Aalto University
School of Chemical
Technology

David Sibarani

Thermal Conductivity of Copper Smelting Mattes and Slags

Master's Programme in Chemical, Biochemical and Materials Engineering

Major in Sustainable Metals Processing

Master's Thesis for the degree of Master of Science in Technology submitted for inspection, Espoo, 20th of June, 2019.

Supervisor Prof. Ari Jokilaakso

Advisor Dr. Matti Luomala

Aalto University
School of Chemical
Technology

Aalto University, P.O. BOX 11000, 00076 AALTO
www.aalto.fi
Abstract of master's thesis

Author David Sibarani

Title Thermal Conductivity of Copper Smelting Mattes and Slags

Degree programme Master's Programme in Chemical, Biochemical and Materials Engineering

Major Sustainable Metals Processing

Thesis Supervisor Prof. Ari Jokilaakso

Thesis Advisor Dr. Matti Luomala

Date 20 June 2019	**Pages** 67 + 5	**Language** English

Abstract

Current cooling system in copper flash smelting furnace has been developed to have a capability of predicting condition of refractory inside an operating furnace. This system requires thermal conductivity of copper matte and fayalite slag, which have never been analyzed in any research. Since flash smelting furnaces process raw material from solid to liquid, the aim of thesis is to measure thermal conductivity of copper mattes and fayalite slag at low to high temperature. The analysis must be able to explain causes of the measured values, their behavior at elevated temperatures, and their connections to characteristics of the samples. Characterization of samples, e.g. using SEM-EDS and XRD, was done prior to thermal conductivity measurement.

The method of thermal conductivity measurement, laser flash analysis, was predetermined from the start of thesis. Five matte samples and three slag samples were prepared. Among the five matte samples, two were doped with arsenic to observe its effect to thermal conductivity of copper matte. The measurement temperature points were 300 °C, 600 °C, and 900 °C, which resemble raw material's temperature inside flash smelting furnace. To observe thermal conductivity of molten slag, one slag sample was measured as well at 1000 to 1200 °C. Thermal conductivity analysis is executed by NETZSCH company, using NETZSCH 467 HT *HyperFlash*®.

The thermal conductivity measurement results for copper matte were 1.2 to 1.5 W m^{-1} K^{-1} at 300 °C and around 2.1 W m^{-1} K^{-1} at 900 °C. Meanwhile, arsenic containing matte samples had lowered thermal conductivity, between 0.5 and 1.3 W m^{-1} K^{-1} at 300 to 900 °C. The observation of experimental data concluded that thermal conductivity of copper mattes increases linearly with temperature. Its dependence on temperature was weak since the margin was barely 1 W m^{-1} K^{-1}. Low values of thermal conductivity were within expectation as copper sulfide has low thermal conductivity based on prior research. Positive relation between thermal conductivity and temperature, however, was outside expectation because it indicated non-conductor material.

Thermal conductivity of observed slags are between 1.6 and 1.9 W m^{-1} K^{-1}. These values were close to prior research in silicate slag. The three slag samples had more than 30 wt-% SiO_2 content and they behaved as glassy slag. Glassy structure of slag samples probably because the basic oxides were only Al_2O_3 and a minor amount of FeO, meanwhile the iron content in all slag samples were not enough for complete fayalite formation. Experimental data of the three slag samples were not conclusive as well because one slag sample had thermal conductivity which was lower than expected. In addition, experimental data of molten slag did not match the references. Its thermal conductivity increased with temperature, although it was supposed to decrease.

Keywords copper matte, fayalite slag, thermal conductivity, laser flash analysis, glassy slag

Preface

This master's thesis is a project from Outotec Finland Oy. I would like to thank Outotec and my calm and smiley supervisor, Professor Ari Jokilaakso, for giving me the chance to learn conductivity, a bit of crystallography, and a bit of quantum physics in order to finish this thesis. Thanks for the guidance, kindness, and humility that eases me to get through all the milestones and hurdles. I would like also to thank Dr. Matti Luomala from Outotec Finland Oy for providing all samples and chemical analysis. This study utilized the Academy of Finland's RawMatTERS Finland Infrastructure (RAMI), based jointly at Aalto University, GTK Espoo and VTT Espoo.

I would like to thank Prof. Emer. Pekka Taskinen for some discussion about thermodynamic and binary phase diagrams, and the monograph he lent me. I would like to thank M.Sc. Lassi Klementinen for his omnipresence, always there to discuss and teach or arrange a training for the SEM and XRD analysis. I would like to thank D.Sc. (Tech.) Imam Santoso, for the insight into microstructure while using SEM and reminding me all the stories behind every different of microstructure, a thing I had forgotten. Lastly, Juhani Heimo, my predecessor in experimenting with thermal conductivity; he has helped me tremendously indirectly, without he ever noticed it, through his thesis script. Lastly, I want to thank Aalto University because I could get almost all the papers and books thanks to your collection ☺

All the opportunities, to learn more in metallurgy in Finland, speaking a bit of Suomea, broaden my horizon in the world of sustainability and instruments of well-beingness, and getting new national and international friends; I would not get these if I were not studying in Finland. For this, I thank LPDP, Indonesia Endowment Fund for Education; without the support, I would not be experiencing such good memories in Finland. I really hope Indonesia and Finland can collaborate more, both in economical and non-economical sectors.

I would like to thank my friends for all the laughter, along with the delicious food we cook. I would like to thank Mother, Father, big brother, big sister, and My big little brother Indra, because I know you keep praying for me. Best for the last, Elisa Udayani, you are light, dear. Thanks for all the love and warmth, keeping me strong. Going up, you light me up!

Soli Deo Gloria. Praise be to Trinity God for giving me the health and ability to finish this script!

Otaniemi, June 2019

David Sibarani

Table of contents

Symbols and abbreviations

Symbols (by order of appearance)

Symbols	Description	Units
j_U	Heat flux	W m^{-2}
K	Coefficient of thermal conductivity	W m^{-1} K^{-1}
T	Temperature	^oC or K
dT/dx	Temperature difference over a certain length	m^{-1} K
q	Heat power	W or J s^{-1}
R	Thermal conductivity resistance	-
A	Surface area	m^2
E	Emitted radiative energy flux	W m^{-2}
G	Energy flux from irradiation	W m^{-2}
α	Radiated energy flux absorptivity of a body	-
	Thermal diffusivity	m^2 s^{-1}
ε	Radiated energy flux emissivity of a body	-
σ	Stefan-Boltzmann constant, 5.67 x 10^{-8}	W m^{-2} K^{-4}
	Electric conductivity	S m^{-1} or mhos m^{-1}
K_e	Coefficient of thermal conductivity by electron	W m^{-1} K^{-1}
K_{ph}	Coefficient of thermal conductivity by phonon	W m^{-1} K^{-1}
C	Heat capacity of quantum particle	J K^{-1}
v	Velocity of a particle	m s^{-1}
l	Mean free path of phonon	m
π	ratio of circle circumference to its diameter, 3.14	-
N	Number of electrons	-
k_B	Boltzmann constant, 1.381 x 10^{23}	m^2 kg s^{-2} K^{-1}
T_F	Fermi temperature	K
ϵ_F	Kinetic energy of fermion particle	J
m	Mass	kg
ρ	density	kg m^{-3}
c_p	Specific heat	J kg^{-1} K^{-1}
e	Charge of electron, 1.6 x 10^{-19}	C
E	Electric field	N C^{-1} or V m^{-1}
j	Electric current density	A m^{-2}
ρ	Total electrical resistivity	ohm (Ω)
ρ_L	Resistivity by lattice vibration (phonon)	ohm (Ω)
ρ_i	Resistivity by imperfection (microstructure defect)	ohm (Ω)
L_n	Lorenz number, 2.45 x 10^{-8}	W Ω K^{-2}
ΔT	Temperature change in a certain duration	K
ΔT_M	Maximum temperature change in an LFA experiment	K
L	Thickness of LFA specimen	m
t	Duration of LFA experiment	s
$[..]_M$	Notation for specimen	-
$[..]_R$	Notation for reference	-
Q	Degree of polymerization	-
X	Mole fraction	-
f	Fraction of basic trioxide compound in slag melt	-
η	Viscosity	Poise
A_w, B_w	Weymann constant	-
r^*	Ratio of M^+ in slag melts	-
R	Gas constant, 8.3144	J mol^{-1} K^{-1}

Abbreviations (by order of appearance)

FSF	Flash Smelting Furnace
SEM-EDS	Scanning Electron Microscope-Energy Dispersive X-Ray Spectroscopy
LFA	Laser Flash Analysis
NBO	Non-Bridging Oxygen
XRD	X-Ray Powder Diffraction
DSC	Differential Scanning Calorimetry
XCT	X-ray Computed Tomography

1 Introduction

Copper exists in nature as two types of minerals, oxide and sulfide, e.g. cuprite (Cu_2O) and chalcopyrite ($CuFeS_2$). Between the two types of minerals, copper sulfide is the dominant one in earth's crust, containing typically from 0.5% Cu (open pit mines) to 2% Cu (underground mines). These sulfide ores are then processed through several stages to become >99% Cu material, i.e. concentration, smelting, and refining (Schlesinger et al., 2011).

Among those smelters, approximately 50% of them use flash smelting technology (Schlesinger et al., 2011). It utilizes oxygen-enriched air to burn the sulfur in the concentrate into SO_2 gas, causing the Cu-Fe-S compound to break into Cu-S and Fe-S compounds. Phase change of the feed from solid to liquid initiates at 1100 ^oC. The temperature of the process in the hearth of the furnace (called 'settler' in flash smelting furnace) is typically around 1250 ^oC (Schlesinger et al., 2011).

1.1 Copper matte and its slag

Two product phases, matte and slag, are formed as a result of oxidation inside flash smelting furnace (FSF). The oxygen-enriched air is blown further to oxidize some percentages of Fe-S into Fe-O, while Cu-S is less likely to be oxidized. Based on Gibb's free energy of sulfides and oxides, Fe-S oxidation precedes Cu-S oxidation (see Appendix A). The liquid phase Cu-Fe-S reports to molten product, which is called copper matte, with typical copper content ranges between 45 and 75% Cu (Schlesinger et al., 2011). The major chemical reactions are shown in equation 1-3 (Seetharaman, S., 2014).

Matte	$2\ CuFeS_2\ (s) + O_2\ (g) = Cu_2S\ (l) + 2\ FeS\ (l) + SO_2\ (g)$	(1)
Matte	$FeS\ (l) + O_2\ (g) = FeO\ (l) + SO_2\ (g)$	(2)
Slag	$2\ FeO\ (l) + SiO_2\ (s) = 2FeO{\cdot}SiO_2\ (l)$	(3)
Interface	$FeO\ (l) + Cu_2S\ (l) = FeS\ (l) + Cu_2O\ (l)$	(4)

Iron oxide then reports to slag phase. Since free FeO with high activity in the slag is capable of oxidizing Cu-S to become Cu_2O (see equation 4) or forming magnetite (Fe_3O_4) out of it, flux is added and mixed with the concentrate feed to lower the FeO activity during smelting (Schlesinger et al., 2011). The flux addition and mixing takes place in a steam dryer unit, prior to FSF.

Among several common fluxing agents in pyrometallurgical industries, silica (SiO_2) is the "valid" flux in FSF processing. Silica works by binding the free FeO in the slag system to form iron silicate or fayalite slag (Fe_2SiO_4), altering FeO into a passive substance against Cu-S. Nevertheless, in industrial smelting, there is always a trace of oxidized copper (Cu_2O) in the slag phase (Schlesinger et al., 2011).

Theoretically, Cu_2S melts at 1130 ^oC, FeS melts at 1194 ^oC, and fayalite slag (Fe_2SiO_4) melts at 1173 ^oC, considering they are pure (Yuan, Q. et al., 2017). Based on melting point of concentrates, smelting furnace temperature of 1250 ^oC is sufficient to melt them.

1.2 Water-cooling system and brick lining in the flash smelting furnace

Refractory lining and water-cooling system is applied on the furnace steel frame to maintain the continuity of process. The order of the furnace wall layers, through which heat is transferred from the source of oxidation to coolant, are: slag-matte bath, accretion or freeze lining, refractory, copper fingers, and copper backing plate (see figure 1). Although the hot face of copper plate is shaped as finger in the figure, nowadays, it is casted in a waffle-structure as it provides better heat transfer and slag freeze-lining (Schlesinger et al., 2011). Material of refractory brick in the FSF is magnesia-chrome.

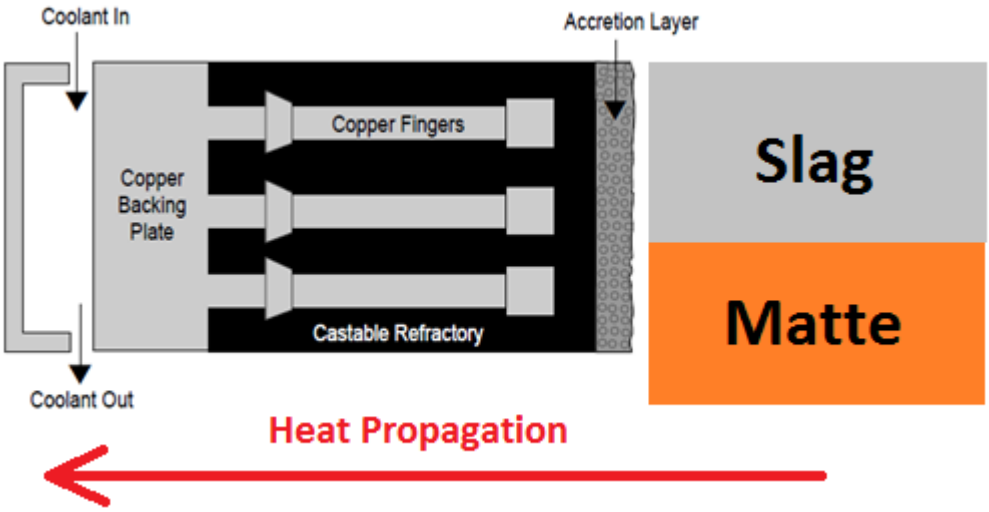

Figure 1 Copper cooling element in furnace wall frame (Kyllo, A. L. et al., 2000) and illustration of heat propagation path from heat source to coolant.

Beside furnace wall, tapping hole is also included in the water cooling system of the FSF. It is a water-cooled copper block installed in the furnace wall. This copper-hole is plugged with moist fireclay, which hardens by the heat of molten bath itself. When matte tapping

starts, the fireclay lid is pierced by using oxygen lance. Once matte tapping is finished, the hole is re-plugged.

Outotec, the global minerals processing and metallurgical technology company, has been perfecting an integrated lining-water cooling system. Figure 2 and 3 shows two elements of the system, Sentinel and copper block. Through this system, cooling performance, brick thickness, and freeze-lining layer can be predicted and controlled to sustain lifetime of the furnace while maintaining quality and productivity of outputs. The instruments are equipped with level 2 (automated control) and level 3 (advanced control and support service) mechanism to optimize its cooling performance, reducing operator's burden, and upgrading the automation whenever necessary (Jansson, J. et al., 2015).

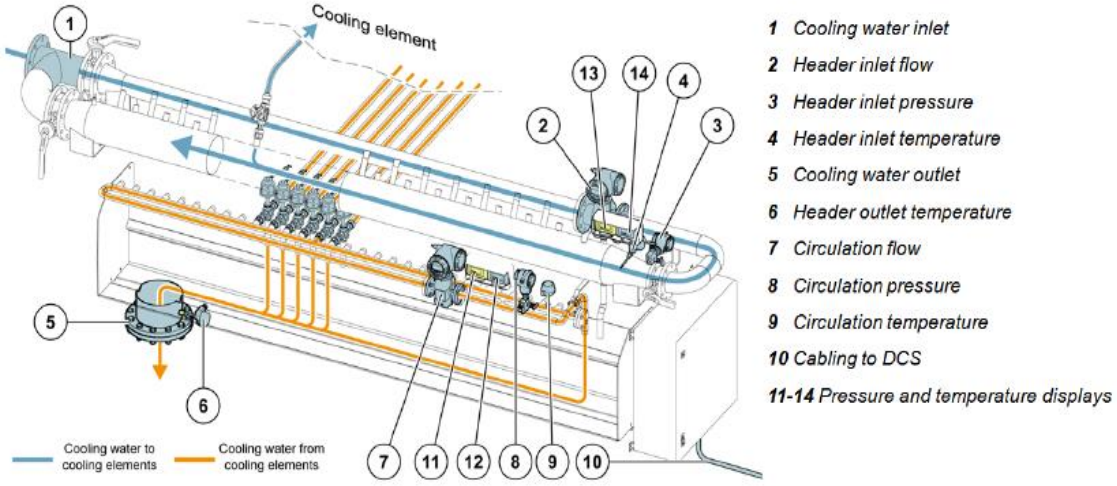

Figure 2 Outotec® Sentinel, instrument to monitor and control the water cooling performance in the smelting furnace (Jansson, J. et al., 2015).

Figure 3 Water cooling system on smelting furnace: furnace wall cooling element with refractory (www.outotec.com).

1.3 Objective of the thesis

Inadequate cooling system chips away brick integrity, which forces the operation to shut down. Meanwhile, excessive design of the whole system creates otherwise avoidable cost. Thermal conductivity of all involved materials is necessary in designing optimum FSF cooling system, lining, and tapping hole. Among them, thermal conductivity of copper matte and its slag is not yet known.

This research aims to experimentally investigate thermal conductivity of copper matte at several Cu grade and its fayalite slag as a function of temperature. It is a novel research because no prior one has specifically analyzed these industrial subjects. The investigation covers the quantitative measure of the thermal conductivity and its qualitative relation to several parameters, including temperature, electrical conductivity, and copper grade. The analysis is carried out in temperature range between 25 and 1000 ^{o}C, where copper matte and fayalite slag are in solid phase. In addition, one slag sample is measured at its molten state, from 1000 to 1200 ^{o}C.

1.4 Thesis Structure

The thesis is started by explaining several chemical and physical properties of copper sulfide and iron sulfide through phase diagrams. Phase diagrams are required because primary parameters of this research are temperature and composition of samples. After that, mechanism of thermal conduction is fully elaborated, starting from the very basic theory of Fourier law of conduction to the atomic phenomena that triggers it.

Since relation between thermal conductivity and several parameters has to be explained in this thesis, literature review is further expanded to factors that are capable of altering the magnitude of thermal conductivity. In addition, mechanism of electrical conductivity is covered because it is connected to thermal conductivity. These factors become the tools to critically analyze results of experiment and to formulate a profound conclusion.

From literature review, three important facts are figured out regarding thermal conductivity of sulfide materials. First, thermal and electrical conductivity could behave differently with temperature, depending on the type of material, either insulator, semiconductor, or conductor. Second, most sulfide minerals are categorized as semiconductor. Third, sulfides behave differently from typical semiconductor, attributed to change of crystal structure at

elevated temperature(s). Therefore, results from prior research are deemed necessary to be covered in this thesis as a comparison for results of this thesis.

Last two parts of literature review are thermal conductivity measurement method and prior research regarding conductivities of sulfide minerals. The measurement method is laser flash analysis which is predetermined from the beginning of thesis. This method is the most used one in several thermoelectric publications, as well as simpler procedure compared to another method called transient plane source (Heimo, J., 2018). Prior research regarding thermal and electrical conductivity of sulfides is provided after the elaboration of laser flash analysis.

The literature review is followed by experimental setup section. The section is divided based on analyzed properties where the name of utilized instruments and the operators are mentioned. Next is result and discussion. Here, the samples comparison are divided into three groups to systematically connect thermal conductivity and properties of each sample. Conclusion and suggestion section summarizes the experimental setup and analysis, while giving several points that can be applied to further confirm the results of this experimental investigation. Lastly, all references and necessary appendices are listed.

2 Sulfide phases

2.1 Phase diagram and crystal structures of Cu-S compounds

Figure 4 shows phase diagram of Cu-S compound. This thesis focuses on Cu_2S, the main compound in copper matte. At room temperature, the phase of Cu_2S is named low-chalcocite, with crystal structure of monoclinic that contains 96 Cu_2S per unit cell. At around 103.5 ^oC, the phase changes into high-chalcocite, which is a hexagonal closed packed structure that contains 2 Cu_2S per unit cell. At around 435 ^oC, the phase becomes digenite-like structured, which is face-centered cubic (Chakrabarti and Laughlin, 1983). The terms γ, β, and α are used in different order between several publications.

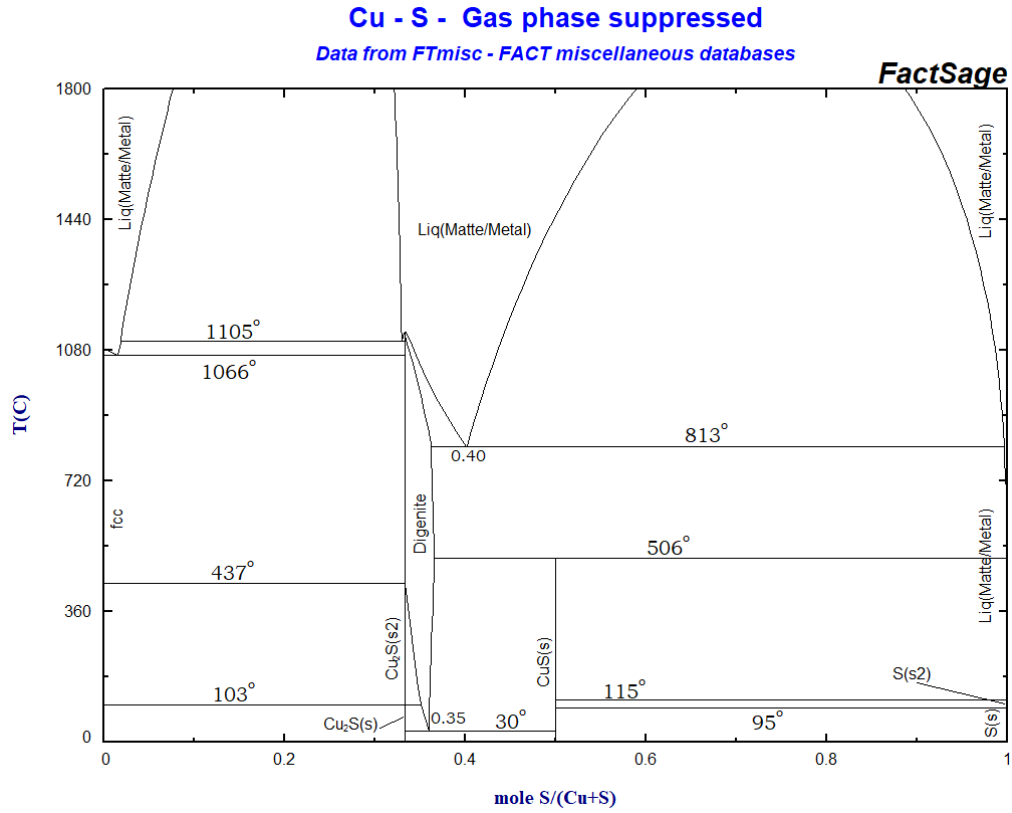

Figure 4 Binary phase diagram of Cu-S compound, taken from FactSage 7.2 and its FTmisc databases [Bale, C.W. et al., 2016].

From the phase diagram, Chakrabarti and Laughlin show that copper metal is thermodynamically possible to be formed or segregated in the copper matte matrix (figure 5). Although the solubility of copper metal is negligible, it is not zero, which means there is possibility for segregated copper metal in the copper matte matrix. A certain amount of copper element could accumulate through diffusion, given the cooling rate is slow enough to give time for diffusion before solidification.

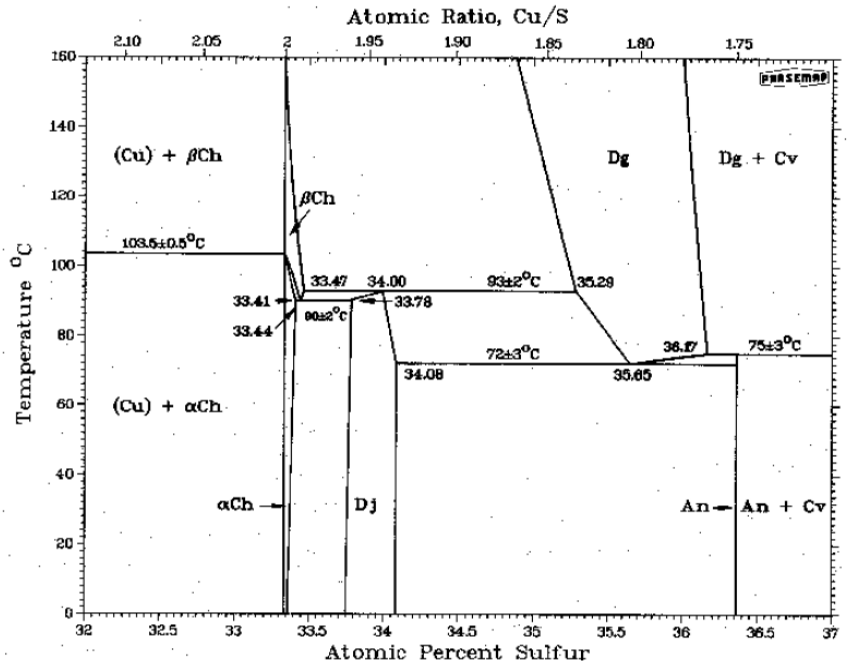

Figure 5 Enlarged view of Cu-S binary phase diagram in the Cu-rich region (Chakrabarti and Laughlin, 1983).

2.2 Phase diagram and crystal structures of Fe-S compounds

Most common Fe-S compounds are FeS_2 and FeS. FeS_2 is found in nature as polymorph, marcasite and pyrite. Marcasite has an orthorhombic crystal structure, while pyrite has a cubic one. Grønvold and Westrum concluded that marcasite is a metastable phase of natural pyrite. It is formed within kinetic boundaries of Fe and S reaction, in which hydrogen might be involved. Two methods could transform marcasite to pyrite, heating to above 700 K or applying mechanical pressure to it. This transformation is irreversible (Grønvold and Westrum, 1976).

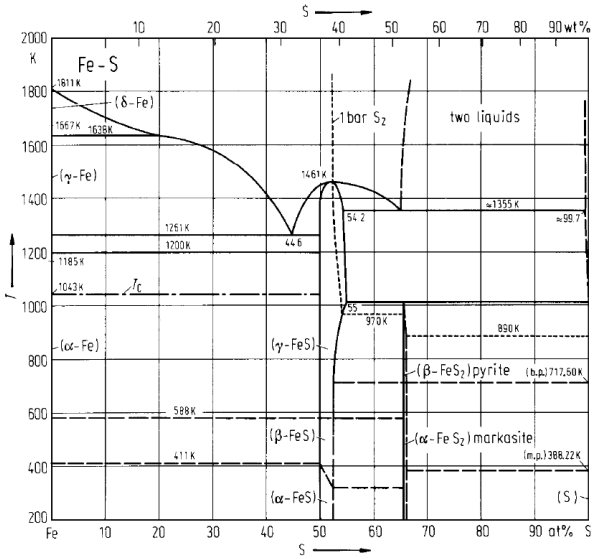

Figure 6 Binary phase diagram of Fe-S compound (Predel, B.).

FeS is formed at 40 to 50 wt-% sulfur. It is a polymorph between $Fe_{1-X}S$ and $Fe_{1+X}S$, as shown in figure 6. FeS is the compound with second highest concentration after Cu_2S in liquid copper matte (Seetharaman, S., 2014). All Fe-S phases, either pyrrhotite, troilite, or mackinawite have complex crystal structure whose thermoelectric properties alter once the structure changes (Pearce et al, 2006). Their properties can shift from semiconductor to conductor, either by temperature or external pressure. If FeS compound is stable in a copper matte solution at every temperature, its conductivities would affect copper matte conductivities.

By temperature, FeS crystal structure changes at 411 and 588 K (138 and 315 °C). The structure of FeS (troilite) at room temperature and pressure is hexagonal α-FeS, a semiconductor one. This structure is sometimes called troilite structure. After α-transition at 138 °C, FeS changes into conductor with hexagonal structure, similar crystal category but slightly different in its lattice parameter. It is marked by a sharp increase in electrical conductivity (Li, Fan, 1996). After β-transition at 315 °C, it changes into hexagonal-semiconductor again. In conclusion, three forms of Fe-S crystal structure belong to hexagonal group (Fei, Y. et al., 1995). This is quite different from Cu_2S whose structure changes with temperature.

FeS variant which has excessive sulfur is called pyrrhotite ($Fe_{1-X}S$). Fan Li stated that the more the X, the more area of troilite structure in phase diagram diminishes, that is below 315 °C. Contradictory to troilite, pyrrhotite has a metallic behavior at room temperature and pressure (Li, Fan, 1996). At the transition temperature (315 °C), its structure changes from monoclinic to hexagonal for Fe_7S_8. Other pyyrhotite variants beside Fe_7S_8 have hexagonal structure at room temperature and pressure, but still have conductivity of a metal (Pearce et al, 2006).

3 Fundamentals of conduction and radiation

Heat conduction is thermal energy transfer from a higher to lower energy point over a material. Since the material acts like a medium, its physical properties would affect the transfer process. Conduction mechanism is less prevalent in materials with less density and crystal structure, meaning the liquid and gas-phased materials. In a less dense material, the most prevalent heat transfer mechanism is a dimensionless one called convection. However, this second approach is not used in this experiment. The last heat transfer mechanism is through gas or vacuum, which is called thermal radiation (Incropera and DeWitt, 2002).

3.1 Thermal conduction

The longer the distance, the slower the heat is conducted. Meanwhile, the bigger temperature difference between two points, the faster the conduction. Mathematically, flux of heat by means of conduction is expressed in Fourier law of conduction:

$$j_U = -K\frac{dT}{dx} \quad , \tag{5}$$

where j_U is heat flux, K is thermal conductivity coefficient, and dT/dx is temperature gradient across the distance (Kittel, C., 1958). Heat flux in this expression is the amount of thermal energy per second per surface area or heat power per surface area. Negative sign only indicates the direction of energy, which is leaving the heat source. In case of multi-layered material, e.g. furnace walls, the heat flux mechanism is illustrated in figure 7, while the calculation method is a simple cumulative operation, as shown in equation 6 and 7.

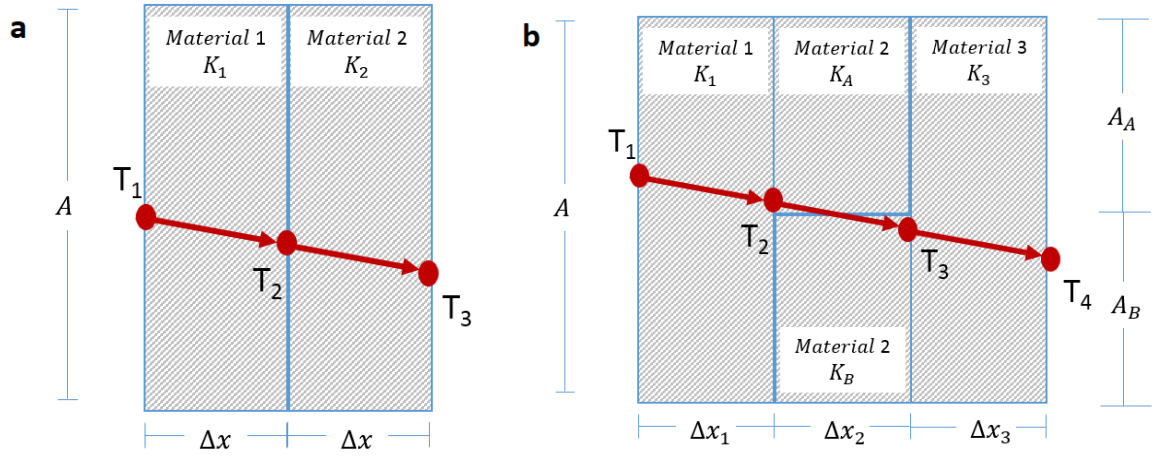

Figure 7 The expression of heat flux in two and three layered walls.

$$q = -\frac{(T_1 - T_3)}{R} \qquad R = \sum_{n=1}^{2} \frac{\Delta x_n}{K_n \cdot A_n} \tag{6}$$

$$R = \sum_{n=1}^{3} \frac{\Delta x_n}{K_n \cdot A_n} \qquad \frac{\Delta x_2}{K_2 \cdot A_2} = \frac{\Delta x_2}{K_A \cdot A_A + K_B \cdot A_B} \tag{7}$$

where q is heat power, T is temperature, R is resistance, A is surface area, Δx is thickness of layer, and K is thermal conductivity coefficient. Equation 6 and 7 follow the relation of electric current with electric potential and resistance. Equation 6 matches a serial circuit, while equation 7 matches a combination of serial and parallel circuit. The equations are expressed in heat power instead of heat flux, considering the surface area of each layer might be different (Incropera and DeWitt, 2002).

3.2 Thermal Radiation

Thermal radiation does not utilize "propagation" term anymore, instead emission and absorption. The energy that leaves the source as electromagnetic wave is called emission (Incropera and DeWitt, 2002). When the wave reaches surface of an opaque material, the energy path is divided into two, absorbed or reflected. The whole process is called thermal radiation, as illustrated in figure 8.

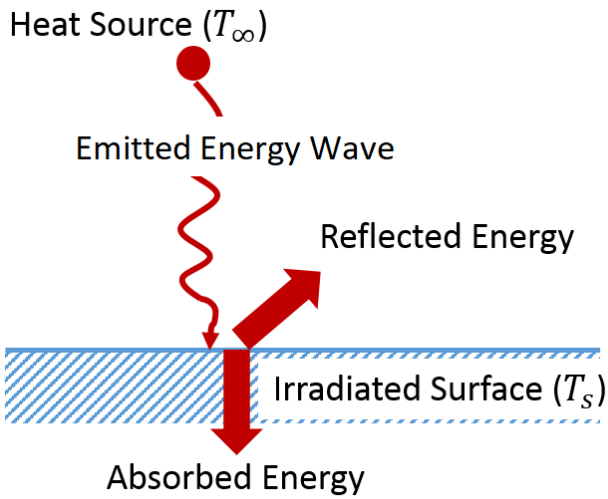

Figure 8 Process of thermal radiation by heat source and irradiation on the body that accepts the heat.

Absence of medium does not mean thermal radiation occurs only in vacuum, but also in any kind of atmosphere, parallel with convection. If the emitted energy is not fully absorbed by the body, then a constant called absorptivity or emissivity is multiplied to the amount of radiative energy from the original source. Absorptivity and emissivity are mathematical expressions of two surface conditions, color and surface finish. They are shown in equation 8 and 9,

$$G_{abs} = \alpha \cdot E \,, \tag{8}$$

$$E_s = \varepsilon \cdot E \,, \tag{9}$$

where E is emitted energy from the heat source, G_{abs} is absorbed thermal energy, α is absorptivity, E_s is emitted energy by the body or in this term is reflected from the heat source, and ε is emissivity (Incropera and DeWitt, 2002). Minimum and maximum value of α and ε are 0 and 1, respectively. If emitted energy is fully absorbed by the body, then absorptivity is 1, whereas zero absorptivity means emitted energy is fully converted into reflected energy.

The surface color of perfect emissivity and absorptivity is black, often called *blackbody* radiation. The amount of emitted thermal energy could be calculated from surface temperature of the particular body, as shown in equation 10:

$$E_s = \varepsilon \cdot \sigma \cdot T_s^4 \,, \tag{10}$$

where, σ is Stefan-Boltzmann constant and T_s is surface temperature of the body. Infinity distance of heat source (figure 8) indicates thermal radiation is also a non-dimension heat transfer, similar to convection, which is unaffected by distance (Incropera and DeWitt, 2002).

4 Atomic scale of thermal conductivity

In atomic scale, thermal conduction is initiated when atoms of a matter absorb heat, whereupon they relay it to the next adjacent atoms through a mechanism. In solid materials, all atoms are densely bound to each other in a structure. Once atoms absorb energy, they would vibrate. Then, the vibration propagates to the other atoms through the atomic bonds. In liquid system, conduction happens in a similar way, but less vibrant due to wider gap between molecular particles (intermolecular spacing). In gas system, the molecules are not structurally bound. Once molecules absorb energy, they move and collide with adjacent molecules. As a result, heat is transferred through the chains of collisions (Incropera and DeWitt, 2002).

Conduction can be hampered by the properties and condition of the material. In case of heat conduction in liquid and gas system, molecule's movement is quite random depending on the material itself, creating possibilities for molecules to interfere with each other. Meanwhile in solid material, heat conduction is determined by the atomic structure of the particular material. Therefore, degree of heat transfer is unique between each material. Even a non-metallic material like diamond has a better thermal conductivity compared to aluminium, attributed to highly-ordered atomic structure of diamond (Incropera and DeWitt, 2002).

4.1 Thermal conductivity in solid material

Atoms in solid matter are not scattered randomly. They are structured as if they have mathematical coordinates. A set of coordinates form a lattice and a set of ordered lattices form a crystal. Crystal is how the atoms arrange themselves in solid matter. Crystals are linked to each other and form a 'grain' if they are aligned in one orientation. Two adjacent groups of crystals with different orientation creates a boundary between them, which is called grain boundary. This boundary marks a discontinuation of bonding between atoms (Kittel, C., 1958).

In quantum physics, all propagations as effect of some physical activities are described as wave, e.g. photon for electromagnetic wave, plasmon for collective electron wave, magnon for magnetization wave, and phonon as elastic wave (Kittel, C., 1958). Propagating thermal energy can be illustrated as a momentum-carrying wave that sweeps the crystals. The momentum is carried by an excited neutron or electron after absorbing energy.

Crystal lattices vibrate in direction with the wave on its axis, thus called lattice vibration. The bigger the wave, the more amplitude of the vibration. Phonon is a quantum unit of the lattice

vibration energy. An irregularity or discontinuation at atoms bonding diminish vibration propagation, which means hampering the thermal conduction (Jiang, C. and Song, J., 2014).

In a conducting material, the carriers of thermal energy are phonon and excited electron (called free electron). In a non-conductor material, the energy carrier is only phonon because electron movement is so limited here. If the material is a conductor or superconductor, phonon contribution to conductivity is negligible compared to electron. This relation is expressed as:

$$K = K_e + K_{ph} \quad , \tag{11}$$

where K is total thermal conductivity, K_e is thermal conductivity by electron, and K_{ph} is thermal conductivity by phonon (Incropera and DeWitt, 2002).

4.2 Thermal conductivity coefficient formulation in quantum physics

Thermal energy flux formulation is expressed in Fourier's law of conduction (eq. 5). On the other hand, thermal conductivity coefficient was formulated based on preceding theory that particle moves after absorbing thermal energy. It is a transformation from heat to kinetic energy. Peter Debye used kinetic theory of gases to describe thermal conductivity coefficient in dielectric solid:

$$K = \frac{1}{3} C \cdot v \cdot l \quad , \tag{12}$$

where C is heat capacity of phonon, v is average phonon velocity, and l is mean free path of phonon (Kittel, C., 1958). If the material is a conductor, then thermal conductivity is dominated by free electron, which changes equation 12 into a product of electron heat capacity, electron average velocity and free-path of electron (Incropera and DeWitt, 2002).

Next, heat capacity can be expanded according to fermion gas concept or free electron gas:

$$C_{el} = \frac{1}{2} \pi^2 N k_B T / T_F \quad , \tag{13}$$

where *N* is number of electrons, k_B is Boltzmann constant, and T_F is fermi temperature. Fermi is a condition that follows Pauli Exclusion Principle, another theory in quantum physics about the quantum state of particles. Below fermi temperature, particles (e.g. electron and neutron) move in an energy level insignificant to its state at absolute zero. Equation (13) is expressed differently in equation (15) by taking into account fermi energy (ϵ_F) of an electron, which is a kinetic energy of a fermion particle (equation 16), product of particle mass (m) and squared velocity (Kittel, C., 1958).

$$k_B.T_F \equiv \epsilon_F \tag{14}$$

$$C_{el} = \frac{1}{2}\pi^2 N {k_B}^2 T/\epsilon_F \tag{15}$$

$$\epsilon_F = \frac{1}{2} m v_F^2 \tag{16}$$

However, thermal conductivity calculation in this thesis uses a different formulation. The equation would depend on the instrument that is used in the experiment. The explanation about the instrument and the thermal conductivity coefficient calculation is covered in section 7.

5 Electrical conductivity mechanism in a material and its relation to thermal conductivity

Electrical conductivity, in similar sense with thermal conductivity, is how quick an electric current can propagate through a material. Electrical conductivity magnitude is decided by the concentration of current carrier, generally electron, and resistivity by the material itself. In quantum state, every atom has its electron placed in its valence band and empty band (conduction band), as shown in figure 9. These two types of band are separated by an energy gap or bandgap (Kittel, C., 1958).

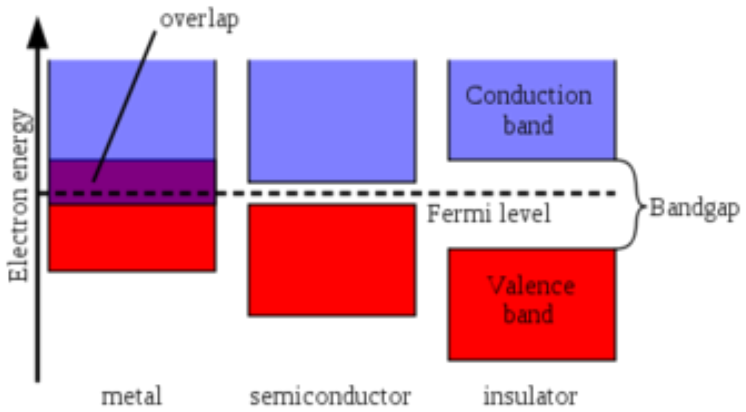

Figure 9 Schematic of energy band gap differences between each material [www.energyeducation.ca].

When an atom is excited by external force that exceeds the energy gap, its electron jumps from valence band to neighboring empty band (sometimes called conduction band), thus creating electrical conduction. Magnitude of energy gap is based on the type of material. For instance, empty band energy level of electric conductors are lower than their valence band energy level and hence their electron travel freely with the smallest amount of electrical field at room temperature. (Kittel, C., 1958).

5.1 Electrical conductivity comparison between each type of material

Another difference between each type of material is the occupation of valence band by electron. If two adjacent valence bands are fully filled or fully empty, it is an insulator. On the other hand, metal is partly filled or partly empty. While in semiconductor, the bands are either slightly filled or slightly empty. All these valence bands condition are illustrated in figure 10.

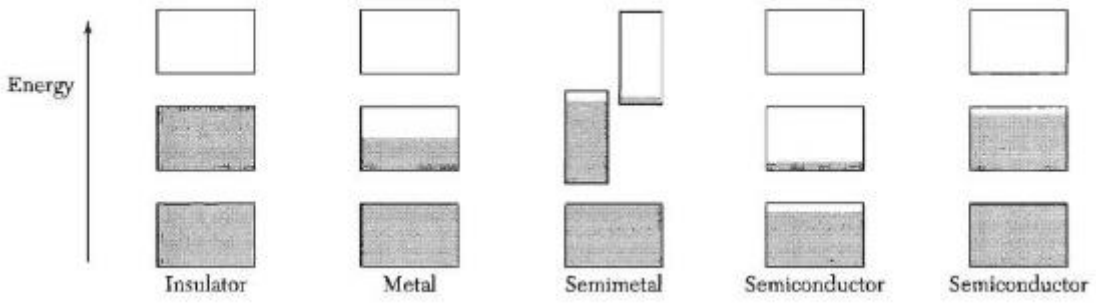

Figure 10 Types of material depending on its valence band. (Kittel, C., 1958)

Electrical conductivity is quantitatively expressed by ohm's law in fermion condition. It shows all the quantum expression as in equation 18. There are many electrical resistivity measurement instrument, and then electrical conductivity is calculated from its resistivity:

$$\sigma = \frac{1}{\rho} \tag{17}$$

where σ is electrical conductivity and ρ is electrical resistivity. Meanwhile, the quantum equation is also known as Drude model of electrical conduction, which is:

$$\sigma = \frac{ne^2\tau}{m} \tag{18}$$

where *e* is charge of electron, *n* is electron concentration, and *m* is mass of electron. Figure 11 shows that electrical resistivity of semiconductor sharply decreases with temperature, while electrical resistivity of conductor increases linearly with temperature (Butera and Waldeck, 1997). However, no publication is found for electrical resistivity analysis of general insulators.

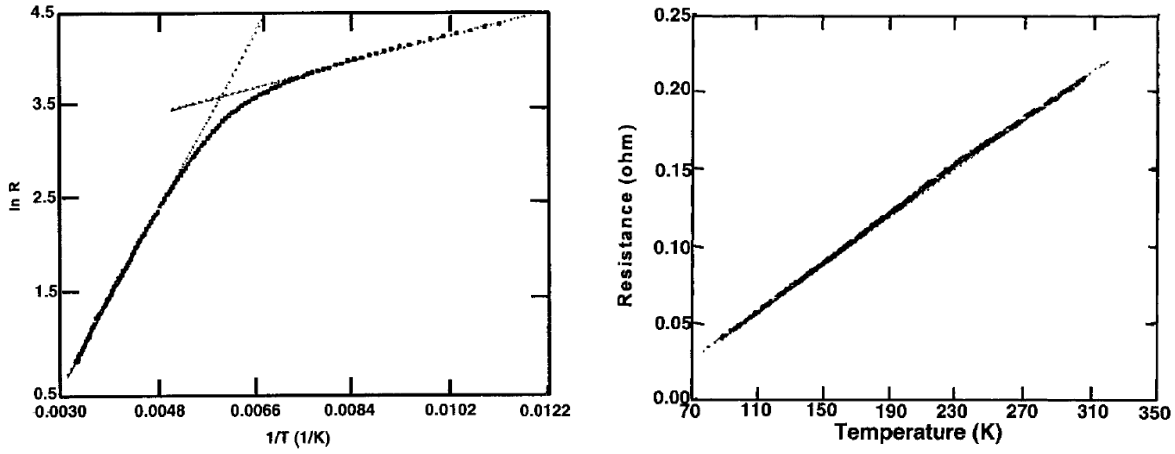

a b

Figure 11 Electrical resistivity change at elevated temperatures of following materials:
(a) semiconductor InSb and (b) conductor copper metal (Butera and Waldeck, 1997).

5.2 Electrical resistivity and its relation to thermal conductivity

Electrical resistivity is divided into two physical phenomena: (1) by phonons and (2) by mechanical defect in the lattice sites. If phonon activity is low, free electron has bigger chance to conduct thermal or electrical energy. If phonon activity is high or an imperfection exist (e.g. lattice vacancy), it can stop or scatter the motion of free electrons (Kittel, C., 1958).

Total electrical resistivity (ρ) is mathematically expressed as,

$$\rho = \rho_L + \rho_i \quad , \tag{19}$$

where ρ_L is resistivity by lattice vibration (phonon) and ρ_i is resistivity caused by mechanical defect or imperfection. Resistivity by phonon vanishes as material approaches absolute zero and rising as temperature increases. Therefore, in most pure materials, as temperature increases, their electrical and thermal conductivity decreases (Haynes, W. M., 2009). This phenomena might be correlated with increasing resistivity by phonon that hinders thermal and electrical conduction by free electron.

5.3 Relation of thermal and electrical conductivity in common solid and liquid systems

In a solid system, electrical conduction is determined by free electron. Once electron absorbs electrical energy, it is then excited and travels (Kittel, C., 1958). Concluding from section 4.1, free electron carries both thermal and electrical conduction, while phonon carries only thermal conduction. Properties of a material determines which one is the dominant carrier. For example, thermal conduction in an electric conductor is dominated by free electron, while in an insulator and semiconductor, it is dominated by phonon (Incropera and DeWitt, 2002). Based on this fact, depending on the material, electrical and thermal conductivity could be in positive or negative relation.

In a liquid system, cation is the medium of electric current; its concentration, charge magnitude, and cation size determine the electrical conductivity. The bigger its concentration and charge, the bigger the electrical conductivity. The smaller its size is, the more easily it roams around the system and the better it conducts electrical energy. Polymeric network that supports thermal conductivity has adverse effect towards electrical conductivity by resisting cation movement in the system (Mills, K. C., 2011).

5.4 Relation of thermal and electrical conductivity in solid metals and conductor

The relation between thermal conductivity and electrical conductivity, theoretically, was stated first in Wiedemann-Franz law, that at not too low temperature, ratio of thermal conductivity and electrical conductivity is directly proportional to temperature, regardless of the element. By combining equation (12) and (15-18), Wiedemann-Franz law could be expressed as:

$$\frac{K}{\sigma} = \frac{\pi^2}{3}\left(\frac{k_B}{e}\right)^2 T \quad , \tag{20}$$

where this equation can be further combined with Lorenz number (L_n), which is defined as

$$L_n = K/\sigma T \, , \tag{21}$$

and finally, L_n become a function of electron charge only, independent of metal element.

$$L_n = \frac{\pi^2}{3}\left(\frac{k_B}{e}\right)^2 = 2.45 \times 10^{-8}\, W \cdot \Omega / deg^2 \tag{22}$$

Equations (20-22) sum up that the ratio of thermal conductivity to electrical conductivity is a product of Lorenz number and material's temperature (Kittel, C., 1958). This formula does not apply at elevated temperature, where good conducting metals (e.g. pure copper and tin) has lowered thermal conductivity (Incropera and DeWitt, 2002).

Thermal and electrical conductivity of metals usually decreases at elevated temperatures because most of them are good conductors (Lide, D. R., 2005). As explained in the beginning of this section, metals have preliminary free electrons at room temperature because of its low conduction band energy. Once a metal absorb heat, in addition to resistivity by phonon, the free electron is excited as thermal-electron and thus colliding with any electrical-electron (Kittel, C., 1958). In conclusion, thermal conductivity has positive relation with electrical conductivity in good conducting material; both of them have negative relation with temperature.

5.5 Relation of thermal and electrical conductivity in solid semiconductor and non-conductor

Semiconductor, as shown in figure 9, has a small bandgap compared to insulator. At elevated temperature, the electron could easily jump to conduction band, becoming free electron. This is the reason semiconductor has better electrical conductivity at high temperature, although not

as high as good conducting metals. Inversely, approaching absolute zero, electrical conductivity of a solid semiconductor decreases as its resistivity increases (Kittel, C., 1958). This peculiar behavior of semiconductor makes them applicable in certain field, e.g. computers and mobile phones.

Originally, non-conductor and semiconductor have high electron resistivity at room temperature and pressure. Referring to equation 11 and 19, this results in contribution of phonon to thermal conductivity being significant, as covered completely in section 6.3. If their thermal conductivity increases along with temperature, it can be said that its phonon activity increases, which hampers electrical conductivity.

This, however, does not mean the absolute value of electrical conductivity becomes lower because, if the increased value of thermal conductivity is 1 to 2 $W\ m^{-1}\ K^{-1}$, surely the electrical resistivity by phonon would increase insignificantly as well and the electrical conductivity could be unaffected. On the other hand, if thermal conductivity slightly decreases at elevated temperatures, its contribution to lowered electrical resistivity would be insignificant as well. To sum it up, thermal conductivity has negative relation with electrical conductivity in semiconductors.

5.6 Doping in semiconductor and its effect toward electrical conductivity

Atomic structure of common material is a complete valence electron sharing (8 electrons covalent bond). Meanwhile in semiconductor, the valence electron sharing is imperfect, either below or more than 8. Negative (n-type) semiconductor has more than 8-shared electrons; positive type has less than 8 electrons. Electron deficiency creates unoccupied electron spot, called ‘hole’. In semiconductor, hole is accounted as current carrier beside electron because it is the place that could accept current brought by travelling free electron (Kittel, C., 1958).

Figure 12 depicts the condition of imperfect valence electron sharing. When a silicon atom (4 valence electrons) in a silicon network is substituted by a phosphorus atom (5 valence electrons), there is an excess of 1 electron. This electron occupies an empty band and can be easily thermally excited. If boron atom (3 valence electron) is the substitute, 1 empty electron slot will become the ‘hole’ and available to accept any excited electron. This substitution method is called doping and it enhances the electrical conductivity characteristic of a semiconductor. Due to this phenomena, alloying has a possibility to change metal into semiconductor (Kittel, C., 1958).

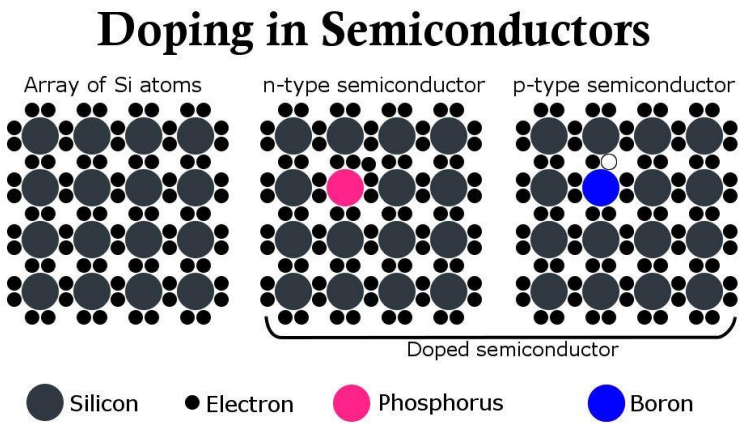

Figure 12 Electron sharing condition in intrinsic semiconductor and doped one. Pink dot has excess electron, blue dot is electron-deficient [www.scienceabc.com]

In case of silicon doping, boron addition in ratio one boron atom per 10^5 silicon atoms increases pure silicon conductivity at room temperature by a factor of 10^3 (Kittel, C., 1958). Either doping effect to silicon turn it to n-type or p-type semiconductor, is easily analyzed as silicon being a simple tetrahedral-structured solution. Effect of doping to some semiconductor, e.g. Cu_2S and CuS, are difficult to analyze without direct observation to the compound with proper equipments. After all, they are known for their complex crystal structure (Wuensch and Buerger, 1963).

6 Factors affecting thermophysical properties

Major factors that affect thermal conductivity of a material are its crystal structure, composition, temperature, viscosity, basicity, density, and specific heat capacity. Moreover, they are intertwining and influencing each other. For example, temperature could change crystal structure, specific heat capacity, and density of a material. Therefore, the discussion in this research revolve around these properties and their effects to each other (Mills, K. C., 2014).

6.1 Change of properties based on basicity

In case of liquid slag, thermal conductivity is influenced by the presence of network former/breaker compounds. The networks are actually phonon free-path. The more networks, the greater the vibrations, the higher the thermal conductivity (Mills, K. C. et al., 2011).

Network formers are acidic oxides, e.g. SiO_2 and P_2O_5, for they create networks with other similar compounds through the O bonding. Network breakers are basic oxides, e.g. Na_2O, CaO, FeO, and MgO, which donor their oxygen into the solution. Once acidic oxides catch the free oxygen, oxide networks collapse, resulting in lowered thermal conductivity. For example, "networked" SiO_2 turns into depolymerized SiO_4^{4-} after binding free oxygen.

The sensitivity of thermal conductivity of slags to network formers/breakers can be related to other physical properties of solutions, e.g. basicity and viscosity. Thermal conductivity is in opposite relation to basicity and in correlation with viscosity. Basicity used to be the parameter to characterize network, but currently viscosity and optical basicity are the ones applied in conductivities modelling (Mills, K. C. et al., 2011).

Effect of basicity to conductivities of solid slag is displayed by some results of numerical method. Relation between network parameter and thermal conductivity of solid slags is drawn from a regression of several experimental data (Mills, K. C. et al., 2011). Connection between these two parameters are published in other publications as well, as shown in section 8.

6.2 Change of properties in slag system based on temperature

In solid slag, thermal conductivity behavior to temperature is not always linear. Slag structure is classified into two categories depending on the composition, glassy or crystalline. Glassy

solid slag behaves like glass, has glass transition temperature (denoted as T_g) and entering supercooled-liquid state before becoming liquid (Mills, K. C. et al., 2011).

When glass is heated up approaching its T_g, its heat capacity increases drastically, as it becomes an amorphous solid. This state is extremely viscous, causes increasing thermal conductivity. From the peak of T_g, as temperature keeps increasing, amorphous glass changes into liquid. Its viscosity then decreases smoothly along with its thermal conductivity (Mills, K. C. et al., 2011). On the other hand, crystalline slag's behavior is quite linear, where its thermal conductivity decreases with temperature without fluctuation, as shown in Figure 13.

Once a solid slag system absorb heat more than it can transfer, its lattices vibrate intensely and eventually collapse; it turns into liquid slag. In liquid slag system, increasing system temperature loosen the structure of the system itself, causing its surface tension and viscosity to decrease. Therefore, thermal conductivity of a liquid slag system decreases with temperature.

Structure of slag is more likely to be decided by the degree of polymerization of slag than the cooling rate. Higher network former concentration indicates higher polymerization degree, render the slag to be more glassy structured (Mills, K. C. et al, 2011). Important to note, although thermal conductivity behavior of glassy slag is to increase in rising temperature, but its value at room temperature is lower than crystalline slag by a factor of 1.5 to 2.5 (Nishioka, K. et al., 2006).

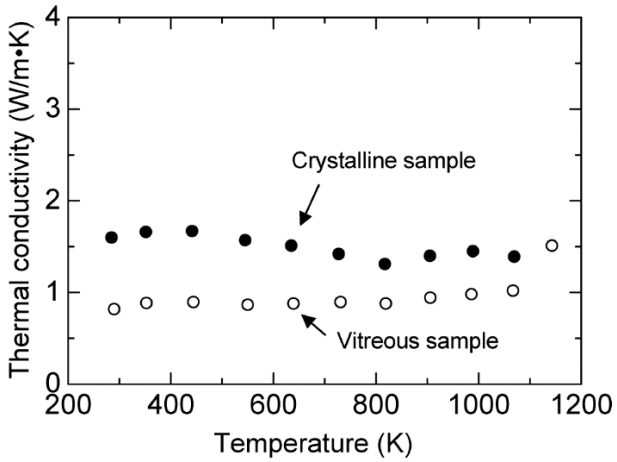

Figure 13 Comparison of thermal conductivity of solid slag between crystalline slag and glassy/vitreous slag (Nishioka, K. et al., 2006).

Mills has compiled many theories regarding thermophysical properties modelling, especially structure of slag. He profoundly explain structure of slag, whose application is more than just a concept of glassy and crystalline slag. Structure of slag could be quantified into degree of

polymerization and viscosity, which are more complex than basicity. These two parameters were used in modelling thermal conductivity. This method is elaborated in section 7.5.

6.3 Change of properties in non-slag system based on temperature

This sub-section further deepen literature review in section 4.1, 5.4, and 5.5 about effects of elevated temperature to thermal conductivity of conductor (mostly metals) and non-conductor. Conductor material has higher electron activity, which means phonon contribution to heat transfer is negligible. Non-conductor and semiconductor are different from conductor in a way that contribution of phonon to their thermal conductivity is not negligible.

On the basis that phonon has positive relation with temperature, effect of temperature is therefore different between conductor and non-conductor (including semiconductor). Elevated temperature would decrease thermal conductivity of conductor, which otherwise increase thermal conductivity of non-conductor (Incropera and DeWitt, 2002). Some examples are shown in figure 14. However, relation between temperature and thermal conductivity could be various in semiconductor. One thing for certain, its thermal conductivity is extremely lower than conductor.

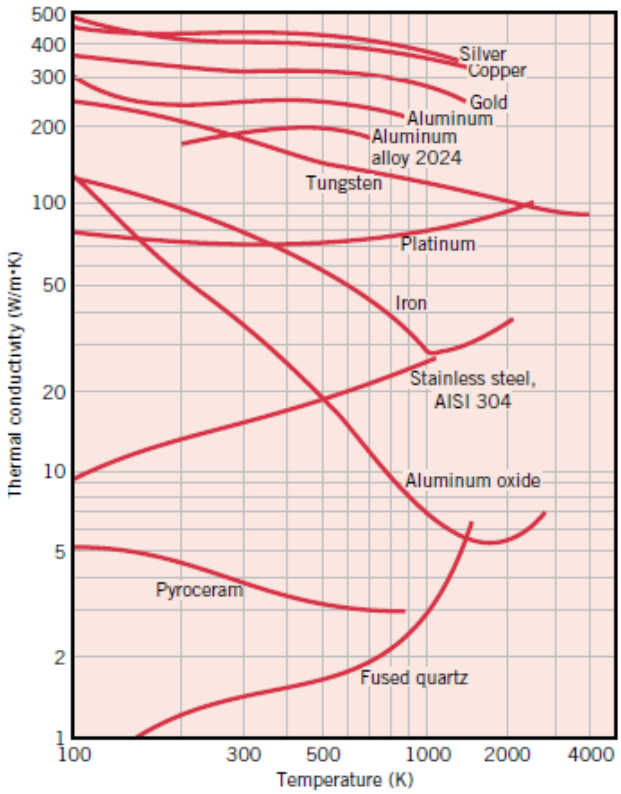

Figure 14 Thermal conductivity of both solids of heat conductor and non-conductor (Incropera and DeWitt, 2002).

No statement generally claims that thermal conductivity of semiconductor must be going down with increasing temperature, probably because the vast type of semiconductors that has yet to be covered completely. However, several research show that typical semiconductor (metals and alloys) would have decreasing thermal conductivity at elevated temperatures (table 1), unless there is any change in its structure or any other reason, which is explained completely in section 8.

Table 1 Thermal conductivity of several intrinsic semiconductors.

Compound	Temperature [K]	Thermal Cond. [$W.cm^{-1}.K^{-1}$]	Reference
Silicon	20-1600	49.8-0.221	Lide, D. R., 2005
Germanium	10-1200	17.7-0.174	Lide, D. R., 2005
Tin	2-500	323-0.596	Lide, D. R., 2005
Graphite*	100-2000	49.7-2.62	Lide, D. R., 2005
Gallium Arsenide	50-800	5-0.15**	Bogaard, R.H. and Ho, C.Y., 1989

*) Graphite is categorized into 2 type based on its measurement orientation relative to the sample, parallel or perpendicular to its layer planes.
**) Values are obtained only from graphic, so the numbers might not be exact

6.4 Change of properties based on composition and chemical formula

The negative relation of temperature and thermal conductivity does not appear in fluoride slag. At temperature range around 700-1400 K, thermal conductivity of this solid slag increases from 0.9 to 1.67 W m^{-1} K^{-1}. Thermal conductivity is even higher if CaF_2 content in the solid slag is increased, around 1.738-2.558 W m^{-1} K^{-1}. Though slag structure is not mentioned in the paper, it is suspected to be crystalline because CaF_2 and CaO are basic and network breakers (Yanwu Dong et al., 2015). Presence of a certain compound might change the thermophysical properties of a mixture into new properties which are not possessed by each individual compound.

In industrial copper matte, the Cu-S stoichiometry is Cu_2S. Among $Cu_{2-X}S$ stoichiometric structure, Cu_2S has the lowest thermal and electrical conductivity (Qiu, P. et al., 2016), while CuS has the best electrical conductivity (Liu, Y. et al., 2017). If by any chance, there is another $Cu_{2-X}S$ compound beside Cu_2S present in the copper matte, it could alter the magnitude of conductivities and its behavior under elevated temperature. Therefore, the SEM-EDS analysis is necessary for predicting chemical formula of each sample (Liu, Y. et al., 2017).

6.5 Change of properties based on thermal expansion

It is reported that thermal conductivity of liquid material is far below solid material. Increased intermolecular space in liquid material obviously diminishes phonon magnitude and reduces thermal conductivity. However, rising intermolecular space does not happen only after phase change, but also during thermal expansion of solid phase. Thermal conductivity and diffusivity are directly proportional to density. If density of a material decreases as its volume expands, then thermal conductivity by phonon activity in all materials is diminished by thermal expansion (Incropera and DeWitt, 2002).

6.6 Metal-Insulator Phase Transition

Good conducting materials could turn into non-conducting materials and vice versa by some method. There are five theories that explain such phenomena meticulously in quantum physic way. In general, several things could trigger this transition, including: electron concentration change, structure change, magnetic property change, and fermi energy change. However, no information that this concept applies to semiconductor as well (Horvat, A. et al, 2013).

Electron concentration can be changed by doping of conducting electron. If an insulator is doped by sufficient conducting electrons, it could behave as metallic conductor. Surprisingly, if a metallic conductor is doped with more conducting electrons, electron localization starts to occur, similar to human overpopulation, which lower the conductivity performance of particular conductor. The other three properties could be triggered by external pressure or high temperature application (Horvat, A. et al, 2013).

7 Thermal conductivity measurement method

One of instruments that can be used to measure thermal conductivity is laser flash analysis (LFA). It was introduced first time in 1961 (Parker, W. J. et al., 1961) to measure thermal diffusivity and specific heat capacity. These two properties are then used to calculate thermal conductivity of a material. The mechanism works by shooting a high-intensity short-duration light pulse to front face of an insulated specimen, as illustrated in figure 15.

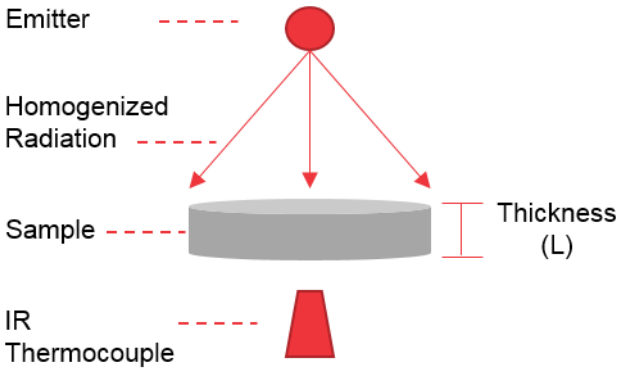

Figure 15 A simple sketch of thermal conductivity measurement using LFA

7.1 Thermal diffusivity and relation to thermal conductivity

Thermal diffusivity can be described as a value that inform how quickly temperature of a material can change or how quickly the heat propagates. Therefore, it is a material-specific property and has a direct relation with thermal conductivity. It is mathematically expressed as follows:

$$K = \alpha \cdot \rho \cdot c_p \,, \tag{23}$$

where α denotes thermal diffusivity, ρ denotes density of material, and c_p denotes specific heat capacity of material (Shinzato and Baba, 2001). Equation 23 is the final equation that dictate the thermal conductivity measurement by the instrument that is used in this research. It was firstly elaborated through derivation of Carslaw and Jaeger's equation (Parker, W. J. et al., 1961). Thermal conductivity and specific heat capacity are the intrinsic properties, while thermal diffusivity is an interdependence between thermal conductivity and specific heat capacity.

7.2 Principle of laser flash analysis

The flash acts as radiation energy toward specimen's surface. The few millimeter-thick specimen is coated with a black material for a perfect blackbody radiation absorption. Temperature change on its rear surface is measured by a thermocouple and recorded with oscilloscope and camera. When this apparatus was designed for the first time, it was tried at temperature from 22 ºC to 135 ºC. Example of LFA output is given in Figure 16.

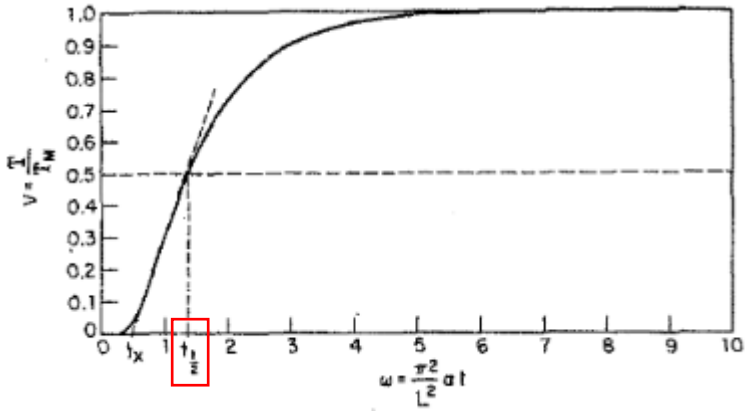

Figure 16 Chart of measured temperature relative to time of heating; y-axis is the ratio of temperature to maximum measured temperature; on x-axis, $t_{0.5}$ is drawn as time that marks half-maximum temperature (Parker, W. J. et al., 1961).

Since the specimen is a solid matter that is heated up at its front surface, heat propagates to rear surface by means of thermal conduction. LFA output chart in figure 16 is to be used in determining thermal diffusivity. Thermal diffusivity calculation was derived from Jaeger and Carslaw's one dimensional thermal conduction equation as follows:

$$\Delta T = \Delta T_m \left[1 + 2\sum_{n=1}^{\infty}(-1)^n exp\left(\frac{-n^2\pi^2\alpha t}{L^2}\right)\right] \tag{24}$$

where ΔT is temperature change of specimen, ΔT_m is maximum temperature of the rear surface of specimen, α is thermal diffusivity, t is time of temperature changing, and L is thickness of specimen. If time is assumed to be the time needed for temperature to reach half of its maximum temperature, then equation (24) can be solved as:

$$\alpha = \frac{0.1388 \times L^2}{t_{0.5}} \tag{25}$$

7.3 Improved laser flash apparatus arrangement

In 2001, a new arrangement of LFA was introduced through a publication (Shinzato and Baba, 2001), claimed to be able to accurately measure thermal diffusivity and specific heat capacity of solid materials by single LFA apparatus up to 1700 K under inert atmosphere. It utilized a reference specimen of known specific heat capacity. Additionally, both reference and specimen must have identical shape and dimension.

Both samples are flashed with homogenized laser to supposedly be irradiated with same intensity. Hence, both have to possess equal degree of absorptivity. It was managed through surface polishing and coating them with the same black material. This way, the specific heat capacity of the material is calculated from comparison with specific heat capacity of the reference.

After thermal diffusivity is calculated, specific heat capacity of specimen can be obtained from ratio of heat flux between specimen and reference, which is:

$$c_{p,M} = \frac{A_M m_R \Delta T_R}{A_R m_M \Delta T_M} \cdot c_{p,R} \tag{26}$$

where A is surface area, and notation $_M$ for specimen, while notation $_R$ for reference. Then by re-writing mass as product of density and volume, equation (26) can be re-written as,

$$\rho \cdot c_{p,M} = \frac{L_R \Delta T_R}{L_M \Delta T_M} \cdot \rho \cdot c_{p,R} \tag{27}$$

When equation 23, 25, and 26 are included in the LFA software, it automatically give outputs of specimen's thermal diffusivity, specific heat capacity, and thermal conductivity (Shinzato and Baba, 2001). Today's LFA, equipped with its packaging software, is capable of measuring thermal diffusivity and specific heat capacity right away with a single instrument. It is unknown whether it follows arrangement by Shinzato and Baba or its own mechanism.

7.4 Correction of LFA calculation regarding thermal expansion

Thermal expansion induces change in thermal conductivity as explained in section 5.4. Dimensional change then is applied in equation (23) and (25) because thermal conductivity measuring instrument does not take into account thickness change. By using a special apparatus, e.g. dilatometer, change of specimen's length is obtained at each temperature point,

and then, used as a correction factor to these two equations. The final equation of thermal conductivity and thermal diffusivity are then shown in equation 28-30, respectively.

$$K_{corrected} = \alpha_{corrected} . \rho_2 . c_p \ , \tag{28}$$

$$\rho_2 = \frac{m}{V_2} \ , \tag{29}$$

$$\alpha_{corrected} = \frac{L_2^2}{L_1^2} \cdot \alpha \ , \tag{30}$$

where ρ is density after volume change, V_2 is volume after thermal expansion, L_2 is length or thickness after thermal expansion, L_1 is thickness at room temperature.

7.5 Determination of thermal conductivity through structure of slag

Section 7.1 until 7.4 profoundly explain LFA method, but this section shows a different approach to determine thermal conductivity, applicable to liquid and solid slag (Mills, K. C. et al., 2011). It is not obvious whether all types of slags are approachable by this method since only oxide slags are used in the publication. In addition, the equations are already applied in the modelling software by Mills. The first important parameter is degree of polymerization,

$$Q = 4 - NBO/T \tag{31}$$

$$NBO/T = \frac{2(X_{MO} + X_{M_2O} + 3fX_{M_2O_3} - X_{Al_2O_3} - (1-f)X_{M_2O_3})}{(X_{SiO_2} + 2X_{Al_2O_3} + 2(1-f)X_{M_2O_3})} \tag{32}$$

where Q is the degree of polymerization, X is mole fraction, f is the fraction of M_2O_3 that act as network breaker, MO refers to any single oxide compounds, M_2O for double oxide ones and M_2O_3 for trioxide ones. NBO is the abbreviation for non-bridging oxygen and T stands for tetrahedral compound, e.g. silica, thus, NBO/T is a parameter called degree of depolymerization, not a ratio of two parameters named NBO and T.

The value Q then is used to calculate thermal conductivity at certain temperature,

$$\ln k_{298} = -0.424 + 0.00002 \exp(Q/0.299) + 3.2 \, X_{Li_2O} \tag{33}$$

$$\ln k_{Tg} = -0.435 + 0.00005 \exp(Q/0.332) + 3.0 \, X_{Li_2O} \tag{34}$$

where k_{298} is thermal conductivity at 298 K and k_{Tg} is thermal conductivity at glass transition temperature. This model was made based on regression of experimental data. The developer stated that from room temperature until glass transition temperature, thermal conductivity

linearly increases. Equation 31-34, however, was claimed to work only for slag with $2.2 \leq Q \leq 3.3$.

Beside thermal conductivity, viscosity could be quantified by numerical method. There are three models for it. The one shown here is the simplest out of 3, named Riboud Model,

$$\eta = A_w \cdot T \cdot \exp(B_w/T) \tag{35}$$

$$A_w = \exp(-19.81 + 1.73X_{`CaO'} + 5.82X_{CaF_2} + 7.02X_{`Na_2O'} - 35.76X_{Al_2O_3} \tag{36}$$

$$B_w = 31140 - 23896X_{`CaO'} - 46356X_{CaF_2} - 39159X_{`Na_2O'} + 68833X_{`Al_2O_3'} \tag{37}$$

where η is viscosity, T is temperature in Kelvin, A_w is Weymann constant A, and B_w is Weymann constant B. Lastly, the components of equation 36 and 37 are calculated by,

$$X_{`SiO_2'} = X_{SiO_2} + X_{P_2O_5} + X_{TiO_2} + X_{ZrO_2} \tag{38}$$

$$X_{`CaO'} = X_{CaO} + X_{MgO} + X_{FeO} + X_{Fe_2O_2} + \{X_{MnO} + X_{NiO} + X_{CrO} + X_{ZnO} + X_{Cr_2O_3}\} \tag{39}$$

$$X_{`Na_2O'} = X_{Na_2O} + X_{K_2O} + X_{Li_2O} \tag{40}$$

$$X_{`Al_2O_3'} = X_{`Al_2O_3'} + \{X_{`B_2O_3'}\} \tag{41}$$

One important point is that $X_{`SiO_2'}$ is not included in either equation 36 or 37. Perhaps it must be the variable of the first component. The model is valid only in the following slag composition range: $SiO_2$ (28-48%), CaO (13-52%), $Al_2O_3$ (0-17%), $CaF_2$ (0-21%), and $Na_2O$ (0-27%). Clearer explanation regarding $X_{`SiO_2'}$ and whether the composition percentages are weight or atomic are not found. The bracket {} indicates something that the software would process differently.

7.6 Determination of electrical conductivity through structure of slag

Two models had been developed for calculating electrical conductivity of liquid slag. The first one is based on optical basicity and the second one is based on viscosity (Zhang and Chou, 2010). The model explained here is only the latter one,

$$M_2O - SiO_2: \quad \ln\kappa = (0.02 - \ln\eta)/2.87 \tag{42}$$

$$MO - SiO_2: \quad \ln\kappa = (0.15 - \ln\eta)/1.1 \tag{43}$$

where κ is electrical conductivity notation used by Zhang and Chou. The model is further expanded when the slag contains not only M^+, but also M^{2+}, M^{3+} and M^{4+},

$$r^* = 2\,\Sigma\,X_{M^+}/\Sigma\,(\,2\,X_{M^+} + X_{M^{2+}} + 0.667\,X_{M^{3+}} + 0.5\,X_{M^{4+}}) \quad (44)$$

$$\ln\kappa = 0.15 + r^* \cdot 3.87 - (\ln\eta/\{1.1 + 1.77r^*\}) \quad (45)$$

where r^* is the ratio of cation M^+ in the slag. The application of this model is still only for slag melts, yet this is by far the only model for electrical conductivity measurement (Mills, K. C. et al., 2011). Units of parameters used by Zhang is poise for the viscosity and S cm^{-1} for the electrical conductivity.

Actually, Mills claimed that optical basicity is better in determining structure of slag because it includes the number of oxygen of each molecule in the calculation. This means optical basicity differentiate the effect of each cation to the silicate structure, while viscosity from Q might not do. However, the optical basicity based-model is originally made for calcium-aluminosilicate slag system. No explanation whether it can be applied in another system with similar cation number.

8 Prior research on conductivities of sulfidic minerals and silicate slag

Objects of investigation in this thesis are copper matte and fayalite slag. There is not any prior research that specifically observe them before, thus the collected publications are thermal and electrical conductivity of some general sulfides. The selected sulfides data are ones which have close chemical formula to copper matte e.g. chalcocite and pyrite. Prior research data are collected as tools to validate thesis data.

The interesting fact is that many sulfidic minerals had been categorized as semiconductor. Research regarding their electric conductivity has advanced to the stage where alloying and crystallization are applied to create artificial sulfides and, sometimes, having their crystal structure modified for thermoelectric research, a 2-way conversion between electrical potential and heat. Based on semiconductor's trait, sulfidic mineral's electrical conductivity increases at elevated temperatures, as shown in figure 17 (Garbee, 1969 and Pearce et al., 2006).

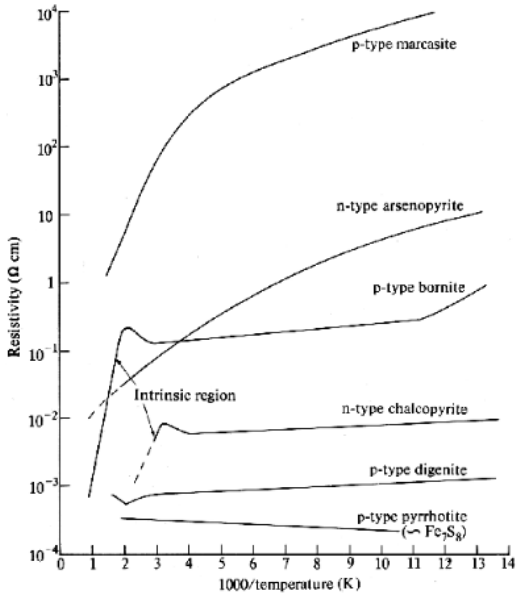

Figure 17 Resistivity of several sulfide minerals (Pearce et al., 2006).

8.1 Conductivities of Cu_2S

Research of thermophysical properties of Cu-S minerals are mostly aimed for semiconductor development. As preliminary study before experiment, hypothesis on copper matte thermal conductivity is approached from molar heat capacity and thermal conductivity of Cu_2S. In cited prior research, the samples were obtained from alloying of pure copper and pure sulfur in.

Specific heat capacity holds a close direct relation with thermal conductivity (Nishioka, K. et al., 2006). From equation 23, higher specific heat capacity means higher thermal conductivity.

Figure 18 shows molar heat capacity of Cu_2S increase steadily at temperature range 0-89 ^oC, from 0 to 10.1R J $mol^{-1}K^{-1}$ or 0.5 J g^{-1} K^{-1}. Then, it is spiking to more than 121R J mol^{-1} K^{-1} or 6.3 J g^{-1} K^{-1}, attributed to phase transition from $\gamma\ to\ \beta$. From around 107 ^oC, it keeps decreasing steadily until another spike due to phase change at 437 ^oC, from β to α. Range of molar heat capacity of Cu_2S at temperature 107-677 ^oC is 13.2R to 9.96R J mol^{-1} K^{-1} or 0.7 to 0.5 J g^{-1} K^{-1} (Grønvold and Westrum, 1987).

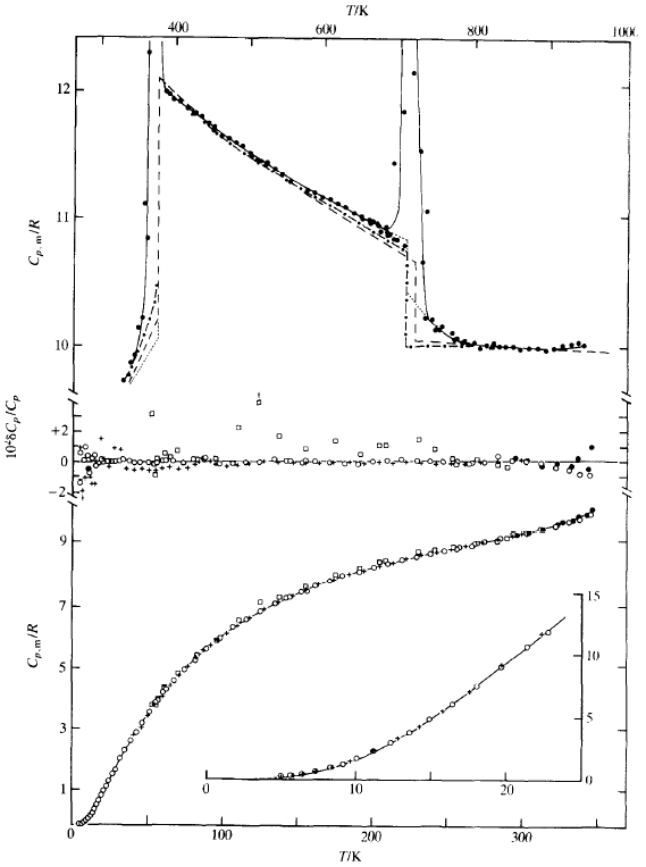

Figure 18 Molar heat capacity of Cu_2S from room temperature. Lower chart is the low temperature measurement. The y-axis was scaled in *R*, gas constant (Grønvold and Westrum, 1987).

Figure 19 shows experimental data of two experiments, which are of similar behavior and magnitude, between 0.3 and 0.4 W m^{-1} K^{-1}. Below 89^oC, its specific heat capacity increases, while its thermal conductivity decreases. The γ-chalcocite behaves like typical intrinsic p-type semiconductor at elevated temperatures. After Cu_2S changes into β-chalcocite, its specific heat capacity steadily decreases, while its thermal conductivity steadily increases. However, after changing into cubic chalcocite, when its specific heat capacity dropped, its thermal conductivity also decreases with temperature. It seems fluctuation of specific heat capacity is quite different from fluctuation of thermal conductivity.

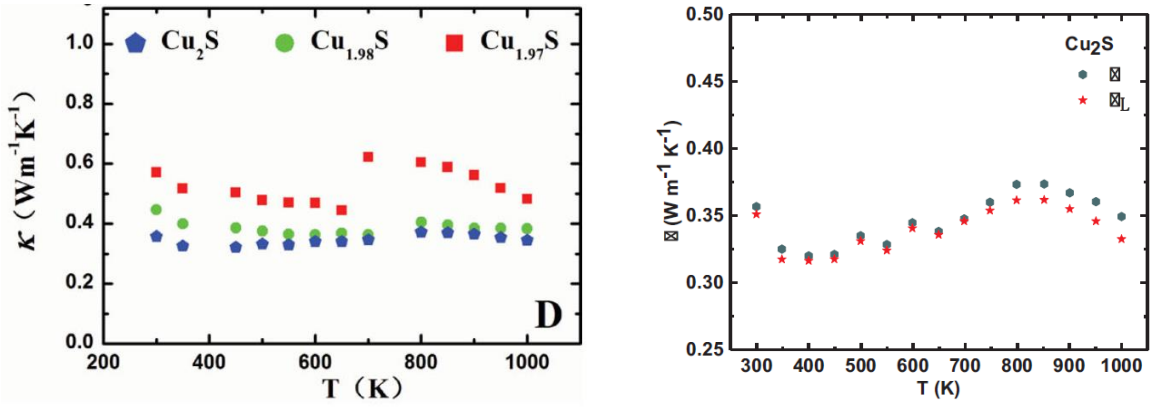

a b

Figure 19 Thermal conductivity of artificial Cu_2S: (a) using Netzsch LFA457 (He, Y. et al., 2016); (b) specified as two types, total electrical conductivity (blue dots) and phonon activity (red dots). (Duan, J. et al., 2018)

After the first structure transition, thermal conductivity increases until next structure transition. Ying He et al. claimed that thermal conductivity of Cu_2S at β and α was independent of temperature because the value change was insignificant. They deduced that α-chalcocite did not behave as a semiconductor anymore, instead a metal, because its electrical conductivity decreased with temperature (see Figure 20b). This statement matches figure 19b, where there is a contribution from electron to total thermal conductivity after second structure change at 700 K. Thermal-electron works only in conductors.

Measured specific heat capacity by Ying He accurately matches figure 18 by Grønvold and Westrum. Consequently, they argued specific heat capacity should not be seen as the only reference because changes in thermal diffusivity and density alter thermal conductivity as well. The focus should be more into the magnitude of thermal conductivity that is extremely low and fluctuates no more than 0.1 W $m^{-1}K^{-1}$ until 1000 K (Ying He et al., 2016).

The behavior of electrical conductivity was derived from electrical resistance in several publications (Figure 20), measured by using an old two probe method with electrometer and potentiometer. From Figure 20a, Cu_2S electrical conductivity increases to about 55 S/cm at first structure change at 110 ^oC. Thereafter, it abruptly drops to around 7 S/cm and steadily increases until around 20 S/cm. At second structure change (470 ^oC), it leaps abruptly higher than that of γ phase, above 140 S/cm (Hirahara, E., 1950). The range of electrical conductivity in figure 20b is 1-20 S cm^{-1}, whereas it is 7-150 S cm^{-1} in figure 20a. The results might be different due to different tools of experiment. Ying He used the modern Ulvac ZEM-3 to measure all electrical properties (Ying He et al, 2016).

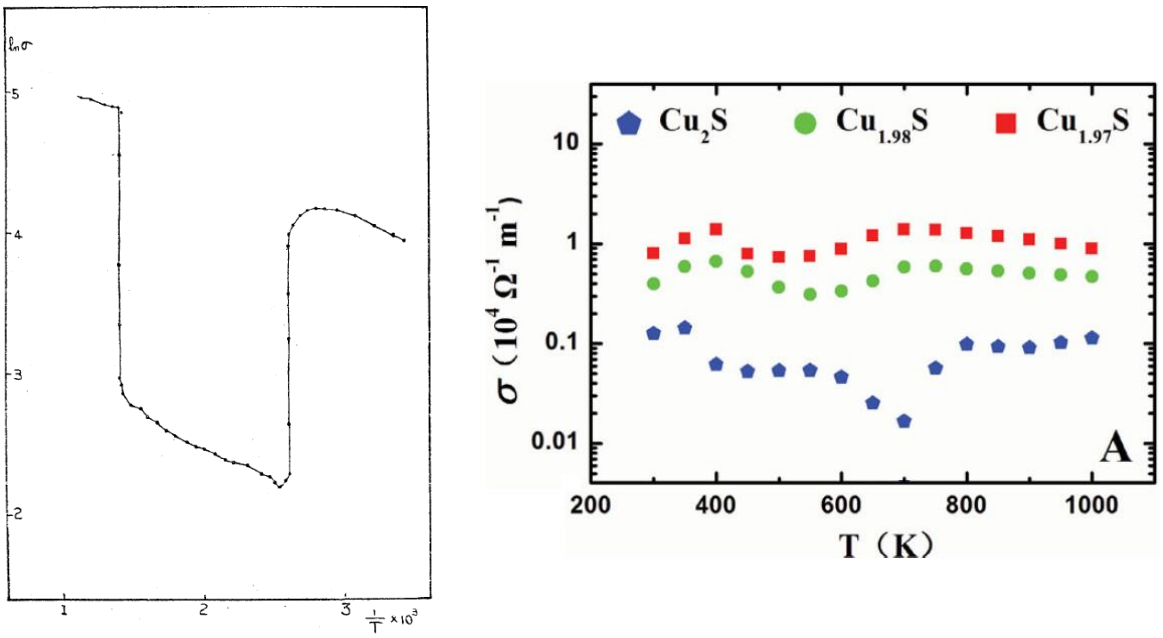

a b

Figure 20 (a) Electrical conductivity of Cu_2S experimental data plotted as natural logarithmic of electrical conductivity (S/cm) to temperature (Kelvin) (Hirahara, E., 1950); (b) Electrical conductivity of $Cu_{2-X}S$ (He, Y. et al, 2016).

Another study (table 2) supports results in figure 20. Although Garbee claimed that result at 550 ^oC had a potential to be biased, because it did not state the specimen's composition and phase at measured temperature, but it somehow matches result in figure 20. The difference of table 2 compared to figure 20 is the value of γ-chalcocite which is lowered by a factor of 10, starting from 0.91 S cm^{-1}. Unfortunately, table 2 do not have complete data from 437 ^oC to melting point, so comparison of α-chalcocite between Table 2 and figure 20 could not be made. As a conclusion, crystal structure of Cu_2S changes twice and affecting its thermal and electrical conductivity to be not linearly related to temperature.

Table 2 Electrical conductivity of Cu_2S in several sources (Garbee, A. K., 1969). *) In this temperature range, crystal structure changes. The peak and bottom value, unfortunately, is not obtained from the original reference.

Temperature (°C)	Specific Conductivity (mhos/cm)
0-200	0.91-0.6 *
550	0.3
1129-1250	47-91
1130-1480	25-97
1000-1450	45-160

8.2 Effect of dopant on Cu_2S conductivities

In Cu_2S, copper has 1 valence electron, while sulfur has 6 valence electrons. Through their complex monoclinic bonding, there are holes in this bonding that makes chalcocite a positive semiconductor. If an element like arsenic (As) with 5 valence electrons substitute the some copper elements, it could change the characteristic of electrical conductivity. One publication shows that Cu-As-S retain a p-type conductivity of Cu-S compound, although the stoichiometric ratio in the publication is covellite (Balow, R. B. et al., 2015).

Nevertheless, research of metals doping to Cu_2S other than arsenic are progressing quickly. Some metals dopants used were Zn and Fe, where they managed to enhance thermoelectric properties of Cu_2S (Vasuhi, A. et al., 2016). When dopant enters the matrix of mother compound, it creates vacancy along the lattices of the host, Cu. This way, the current carrier concentration increases (Bekenstein, Y., 2014).

Publications that analyze the effect of metallic sulfur in conductivities of Cu_2S at elevated temperatures were not found. The closest ones to that are the research shown by figure 19a and 20b, where some samples have excess sulfur in their stoichiometric formula. As a result, thermal conductivity and electrical conductivity are elevated to a higher level, along with different fluctuation pattern. Based on figure 19a and 20b, there is a possibility that arsenic doping might significantly change conductivities of copper matte.

8.3 Conductivities of FeS_2

Thermal conductivity of pyrite has a negative relation with temperature, whereas its heat capacity increases with temperature. However, no more prior research is found that analyze pyrite to over 300 ^oC. Starting from 26 W m^{-1} K^{-1} at room temperature, its thermal conductivity drops to 3 W m^{-1} K^{-1} at 300 ^oC (figure 21b). It is assumed that thermal conductivity of pyrite would keep its tendency because its heat capacity does not fluctuate either (see figure 21a). Its specific heat capacity increases from below 15 Cal mol^{-1} K^{-1} or 0.52 J g^{-1} K^{-1} to beyond 18 Cal mol^{-1} K^{-1} or 0.63 J g^{-1} K^{-1}; it was heated up from room temperature to 700 K.

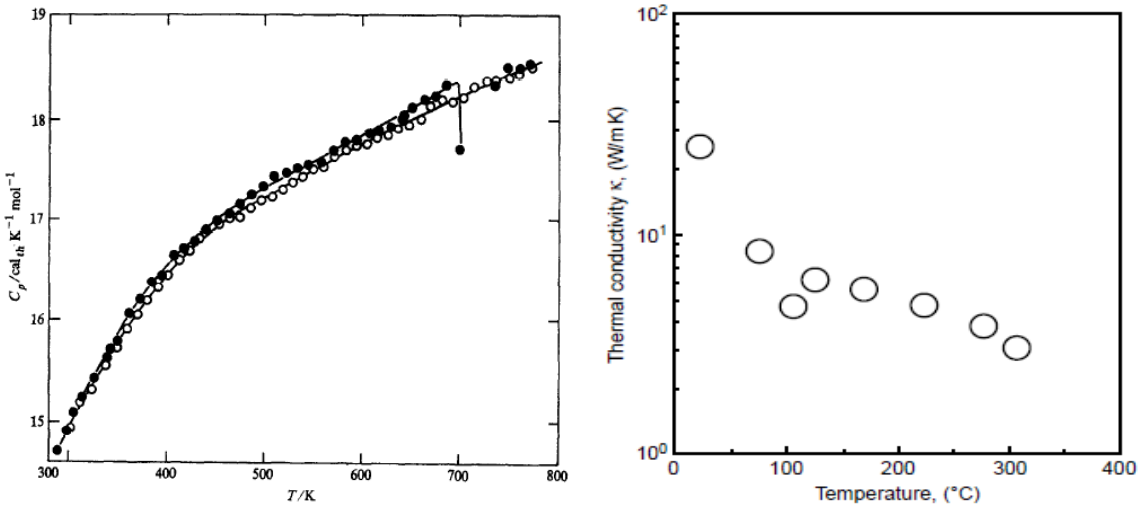

a b

Figure 21 (a) heat capacity of marcasite (black dots) and pyrite (white dots) at elevated temperatures (Grønvold and Westrum, 1976); (b) thermal conductivity of natural pyrite from the mine (Kato, K. et al., 1997)

Pyrite can be either n-type or p-type semiconductor. Electrical resistivity of FeS_2 is 0.5-500 ohm m, whereas Cu_2S is 10^{-4}-2.3x10^{3} ohm m, although the temperature range is not mentioned (Pearce et al., 2006). Marinage also reported the resistivity of pyrite as both negative and positive (see figure 22), which is similar to Pearce in terms of p-type pyrite. The electrical conductivity of p-type pyrite is lower than chalcocite at most temperatures. Exception is at mid-range temperature, where chalcocite becomes high-chalcocite and causing its electrical conductivity to drop.

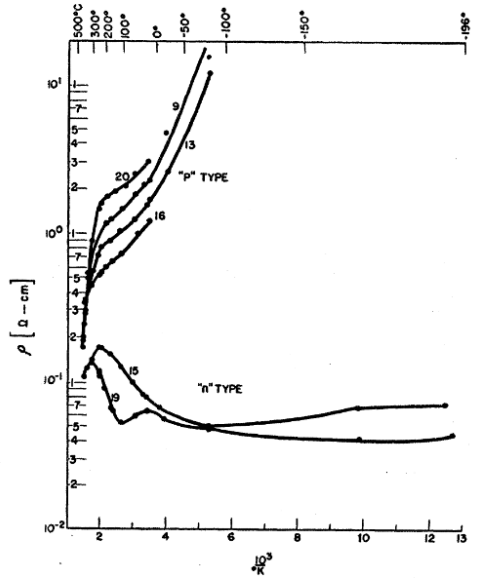

Figure 22 Electrical resistivity of natural crystal of pyrite (Marinage, J. C., 1954)

8.4 Conductivities of Cu_5FeS_4

Bornite, Cu_5FeS_4, shows a very good semiconductor behavior, comparable to that of chalcocite. It has a very low thermal conductivity in temperature region 100 to 700 K, from 0.2 to 0.5 W m^{-1} K^{-1} (see figure 23a). The electrical conductivity rises from 0.05 S/cm at ambient temperature to around 100 S/cm at 700 K (see figure 23b). Although bornite has three phases that change with temperature, however, there is no fluctuation in its electrical conductivity behavior. The specific heat capacity of bornite is also measured from 0 K to room temperature. It increases from 0 to 0.48 J g^{-1} K^{-1} (Qiu, P. et al., 2014). The three reviewed sulfides have quite similar specific heat capacity.

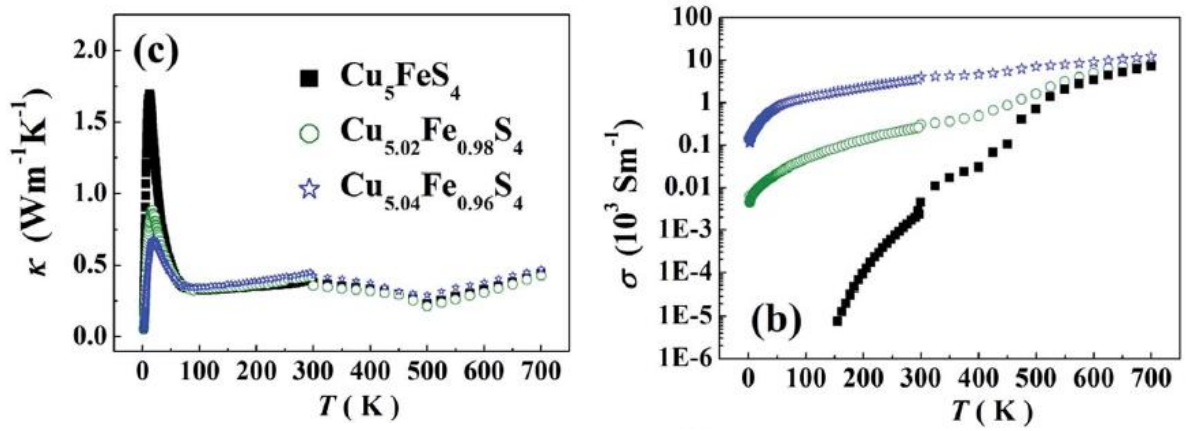

a B

Figure 23 (a) Total thermal conductivity and (b) electrical conductivity of normal bornite and stoichiometrically altered ones. (Qiu, P. et al., 2014)

8.5 Conductivities of FeS

As mentioned in subsection 2.2, Pearce stated that FeS character depends on the stoichiometry. One of the polymorphs, troilite (FeS), shifts from semiconductor into a metal once it is heated up to around 140 ^oC (411 K) and shifted back to semiconductor at 315 ^oC. Another variant, called pyrrhotite ($Fe_{1-X}S$), starts as metallic material at ambient condition. It changes into semiconductor at around 315 ^oC. However, pyrrhotite is quite weird because its synthetic compound is a semiconductor material, while the natural one is a conductor.

In the end, no valuable information was obtained regarding thermophysical properties of FeS polymorphs. Only one publication managed to discuss thermal diffusivity, but it was measured only from 80 to 300 K (Tsatis and Theodossiou, 1982). Another publication by Grønvold and Westrum discussed heat capacity of FeS, which was higher than Cu_2S, in temperature range of 8 to 350 K. They increased from 0 to 13.68 Cal mol^{-1} K^{-1} or 0.65 J g^{-1} K^{-1}, as shown in table 3. It is evident here that specific heat capacity is sensitive to composition and even stoichiometry.

Nevertheless, both these temperature ranges are far from covering the temperature target of this thesis.

Electrical resistivity of FeS-pyrrhotite at room temperature is around 3 x 10^{-4} Ω cm. It shifts to 10^{-2} - 10^{-3} Ω cm once its crystal structure changes at 315 °C. They are 2 order of magnitude-higher compared to Cu_2S (Pearce et al, 2006). Another publication regarding FeS-troilite shows that its resistivity ranges from below 10^{-2} to 10^{-4} Ω cm, measured between 350 and 450 K (Coey, J. et al., 1976). Troilite is a p-type semiconductor (same with Cu_2S), while pyrrhotite is a p-type metal up to 225 °C; above this, it becomes n-type (Pearce et al, 2006).

Table 3 Experimental specific heat capacity of FeS variant (Grønvold and Westrum, 1958).

T, °K	C_p	$S°-S_0°$	$\frac{H°-H_0°}{T}$	C_p	$S°-S_0°$	$\frac{H°-H_0°}{T}$
	Iron-rich pyrrhotite ($Fe_{1.000}S$)			Sulfur-rich pyrrhotite ($Fe_{0.877}S$)		
10	0.0269	0.0090	0.0067	0.0812	0.0207	0.0173
20	0.262	0.0795	0.0608	0.479	0.178	0.133
30	0.863	0.289	0.219	1.395	0.511	0.372
40	1.670	0.645	0.479	1.893	0.973	0.683
50	2.535	1.110	0.803	2.633	1.474	0.998
60	3.393	1.648	1.163	3.397	2.021	1.334
70	4.212	2.233	1.541	4.143	2.601	1.682
80	4.996	2.847	1.924	4.875	3.202	2.036
90	5.718	3.478	2.306	5.569	3.818	2.391
100	6.365	4.115	2.680	6.191	4.437	2.740
110	6.955	4.750	3.042	6.758	5.054	3.080
120	7.504	5.379	3.392	7.281	5.665	3.408
130	7.998	5.999	3.727	7.763	6.267	3.725
140	8.429	6.608	4.048	8.202	6.858	4.029
150	8.823	7.203	4.353	8.597	7.438	4.321
160	9.173	7.784	4.644	8.957	8.005	4.600
170	9.491	8.350	4.920	9.277	8.557	4.865
180	9.779	8.901	5.182	9.570	9.096	5.119
190	10.04	9.436	5.431	9.843	9.621	5.360
200	10.28	9.958	5.667	10.09	10.132	5.590
210	10.51	10.465	5.892	10.32	10.630	5.810
220	10.71	10.958	6.107	10.53	11.115	6.020
230	10.90	11.438	6.311	10.74	11.588	6.221
240	11.08	11.906	6.506	10.94	12.049	6.413
250	11.26	12.362	6.693	11.12	12.499	6.598
260	11.43	12.807	6.872	11.30	12.939	6.775
270	11.60	13.242	7.044	11.47	13.369	6.946
280	11.76	13.667	7.209	11.64	13.789	7.111
290	11.93	14.082	7.369	11.80	14.200	7.270
300	12.11	14.490	7.524	11.95	14.603	7.423
350	13.68	16.459	8.277	12.68	16.501	8.123
273.15	11.65	13.377	7.097	11.53	13.503	6.999
298.15	12.08	14.415	7.496	11.92	14.529	7.396

8.6 Conductivities of solid silicate slag and slag melt

Thermal diffusivity and specific heat capacity of silicate slag behavior at elevated temperatures are shown in figure 24. Thermal diffusivity of crystalline silicate slag decreases smoothly, from 9 x 10^{-7} to 6 x 10^{-7} m^2 s^{-1}, and settle down at 800 K. Meanwhile, thermal diffusivity of glassy slag is quite stable, 3 x 10^{-7} to 4 x 10^{-7} m^2 s^{-1}, in the whole temperature range. Their specific heat capacities, on the other hand, are slightly different. Glassy slag has specific heat from around 700 J kg^{-1} K^{-1} at 300 K to 1000 J kg^{-1} K^{-1} at 1150 K. Specific heat of crystalline slag is from 650 J kg^{-1} K^{-1} at 300 K to around 800 J kg^{-1} K^{-1} at 1150 K. The increasing specific heat of glassy slag was inferred to be the result of endothermic glass structure transition. Glass transition temperature of the specimen in the reference was 1153 K.

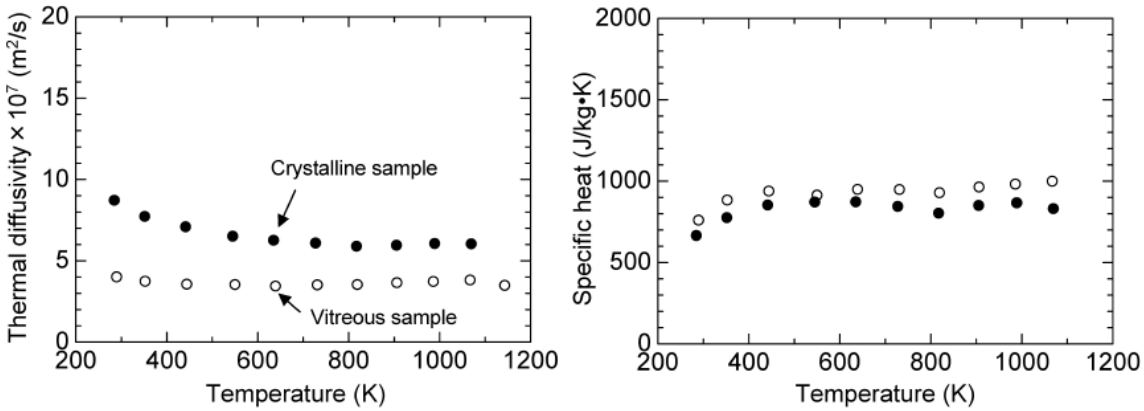

a b

Figure 24 Thermal diffusivity (a) and specific heat capacity (b) of solid crystalline slag and glassy slag, with composition by wt-% of 40CaO-40SiO_2-20Al_2O_3. (Nishioka, K. et al., 2006)

Figure 25 shows that thermal conductivity of glassy slag, which is 67 wt-% silica, increases from 0.8 to 1.2 W m^{-1} K^{-1}, at room temperature to T_g. After T_g, it smoothly drops to below 0.5 W m^{-1} K^{-1} at 1000 ^oC. As silica content in the slag is reduced and balanced with the basic oxides, its structure become crystalline. Thermal conductivities starts at 2.5 W m^{-1} K^{-1} and keeps dropping as temperature increases, reaching as low as 0.3 W m^{-1} K^{-1} at 1000 ^oC .

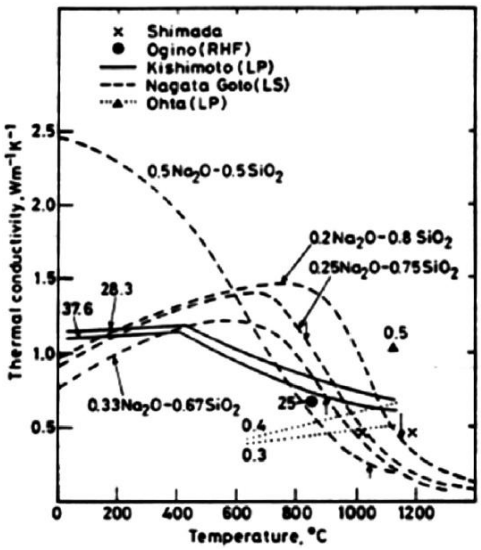

Figure 25 Characteristic of thermal conductivities of Na_2O-SiO_2 system based on silica content and temperature (Mills and Susa, 1992).

Electrical conductivity behaves in opposite manner to thermal conductivity, where it has positive relation with temperature. Increased free cation activity in solution raises its electrical conductivity. Free cations come from basic oxides, e.g. FeO and CaO. Table 4 shows that value of electrical conductivity is significantly bigger in slag with higher FeO and CaO.

Table 4 Experimental electrical conductivity of silicate slag, at 1773 K (Hoster and Pötschke, 1983 as cited by Wang, L., 2009)

Composition			Exp. Data
FeO [wt%]	SiO_2 [wt%]	CaO [wt%]	Elec. Conductivity [S/cm]
10	69.35	20.65	0.093
20	61.64	18.36	0.147
10	56.65	33.35	0.214
20	50.34	29.66	0.342
10	45.21	44.79	0.475
20	40.17	39.83	0.664

An increase of about 300 ^oC has increased the electrical conductivity by almost six-fold. Between 800-1100 ^oC, silicate slag electrical conductivity ranges from 0.043 to 0.25 S cm^{-1}, as shown in Table 5. This value is less than copper matte conductivity by 2 order of magnitude.

Table 5 Electrical conductivity of silicate slag, melting point = 1332 K (Ejima et al., 1968)

Temp (K)	SiO_2	CaO	PbO	Elec. Cond. [S/m]
1073	43.65	12.70	43.65	4.28
1173				8.58
1273				15.37
1373				25.20
1473				38.56

As explained in section 6.2, thermal conductivity of slag melts decrease with temperature. Meanwhile, electrical conductivity typically increases if thermal conductivity of slag decreases, as covered in section 5.5. This theory agrees with experimental data from prior research in figure 26 and Table 6.

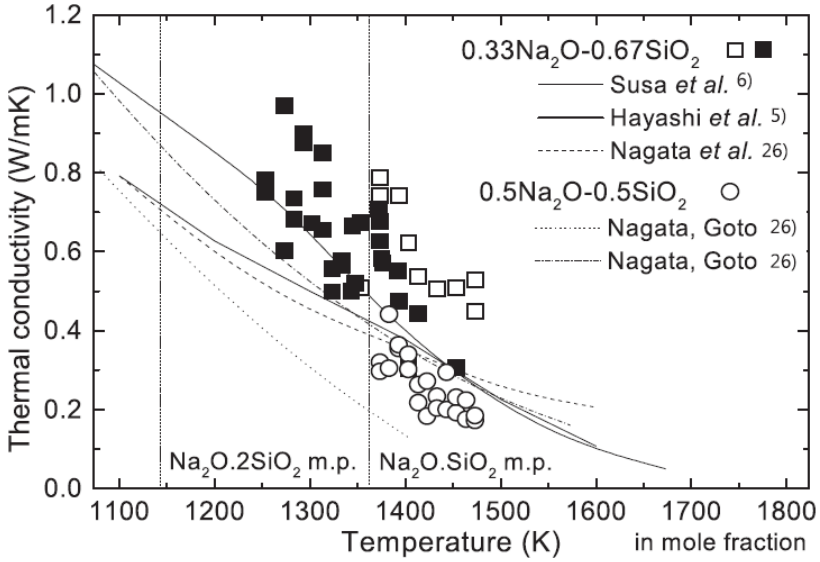

Figure 26 Thermal conductivity measurement of slag melts, depicting both glassy slag and crystalline (Kang, Y. et al., 2014).

Table 6 Electrical conductivity of molten silicate slag systems (Sun, C. and Guo, X., 2010)

Type of molten slag	*w*/%						Electrical conductivity/(S·m^{-1})				
	CaO	MgO	SiO_2	Al_2O_3	FeO	NiO	1 573 K	1 623 K	1 673 K	1 723 K	1 773 K
Based slag	25	7	58	10	0	0	1.4	2.3	3.8	5.3	7.8
4%FeO-containing slag	24	6.7	55.7	9.6	4	0	1.6	2.6	4.0	5.7	8.6
8%FeO-containing slag	23	6.4	53.4	9.2	8	0	2.0	3.3	5.1	7.4	10.6
12%FeO-containing slag	22	6.2	51	8.8	12	0	3.0	4.7	7.2	10.1	14.4
4%NiO-containing slag	24	6.7	55.7	9.6	0	4	1.6	2.6	4.2	6.1	8.8
8%NiO-containing slag	23	6.4	53.4	9.2	0	8	2.0	3.2	5.2	7.6	11.0
12%NiO-containing slag	22	6.2	51	8.8	0	12	2.5	4.1	6.4	9.5	13.4

9 Experimental setup

This chapter serves to conclude the arrangement of thermal conductivity analysis that were conducted in cited literatures. In addition, similar experiment was conducted by Juhani Heimo in order to analyze thermal conductivity of titanium slag (Heimo, J., 2018). Therefore, many aspects of the experimental setup in this thesis uses his work as a reference. The order of sub-sections reflects the order of experiment. This experimental investigation is novel because thermal conductivity of industrial copper matte and the effect of its copper grade to it has never been discussed in any publication.

9.1 Samples and chemical analysis

There are eight samples in this experiment: three samples of copper matte, three samples of slag, and two samples of As-doped copper matte. Three samples of copper matte are distinguished by its copper content, i.e. 60-62 wt-%, 63-65 wt-%, and 66-68 wt-%. Three samples of slag are differentiated by its iron to silica ratio, the most important ratio in determining slag quality. The ratio of SiO_2 to Fe is between 0.7-0.8 (Schlesinger et al., 2011). Lastly, two As-doped coper matte samples that contain different arsenic percentage, 0.255 and 0.5 wt-%, and similar copper percentage, 63-65 wt-%.

All the samples and their chemical analysis are provided by Outotec Finland Oy. The chemical analysis was done by using ICP (Inductive Coupled Plasma). Magnetite concentration was provided as Satmagan analysis. Composition contributes to thermal conductivity magnitude and thus the comparison between copper matte with different copper grade could shed light to relation between industrial copper matte grade and thermal conductivity. Slag samples were compared to analyze the effect of Fe/SiO_2 ratio to thermal conductivity. As-doped copper matte samples have similar copper content to one of normal copper matte, therefore they were compared to analyze effect of arsenic to thermal conductivity. Detailed elemental compositions are shown in table 7.

Table 7 ICP analysis result of all samples, with exception of normal matte samples.

Element	Unit	Slag			Matte				
		S1	S2	S3	DM1	DM2	M1	M2	M3
ICP Al	wt-%	4.40	3.01	3.06	0.02	0.01			
ICP Fe	wt-%	33.80	36.30	38.30	9.13	10.60			
ICP Ni	wt-%	0.08	0.09	0.08	0.80	0.72			
ICP Cu	wt-%	1.09	1.34	1.08	65.20	64.00	60-62	63-65	66-68
ICP Zn	wt-%	3.11	3.57	3.48	0.82	0.84			
ICP As	wt-%	0.15	0.23	0.20	0.59	0.26			
ICP Pb	wt-%	0.39	0.55	0.38	0.75	0.75			
SiO_2	wt-%	35.60	32.00	30.80					
Magnetite	wt-%	9.40	12.90	12.60					
S (calculated)	wt-%				21.10	20.00	from Cu_2S (15-17%)		
Fe/SiO_2	-	0.95	1.13	1.24					

If copper matte grade is lower, presumably its iron content is higher. Thermal conductivity of copper matte might be roughly assumed and compared to each other from average of each sample. However, no publication has been made regarding exact thermal conductivity of FeS, except for its specific heat capacity. If thermal conductivity of FeS is averagely higher than Cu_2S, then thermal conductivity of industrial copper matte has negative relation with copper grade. The hypothesis is FeS thermal conductivity should be close to FeS_2 because of their quite similar specific heat capacity, causing thermal conductivity of industrial copper matte to have negative relation with its copper grade and higher than Cu_2S.

9.2 Microstructure and elemental distribution analysis

Microstructure is critical in analyzing thermal conductivity. The existence of defects and impurities, distribution of the elements, and the grain size contribute to thermal conductivity. The utilization of SEM-EDS is therefore indispensable to find those three characters of each sample.

All samples were molded into resin to be ground and polished. The grinding grit size were escalated in the following order: 240, 400, 800, 1200, and 2500. Next, they were polished by 3µm and 1µm consecutively. Prior to carbon coating, they were rinsed in ethanol solution and dried by using compressed air. The used instruments were shown in figure 27. EDS measurement was applied without standard because the samples were heterogeneous industrial samples. After each sample was analyzed for its thermal conductivity, it was then cut and re-analyzed in SEM-EDS in order to examine its 3D microstructure.

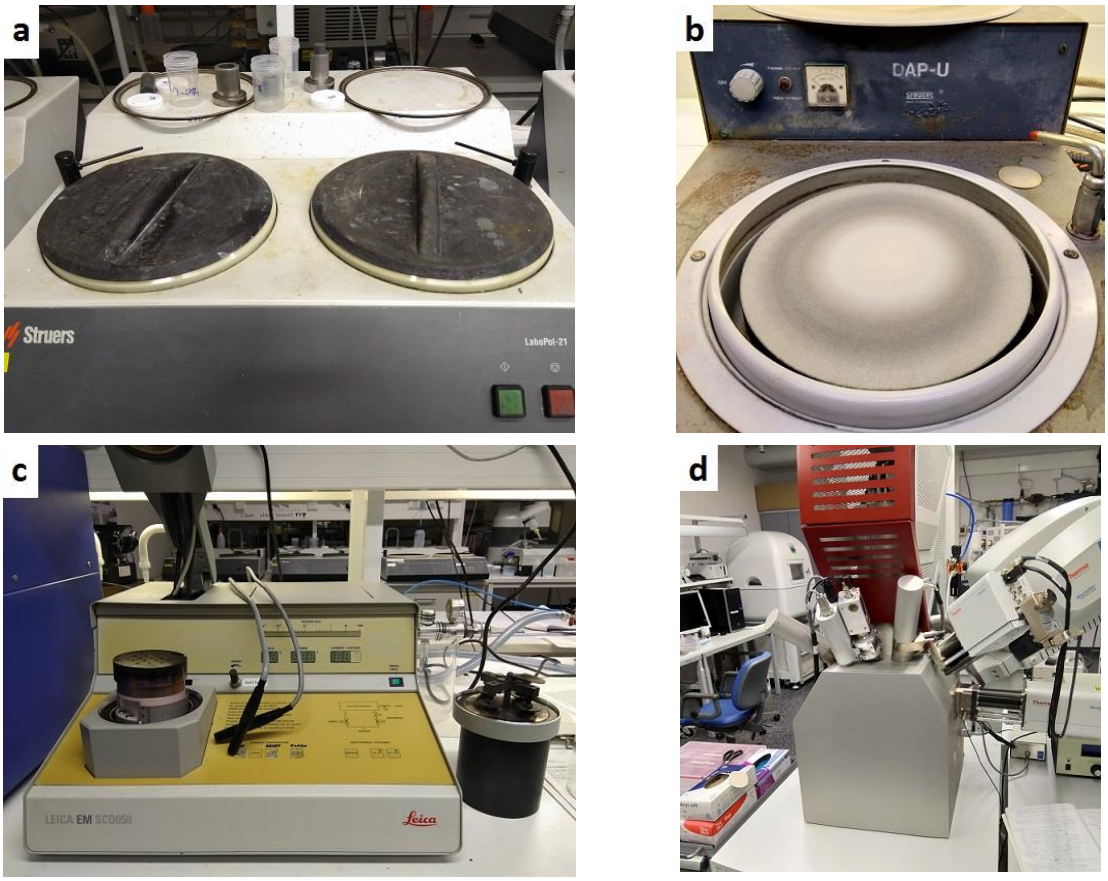

Figure 27 The set of apparatus for preparing a sample of SEM analysis: (a) Grinding table, (b) polishing table, (c) carbon coating, and (d) SEM-EDS.

9.3 Phase analysis

SEM/EDS gives weight and atomic ratio of each element in the sample. From the atomic ratio, the compound formulas were speculated, which were not really accurate. XRD was used only for slag samples to ascertain the phases of compounds in the slag. XRD needs powder as its input, therefore the slag samples were crushed and milled in Retsch XRD-Mill McCrone for 10 minutes. In the milling tube, ± 15 ml of ethanol was introduced for a wet milling process. Wet milling produces finer particles, which was good for XRD. Finally, the wet powder was put into a glass container and dried in 80 ^{o}C furnace for 15 hours. XRD sample preparation tools are shown in figure 28. Parameters used in the measurement are shown in table 8, while its result are shown in Appendix B.

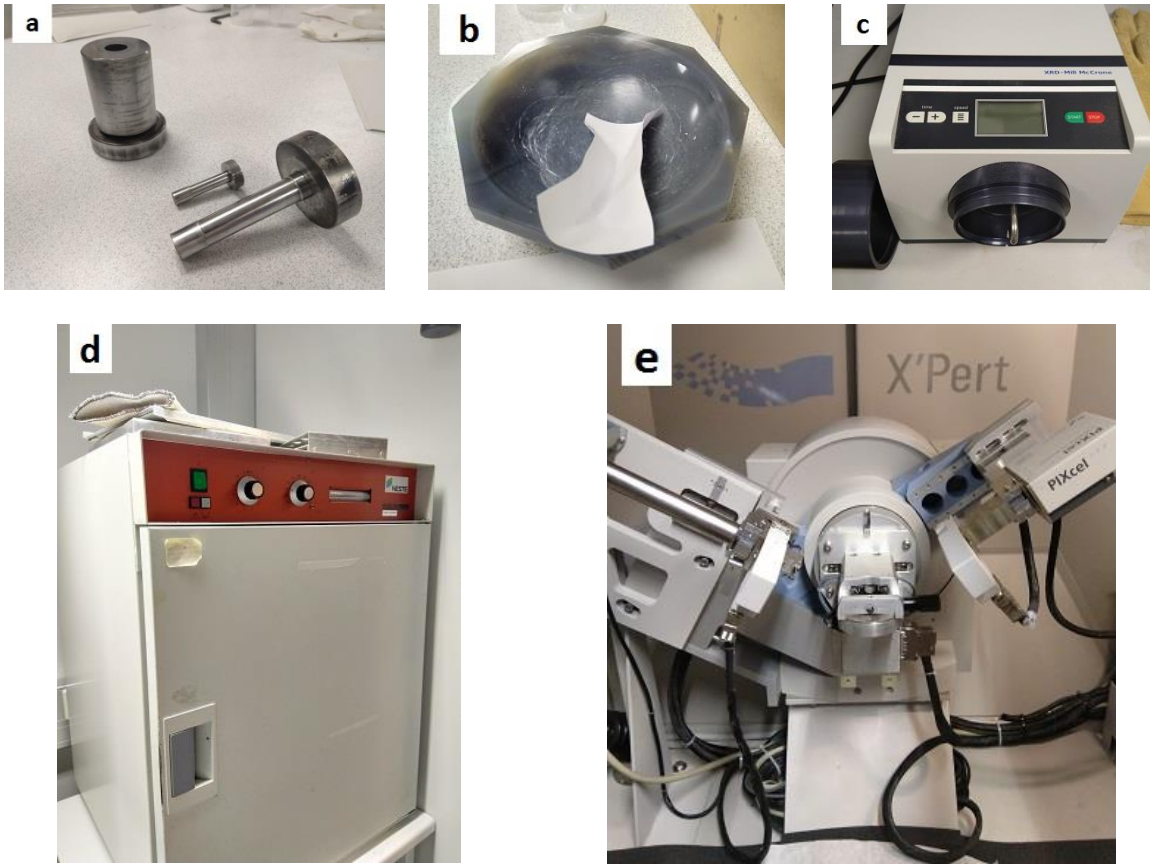

Figure 28 XRD instrument set for preparation and measurement: (a) crusher, (b) mortar, (c) XRD mill, (d) low-temperature furnace, and (e) XRD.

Table 8 Parameters of XRD Analysis

Mask	10 mm
Degree of Measure	10 – 90°
Degree per Step	0.013°
Time per Step	60 seconds
PHD level	35-100%
Sample Rotation	Continuous
Phases Quantification	Rietveld Analysis

9.4 Thermal conductivity measurement

All the samples were cut into around 2.5 mm-thick cylinders with 12.6 mm of diameter. Next, it was polished to have a flat and smooth surface, which was crucial for homogeneous irradiation. Surface porosities, especially on slag samples, made each surface was not level, thus they were filled with wet silicon carbide powder. Last step, sample surfaces were coated with thin graphite layer to promote black body absorption.

One of the LFA type manufactured by NETZSCH is NETZSCH 467 HT *HyperFlash*®, capable of heating the sample from room temperature to 1250 °C, as predetermined in the objective. The maximum heating rate is 50 °C/min. Meanwhile, the heating rate in previous research is

around 100 °C/30 min to ensure a precise thermal conductivity measurement over the temperature range (Heimo, J., 2018). The atmosphere of sample chamber is nitrogen. The heating and measurement must be done at once without any pause that could drop the temperature.

The experiments were originally planned to be carried out in a Nordic research institute. However, the instruments had a technical problem and could not be fixed within the schedule of this research. Therefore, all samples were sent to the Applications Laboratory of manufacturer of LFA instrument, NETZSCH-Gerätebau GmbH, Wittelsbacherstr in Selb, Bavaria, Germany. The procedure from this laboratory is to carry out the experiment without intervention from any parties. LFA itself is shown in figure 29.

Figure 29 One example of LFA instrument manufactured by NETZSCH [www.netzsch-thermal-analysis.com].

In addition, NETZSCH also measure specific heat capacity of one normal copper matte sample and one slag sample at room temperature to 1200 °C by using NETZSCH DSC 404F1, a differential scanning calorimetry manufactured by NETZSCH. The applied heating rate was roughly 20 °C/min. The result would be valuable in observing the comparing character of sample to pure sulfide in reference.

Depending on the compound, e.g. Cu_2S, elevated temperature could change the crystal structure and cooling process triggers the diffusion/migration of elements, causing them to be differently distributed from the original condition (before any heating). Hence, one sample can only be experimented once.

Thermal expansion was measured by using dilatometer. Each specimen for dilatometer must be cut into a 50 mm long-rod to fit the chamber. If not sufficient enough, then alumina pieces

were used to compensate for it. The surface size is 8 x 8 mm. Its maximum heating capacity is 1150 °C, with 2 °C/min of heating rate. The atmosphere of the chamber is argon. Dilatometer itself is shown in figure 30.

Figure 30 One example of dilatometer manufactured by NETZSCH [www.netzsch-thermal-analysis.com].

9.5 Internal structure analysis

Internal condition of a medium affects thermal conduction process in it. Therefore, some samples are introduced to x-ray computed tomography (XCT) for observation of their internal structure. Significant vacancies, cracks, and inclusions surely affects the thermal conductivity and could make the samples become less comparable to each other.

Figure 31 shows XCT instrument that was used in this thesis. The instrument type was GE phoenix v|tome|x s, operated by Geological Survey of Finland (GTK), Espoo, Finland. All three samples were scanned at once using the 240 kV microfocus tube, using 0.5 mm of copper as a beam filter. Accelerating voltage was 220 kV and tube current was 45 µA. Spatial resolution was 10.09 µm. The scan was done with a helical trajectory, with a total rotation angle of 406°, 2285 projections and a vertical feed of 23.04 mm.

Figure 31 XCT instrument used in this experiment by GTK.

10 Results and discussion

10.1 Microstructure analysis

Since microstructure and phase composition influence thermal conductivity, all samples are analyzed by using SEM-EDS (scanning electron microscope-energy dispersive x-ray spectroscopy). Observation shows that all samples have heterogeneous microstructure, which might be the result of slow cooling process upon sample preparation. In order to fully comprehend the heterogeneous microstructure, publications regarding solidification and segregation are reviewed (Appendix C).

10.1.1 SEM-EDS analysis of matte samples

Matte samples are named M1, M2, and M3 based on their copper grade. The characteristic of industrial samples are heterogeneous, as shown in figure 32, where the phases are not well mixed. From the microstructure observation of sample M1, there are four phases in the copper matte sample: gray area, dark gray dots, light gray whiskers, and white dots or lines.

The gray area are the matrix of the phases, composed of copper and iron sulfide phase (area A & B of table 9). The dark gray dots, are composed of iron oxide (point 3 & 5). The atomic ratio and weight percentage of iron oxide shows Fe-O exists as both FeO and Fe_2O_3. FeO normally goes to slag phase during the smelting process. Based on how these spots are evenly spread over the whole area, they are most likely not entrapped slag (figure 32c). They might be droplets formed at high temperature due to oxidation of the iron sulfide by the process air.

Next, the light gray area is copper metal (point 1 of table 9). Figure 32b shows a concentrated copper that fills up a big cavity and cracks. This copper might be copper from saturated copper matte phase which diffuses to adjacent empty space at low temperature. Cavities could be created by volume shrinkage during cooling. However, this kind of big copper protrusion is not found at another location. Binary phase diagram of copper sulfide in section 2.1 thermodynamically support this phenomena.

Lastly, the white lines which have similar composition to white dots are most likely phases that segregate at grain boundaries. Segregation of impurity atoms are easier to take place in grain boundaries due to its higher energy state compared to grain (Callister W. D., 2001). They mostly contain Ni and Pb, which are not found in the main copper matte phase (point 2 & 4 of

table 9). The white metallic dots are scattered in a similar manner to iron oxide dots. Their similarity is that both nickel and FeO have higher melting point than copper sulfide matrix.

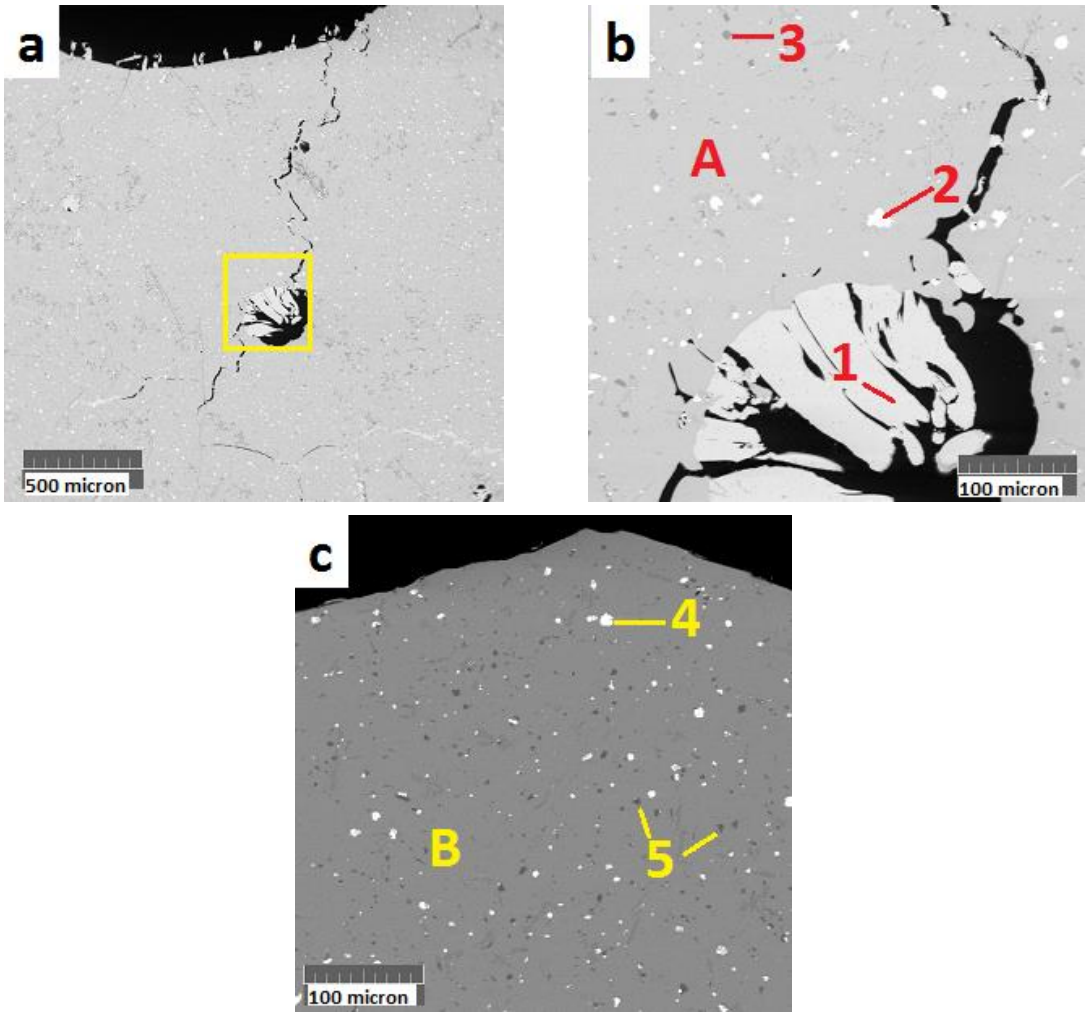

Figure 32 Sample M1: (a) displaying middle part of the sample (133x); (b) zooming in of the yellow box (666x); and (c) the edge part of the sample (666x). *Number in parentheses shows degree of magnification.*

Table 9 EDS analysis of sample M1 in wt-%

	O	*Al*	*Si*	*S*	*Fe*	*Ni*	*Cu*	*Sn*	*Pb*	*Phases*
1	0.3	0.3	-	0.1	-	-	99.4	-	-	Cu
2	1.4	0.2	-	-	0.5	24.3	2.7	0.8	70.6	Pb-Ni
3	29.1	-	0.3	-	68.3	-	1.9	-	-	Fe-O
4	2.8	-	-	-	0.9	29.9	4.1	10.0	52.3	Pb-Ni-Sn
5	28.6	0.2	0.4	0.6	67.0	-	3.3	-	-	Fe-O
A	2.1	0.04	-	23.3	11.7	-	62.9	-	-	Cu-Fe-S
B	2.3	0.2	-	22.9	11.5	-	63.1	-	-	Cu-Fe-S

Diffusion takes time to complete before solidification starts. If a quenching was applied in preparing samples, then the phases would be homogeneous. Both sample M2 (figure 33) and

M3 (figure 34) show heterogeneous microstructures that are similar to M1. The three matte samples also have numerous micro cracks across the surface. These facts justify that their cooling processes are similarly slow.

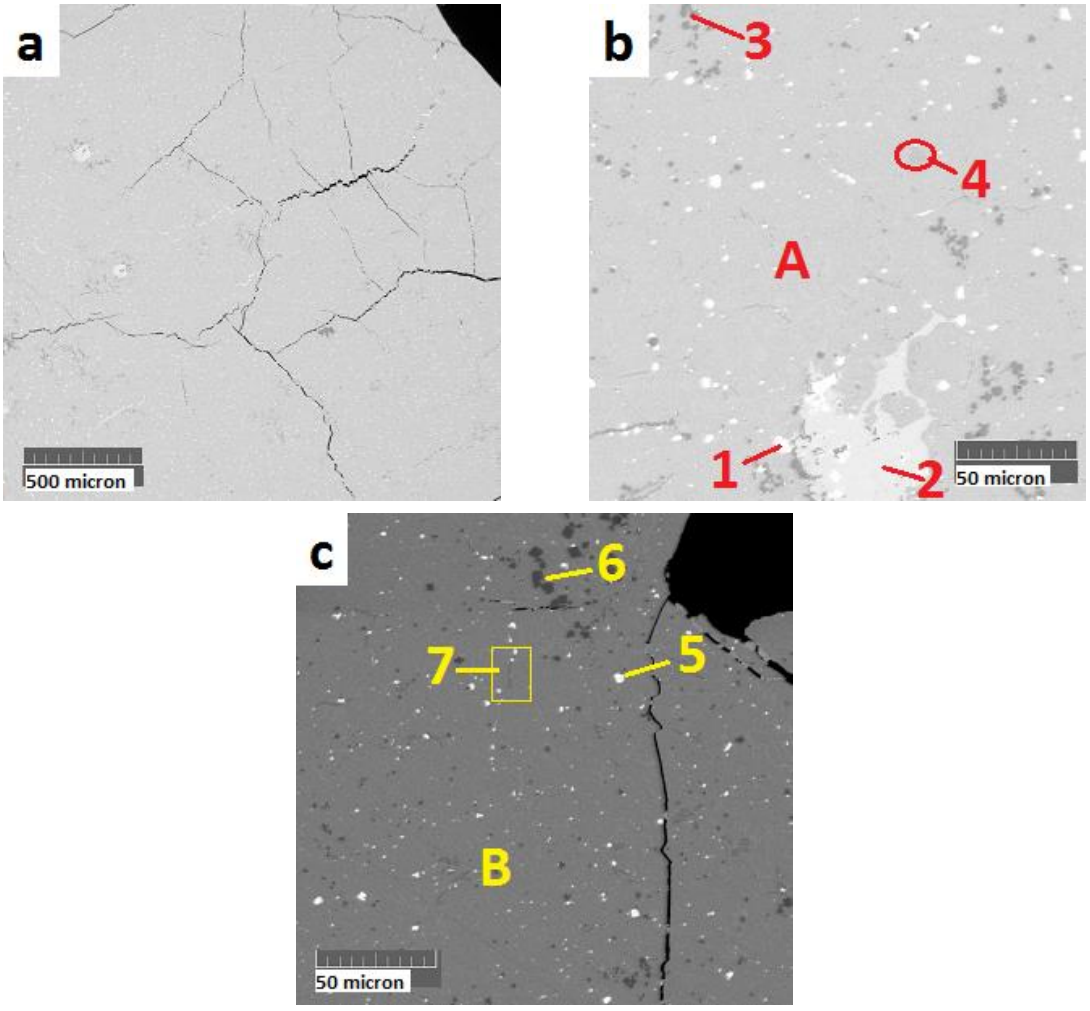

Figure 33 Sample M2: (a) zooming out of sample (133x); (b) zooming in middle part (1340x); and (c) zooming in edge part of the sample (1340x).

Table 10 EDS analysis of sample M2 in wt-%

	O	*Al*	*S*	*Fe*	*Ni*	*Cu*	*Zn*	*As*	*Ag*	*Ta*	*Pb*	*Phases*
1	0.9	0.5	-	2.3	23.2	11.4	-	1.2	2.3	-	58.4	Pb-Ni-Cu
2	0.7	0.4	0.2	2.1	-	95.5	-	-	1.0	-	0.1	Cu
3	24.3	0.3	2.4	62.3	1.3	9.4	-	-	-	-	-	Fe-O
4	0.8	-	29.5	11.5	-	-	44.7	-	-	13.6	-	Zn-Ta-Fe-S
5	1.0	0.8	-	2.2	16.2	16.4	-	-	-	-	63.5	Pb-Ni-Cu
6	27.6	0.5	0.4	68.1	-	3.1	-	-	-	-	-	Fe-O
7	0.9	0.9	28.2	8.0	-	27.1	35.0	-	-	-	-	Zn-Cu-S
A	1.7	0.3	21.9	8.4	-	67.6	-	-	-	-	-	Cu-Fe-S
B	2.9	0.6	21.4	10.2	-	64.9	-	-	-	-	-	Cu-Fe-S

Composition of sample M2 (table 10) is close to M1, containing copper (point 2), copper matte (area A & B), iron oxide (point 3 & 6), and lead-nickel metal phase (point 1 & 5). Their close

values and microstructure give possibility to a similar thermal conductivity coefficient. There are some minor zinc sulfide phases at several locations of sample M2 (point 4 & 7). Zinc sulfide is also found in sample M3 (point 6, table 11).

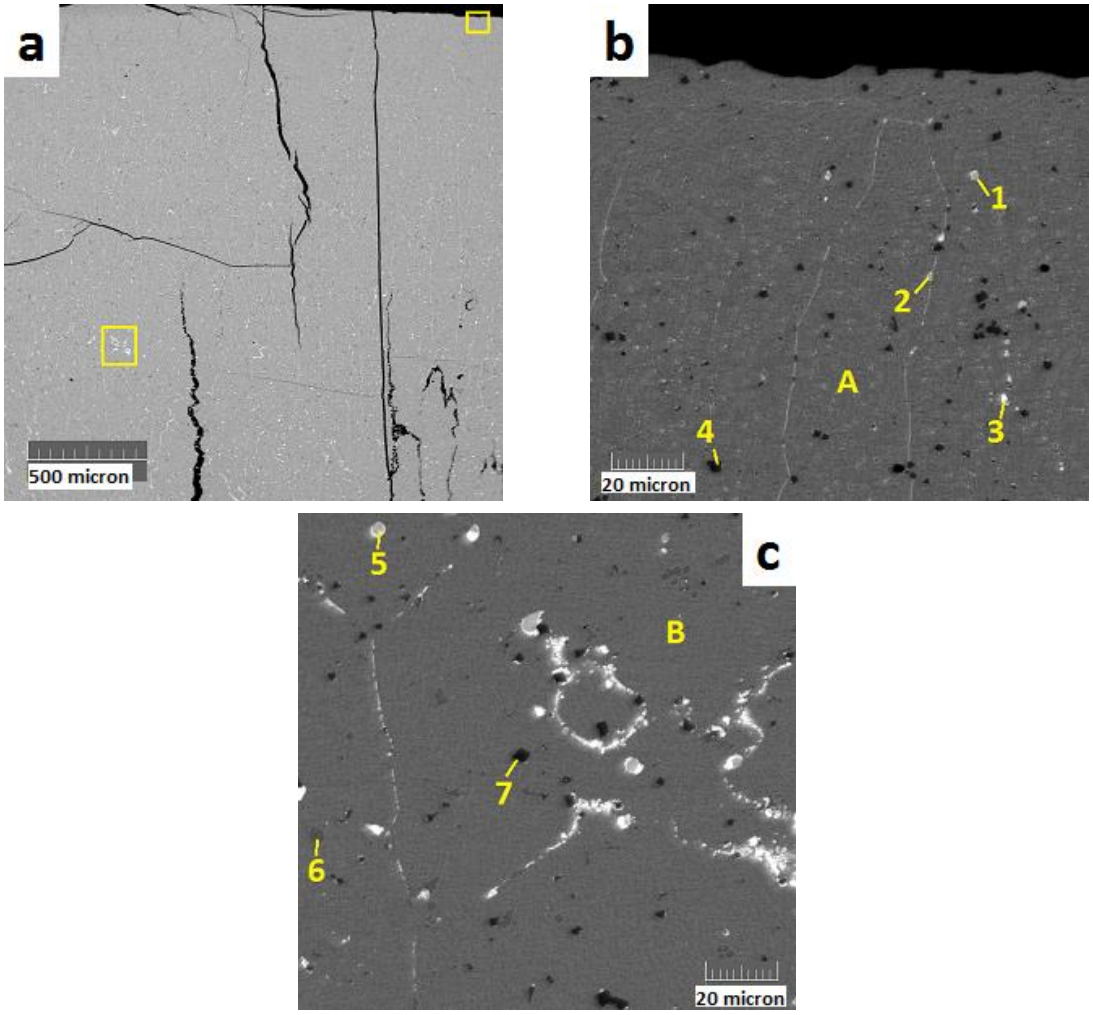

Figure 34 Sample M3: (a) displaying a part of the sample (134x); (b) zooming in of the middle part (2000x); and (c) zooming in the edge part of the sample (2000x).

Table 11 EDS analysis of sample M3 in wt-%

	O	Al	Si	S	Fe	Ni	Cu	Zn	As	Mo	Ag	Sb	Ta	Pb	Phases
1	0.3	-	-	5.2	1.9	44.6	18.4	-	24.3	-	-	5.3	-	-	Ni-As-Cu-S
2	0.6	-	-	9.5	3.1	27.4	30.7	-	14.1	-	9.2	2.7	-	2.7	Cu-Ni-As-S
3	0.5	-	-	-	2.6	16.2	29.0	-	0.1	48.0	3.8	-	-	-	Mo-Cu-Ni
4	23.9	-	0.2	4.0	56.1	-	15.8	-	-	-	-	-	-	-	Fe-Cu-O
5	0.3	-	0.1	3.2	1.5	46.5	13.0	-	23.3	-	2.5	5.1	-	4.5	Ni-As-Cu-S
6	0.9	0.1	-	27.9	5.8	-	-	37.2	-	-	-	-	28.1	-	Zn-Ta-Fe-S
7	26.9	-	0.2	3.1	56.2	-	13.5	-	-	-	-	-	-	-	Fe-Cu-O
A	1.6	-	-	21.5	5.5	-	71.2	-	-	-	-	-	0.5	-	Cu-Fe-S
B	1.5	-	-	21.1	5.2	-	72.2	-	-	-	-	-	-	-	Cu-Fe-S

One distinction of sample M3 is the presence of arsenic (table 11). Arsenic exists as metallic phase and attached to nickel-copper metal (point 1, 2, & 5). Arsenic does not stick with heavier

metals, which in this case are molybdenum (point 3). Order of atomic mass from heavy to light is lead, molybdenum, arsenic, copper, and nickel. This might indicate that arsenic tends to stick with lighter metals.

Naturally, arsenic exists as sulfide in chalcopyrite concentrate. Yet in M3, arsenic is not left in matte phase anymore. It groups up with metallic phases in the sample and somehow changes the microstructure of matte a bit. Previously, in M1 and M2, there is only one bright metal phase, containing nickel and lead (point 1 & 5, table 10). In M3, metallic phases segregate into white and light gray metal phases.

Beside arsenic, M3 contains much higher nickel concentration (point 1 & 5 of table 11) than M2. The iron oxide phases in M3 contains 13 to 15 wt-% copper as well (point 4 & 7). Despite all the differences, the concentration of copper in each copper matte phase follows ICP analysis in section 9.1. Since copper matte phases are still the representative phase in all three matte samples (area A & B of table 9-11), thermal conductivity of each matte sample is comparable based on their copper content.

10.1.2 SEM-EDS analysis of doped matte samples

In this doped matte specimen, the arsenic location is analyzed, whether it is mixed in the copper matte solution as sulfides or stable as a separated metallic phase. Impurities and segregates in doped copper matte (DM1 and DM2) are similar to ones in normal matte (M1, M2, and M3), namely iron oxide (point 4 of table 12), Cu (point 7), and Pb (point 8). The presence of highly concentrated lead spots (97 wt-%) is new, whereas in normal copper matte, it is always grouped up with nickel. One more unique element, technetium (Tc), is found in some droplets, 6.45 wt-% (point 1), 35.95 wt-% (point 9), and 0.35 wt-% (point 6).

As shown in figure 35a, thin white lines are formed around the surface, which most likely are grain boundaries. The white dots are some metallic phases, including nickel and arsenic (point 1, 3, 6, 9 of table 12). Occasionally, the metallic phase could be precious metal, which is common in copper ore, such as silver (point 5). Circled gray area whose color is close to copper matte is zinc sulfide (point 2), which appears in sample M2 and M3. The gray matrix is copper matte (area A, B, & C). No arsenic trace is found in these areas.

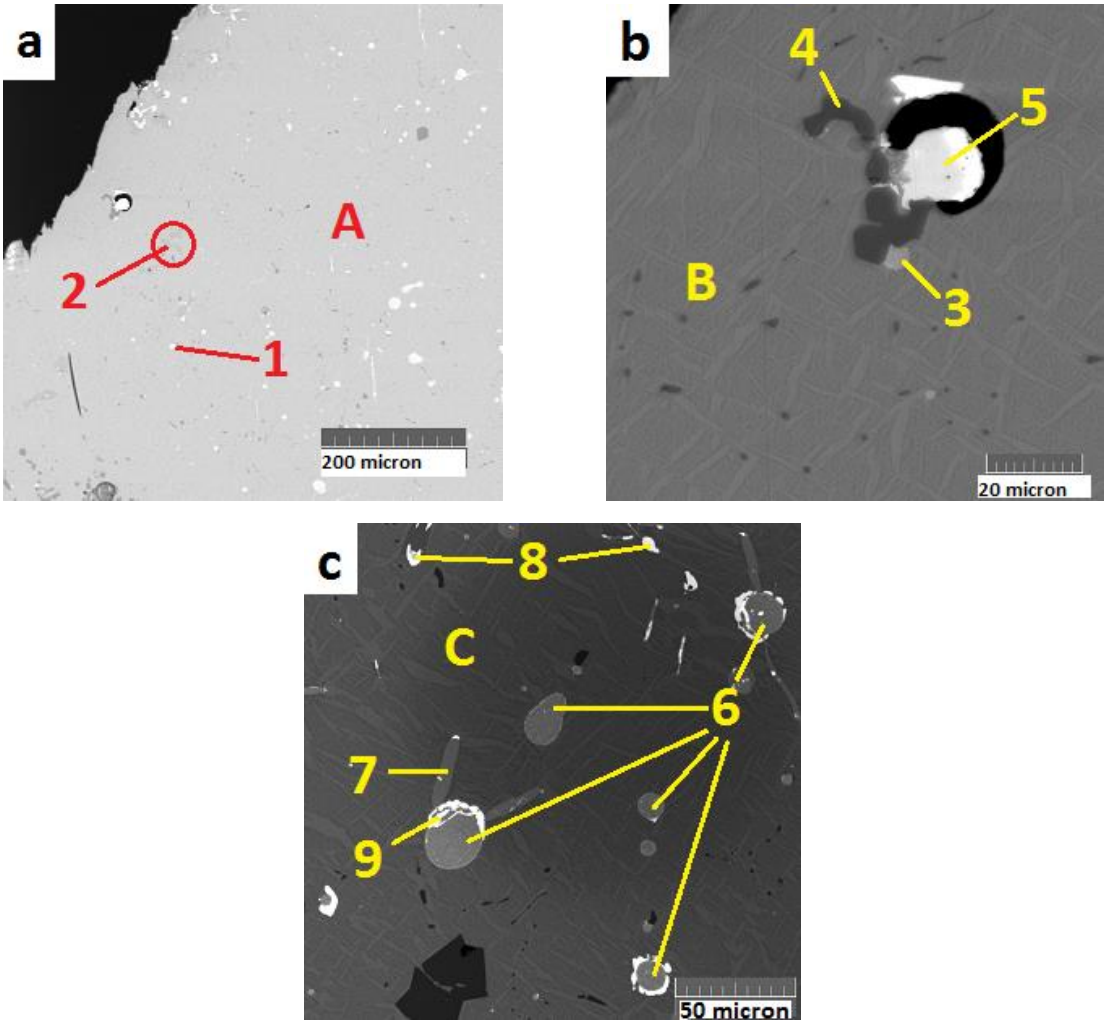

Figure 35 Sample DM1: (a) displaying macro appearance (407x); (b) zooming in edge part (2670x); and (c) zooming in middle part (1340x).

Table 12 EDS analysis of sample DM1 in wt-%

	O	Al	Si	S	Fe	Co	Ni	Cu	Zn	As	Tc	Sn	Ag	Sb	Ta	Pb	Phases
1	0.4	-	-	-	1.6	3.3	40.7	6.2	-	37.8	6.5	3.6	-	-	-	-	Ni-As
2	0.6	0.3	-	30.0	6.4	-	-	-	47.3	-	-	-	-	-	15.4	-	Zn-Ta-S
3	0.6	-	-	1.7	2.8	3.9	41.5	10.8	-	37.9	-	-	-	0.9	-	-	Ni-As-Cu
4	29.1	-	0.2	0.1	68.8	-	-	1.7	-	-	-	-	-	-	0.1	-	Fe-O
5	1.5	-	0.1	-	-	-	-	2.6	-	-	-	-	95.7	-	-	-	Ag
6	0.4	-	-	-	1.2	3.2	49.0	6.5	-	37.3	0.3	-	-	1.8	-	0.2	Ni-As
7	0.3	0.2	-	0.6	1.0	-	-	98.0	-	-	-	-	-	-	-	-	Cu
8	0.2	-	-	-	0.5	-	-	5.0	0.4	-	-	-	-	-	0.2	93.7	Pb
9	1.7	-	-	-	0.7	2.3	28.7	3.5	-	23.2	36.0	1.0	-	3.1	-	-	Tc-Ni-As
A	1.4	0.1	-	22.1	8.1	-	-	68.4	-	0.1	-	-	-	-	-	-	Cu-Fe-S
B	1.3	-	-	22.0	8.4	-	-	68.3	-	-	-	-	-	-	-	-	Cu-Fe-S
C	0.6	0.2	-	22.5	7.5	-	-	69.2	-	-	-	-	-	-	-	-	Cu-Fe-S

Some white droplets on the surface are segregated into bright and darker areas, as shown in figure 35c and 36. Table 12 (point 6) and 13(point 2 and 8) show that dark areas are primarily composed of metals with higher melting point and lighter density, e.g. nickel. Meanwhile, metals with lower melting point solidify later, thus stacked at the outer circle of droplets, as

shown in table 12 (point 9) and table 5 (point 3, 4, and 5). The later bright metal areas are primarily composed of lead, accompanied by less portion of arsenic and nickel.

Beside various melting points across the droplets, segregation is initiated by density difference. Lead belongs to heavy metal group, which makes it solidified at the outer circle of the droplets. This also explains why technetium is segregated at the outer circle. Meanwhile arsenic, having mid-range melting point and atomic mass, is found in both dark and bright droplets (Appendix C). Slow cooling process enables mass transfer through density difference.

Sample DM2 contains zinc-tantalum sulfide (point 1 of table 13), which is also found in DM1 and M3, and zinc iron sulfide (point 7). Iron oxide spots are also found here as in other samples (point 6). A minor area of pure copper is shown in figure 36b (point 9). Area A and B of table 5 prove that copper grade of DM2 fits the ICP analysis, between 66 and 68 wt-%.

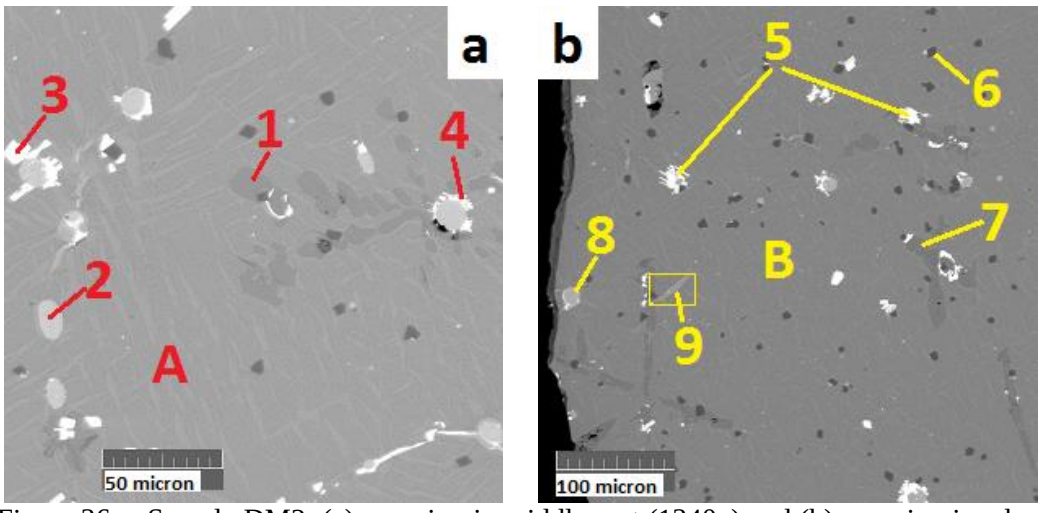

Figure 36 Sample DM2: (a) zooming in middle part (1340x) and (b) zooming in edge part (666x).

Table 13 EDS analysis of sample DM2 in wt-%

	O	Al	S	Fe	Co	Ni	Cu	Zn	As	Sb	Ta	Pb	Phases
1	-	-	27.7	6.1	-	-	-	41.0	-	-	25.2	-	Zn-Ta-S
2	0.3	-	-	1.1	0.9	57.0	5.2	-	30.3	3.0	-	2.2	Ni-As-Cu
3	1.1	0.1	-	0.5	-	21.5	3.8	-	-	-	-	73.0	Pb-Ni
4	1.4	0.1	12.5	1.6	-	21.4	14.6	-	-	-	-	48.4	Pb-Ni-Cu-S
5	1.1	0.2	-	0.3	-	25.4	2.4	-	0.2	-	-	70.4	Pb-Ni
6	28.3	0.1	0.2	68.8	-	-	1.9	-	-	-	0.7	-	Fe-O
7	0.1	-	25.2	5.2	-	-	-	33.7	-	-	35.8	-	Zn-Ta-S
8	-	-	2.0	1.3	0.9	51.1	14.3	-	27.0	2.0	-	1.5	Ni-As-Cu
9	0.4	0.2	-	1.0	-	-	98.1	-	-	-	-	-	Cu
A	1.2	0.1	22.0	8.5	-	-	68.2	-	-	-	-	-	Cu-Fe-S
B	1.0	0.1	22.2	7.7	-	-	68.9	-	-	-	-	-	Cu-Fe-S

10.1.3 SEM-EDS analysis of slag samples

Three slag samples have common traits about their microstructure (figure 37-39). First, they have less cracks and cavities compared to matte samples. Second, large crystals (gray area) are spread across the gray matrix. They are needle-shaped and have different orientation. Sample S1 has its crystals aligned at similar orientation in the middle, but random on its edge (figure 37a). Sample S3's crystals orientation is even more aligned in every part of it (figure 39a). Sample S2, on the other hand, has its crystal aligned randomly (figure 38a).

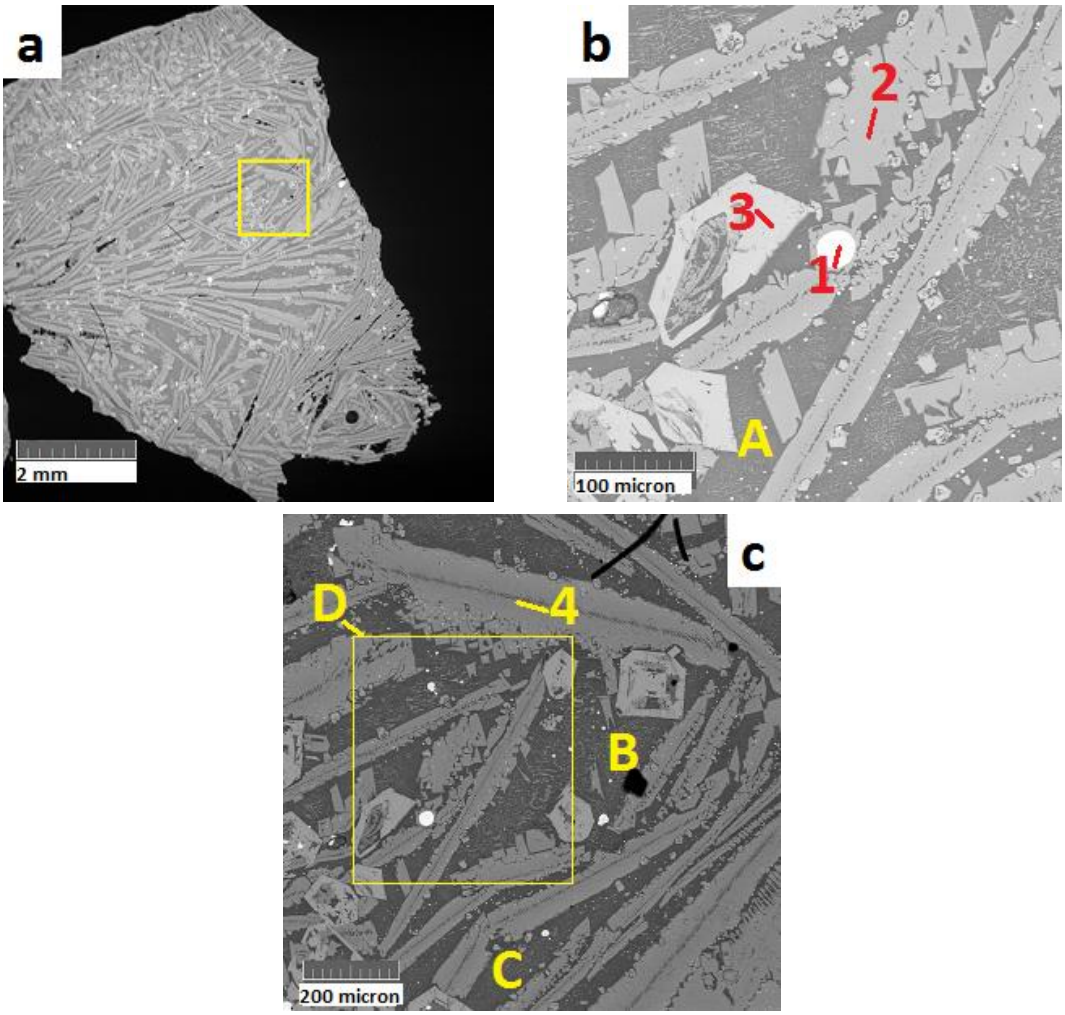

Figure 37 Sample S1: (a) displaying macro appearance (33x); (b) zooming in center part (666x); and (c) zooming in center part (267x).

There are four phases in sample S1, S2, S3: white/bright spots, light gray, gray, and dark gray area. The whiter the spot, the more metal it contains, like copper sulfide and arsenic in point 1 (table 14). The light-gray areas are composed of iron oxide and aluminium oxide (point 3). The gray needle crystals are composed of silicon and iron oxide, bring in the conclusion that this might be the fayalite phase (point 2 & 4). The matrix phase, dark gray area, is mainly silica

(area A, B, C). It variably contains aluminium oxide and iron oxide. Area D was scanned to confirm the representative phase of the corresponding slag, where conclusively, iron-silicate is the dominant one.

Table 14 EDS analysis of sample S1 in wt-%

	O	*Mg*	*Al*	*Si*	*S*	*K*	*Ca*	*Ti*	*Fe*	*Cu*	*Zn*	*Phases*
1	1.4	-	0.1	-	20.2	-	-	-	5.2	73.2	-	Cu-Fe-S
2	37.8	-	-	13.5	-	-	-	-	48.7	-	-	Fe-Si-O
3	32.5	-	4.4	0.2	-	-	-	0.7	62.3	-	-	Fe-O
4	38.3	2.7	0.6	14.1	-	0.2	0.2	-	44.0	-	-	Fe-Si-O
A	49.3	-	7.2	24.9	-	1.6	5.0	0.2	10.5	-	1.2	Si-Fe-Al-O
B	44.3	-	6.1	21.9	-	1.5	2.7	0.3	19.8	-	3.4	Si-Fe-Al-O
C	44.8	-	6.2	22.7	-	1.5	2.8	0.1	18.7	-	3.1	Si-Fe-Al-O
D	39.0	0.8	4.3	17.7	-	0.9	1.4	0.2	32.5	-	3.2	Fe-Si-O

In sample S2 (figure 38), some light-gray crystals contain only iron oxide (point 1 & 2 of table 15). This is similar to copper matte samples, where iron oxide droplets are scattered evenly across the surface. However, the line between each iron oxide could not be drawn because iron oxide in slag sample is localized, contradicting the scattered droplets. In certain locations, the dark-gray area contains a lot of mini gray dots (area B), causing concentration of iron oxide to be quite high. Point 3 signifies the fayalite crystal. Point 5, although contains similar elements to point 3, has different weight distribution. Tiny white droplets that are found across the whole surface, are copper sulfide phase (point 4). Bigger bright droplets (area A of figure 38b), which are found in many spots over the slag sample, are copper sulfide and arsenic phase.

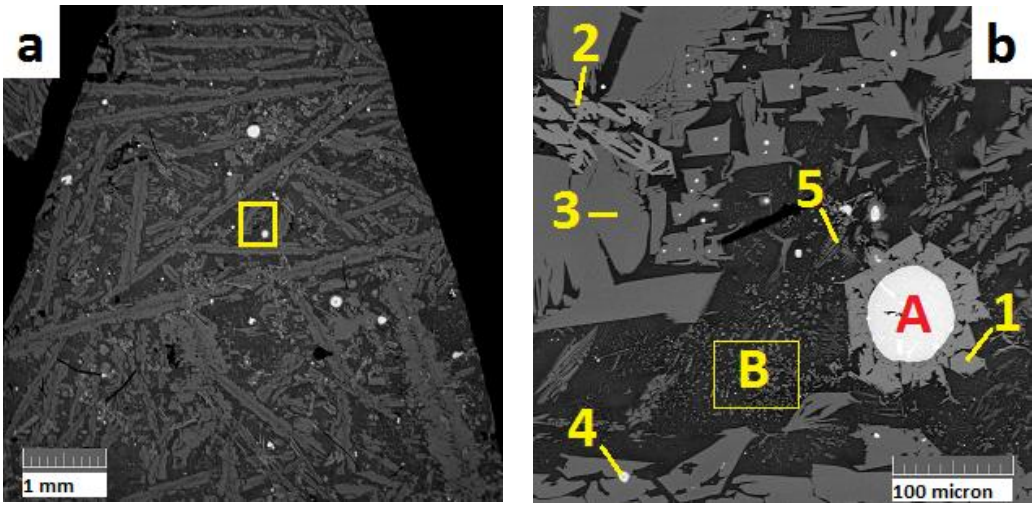

Figure 38 Sample S2: (a) displaying macro appearance (48x) and (b) zooming in center part (667x).

Table 15 EDS analysis of sample S2 in wt-%

	O	Mg	Al	Si	S	K	Ca	Fe	Cu	Zn	As	Sb	Ta	Pb	Phases
1	31.9	-	3.1	0.3	-	-	-	64.7	-	-	-	-	-	-	Fe-O
2	31.7	-	2.9	-	-	-	-	65.4	-	-	-	-	-	-	Fe-O
3	38.2	2.8	-	13.1	0.02	-	-	45.9	-	-	-	-	-	-	Fe-Si-O
4	3.8	-	-	-	18.2	-	-	4.9	73.2	-	-	-	-	-	Cu-S
5	42.2	-	3.6	19.5	-	1.6	1.8	23.1	-	3.4	-	-	5.0	-	Fe-Si-O
A	1.6	-	-	-	7.9	-	-	1.5	70.4	-	17.1	0.9	-	0.6	Cu-As-S
B	43.1	-	5.5	21.4	-	1.7	1.9	23.5	-	3.0	-	-	-	-	Si-Fe-Al-O

From figure 39, big droplets of copper sulfide and arsenic phase are found in sample S3 as well (point 1, 2, 6, and 7 of table 16). At this point, the droplet is obviously segregated into layers of copper sulfide and arsenic. Small droplets of copper sulfide (point 3 & 11 of table 16) are formed on the surface, in the same manner as sample S2 (point 4 of table 15). Iron oxide exists as fayalite crystals (point 4 & 9 of table 16) and iron oxide mixed with minor alumina and zinc oxide (point 5, 8, & 10 of table 16).

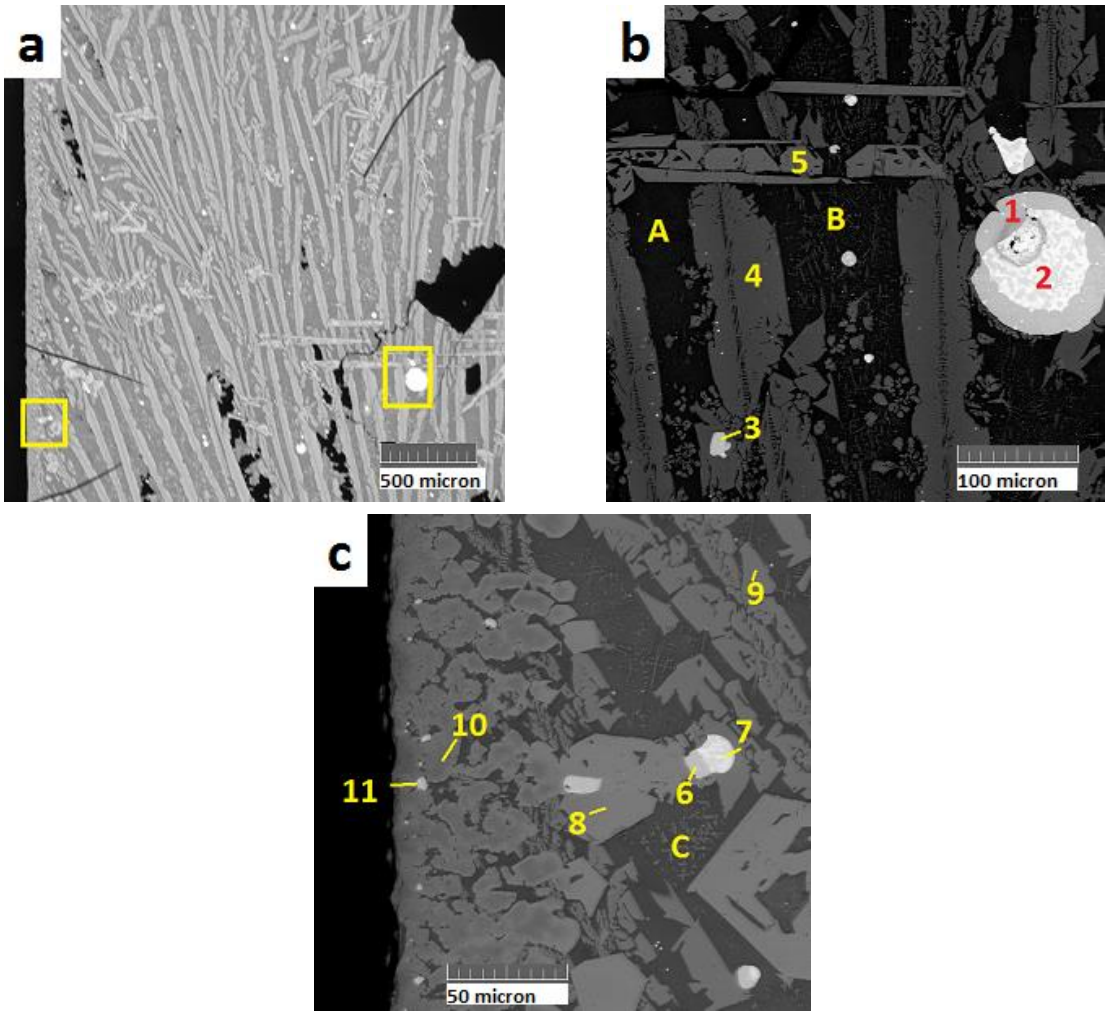

Figure 39 Sample S3: (a) displaying macro appearance (107x); (b) zooming in center part (669x); and (c) zooming in center part (1340x).

Area A, B, and C of table 16 show composition of dark gray glassy matrix. It primarily consists of silica. If the amount of iron is 17 wt-%, then the silicon in the fayalite phase equals to 8 wt-%, which leave the remaining 15 wt-% silicon as silica. Roughly estimating from the macro observation of three slag samples (figure 37a, 38a, and 39a), the portion of fayalite crystals is still higher than glassy silica matrix.

Table 16 EDS analysis of sample S3 in wt-%

	O	*Mg*	*Al*	*Si*	*S*	*K*	*Ca*	*Fe*	*Ni*	*Cu*	*Zn*	*As*	*Sb*	*Phases*
1	1.46	-	0.07	-	20.34	-	-	1.72	-	76.41	-	-	-	Cu-S
2	0.46	-	-	-	-	-	-	0.54	1.33	70.77	-	23.27	3.63	Cu-As
3	1.23	0.07	-	-	18.33	-	-	5.01	-	75.35	-	-	-	Cu-S
4	36.75	2.31	-	13.25	-	-	-	47.69	-	-	-	-	-	Fe-Si-O
5	32.71	-	4.73	0.32	-	-	-	61.87	0.37	-	-	-	-	Fe-O
6	1.27	-	-	-	18.93	-	-	2.66	-	77.14	-	-	-	Cu-S
7	0.57	-	-	-	-	-	-	2.47	4.05	74.62	-	14.87	3.43	Cu-As
8	33.08	-	5.67	-	-	-	-	60.83	0.41	-	-	-	-	Fe-Al-O
9	36.93	2.16	-	13.31	-	-	-	47.60	-	-	-	-	-	Fe-Si-O
10	36.38	1.14	19.10	-	-	-	-	35.08	0.49	-	7.81	-	-	Fe-Al-Zn-O
11	1.67	0.27	-	-	14.67	-	-	4.60	-	78.78	-	-	-	Cu-S
A	46.22	-	7.99	24.66	-	1.58	2.40	14.50	-	-	2.64	-	-	Si-Fe-Al-O
B	45.13	-	7.03	23.97	-	1.39	2.25	17.89	-	-	2.34	-	-	Si-Fe-Al-O
C	48.96	0.34	6.52	23.03	-	1.83	1.81	17.50	-	-	-	-	-	Si-Fe-Al-O

The copper grade of S1 and S2 are similar (73%), while S3 has a bit higher grade (75-78%), as shown in table 16. From microscope observation, different Fe-SiO_2 ratio between the three slag samples do not cause notable disparity in the microstructure. At this point, thermal conductivity of three slag samples might be different by a slight margin.

10.1.4 XCT analysis of three samples

Sample M3, DM1, and S1 were analyzed in XCT. The XCT results are shown in figure 40. In the normal copper matte sample (figure 40a), a lot of low density round areas are observed, which could be sulfur dioxide gas bubbles. This indicates that gas bubbles contribute to discontinuation in the normal copper matte matrix system. According to section 10.1.1, normal copper matte samples have a lot of micro cracks, which are found from figure 40a as well, whereas the macro cracks in the matte sample are formed during XCT sample preparation.

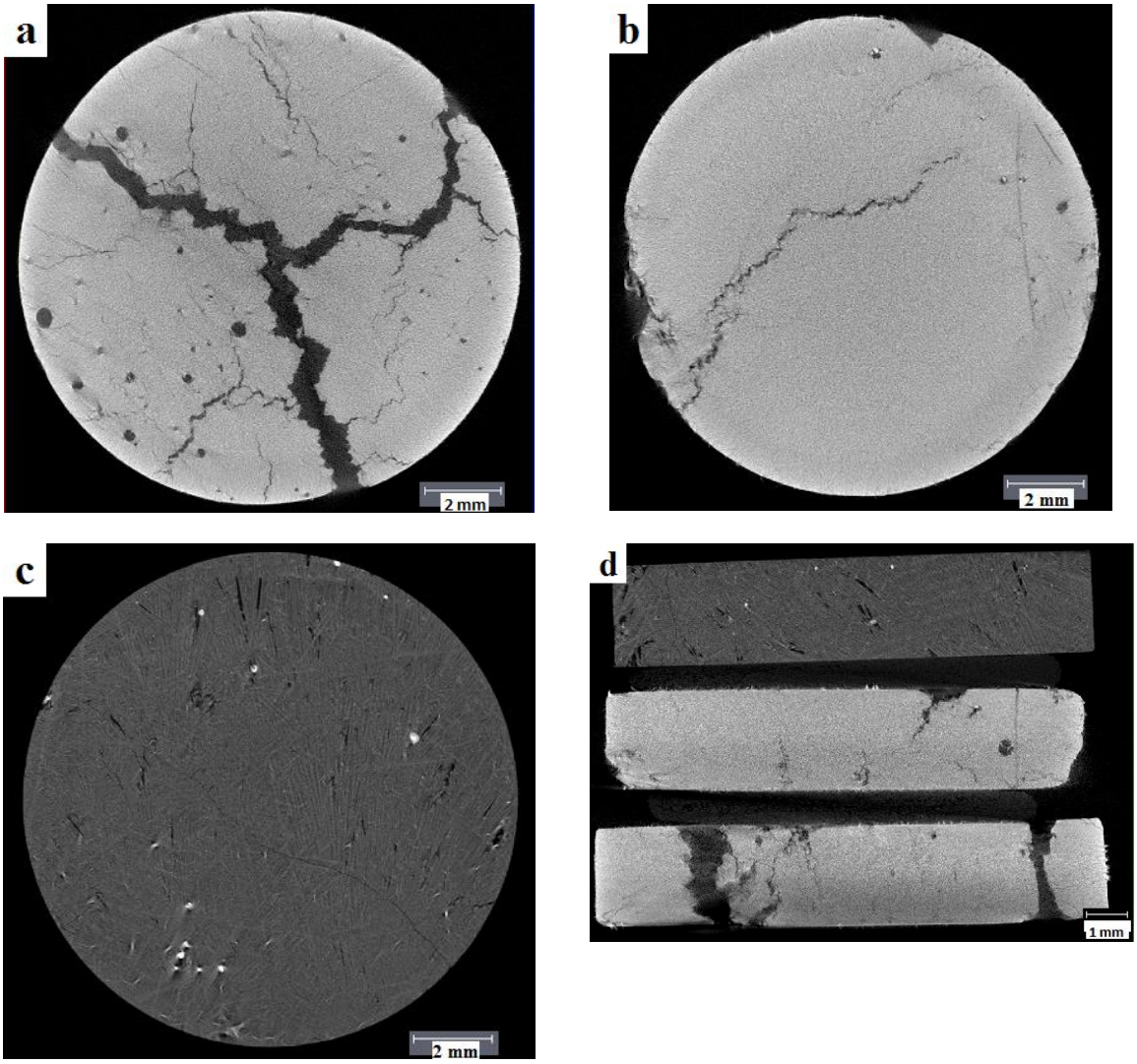

Figure 40 XCT analysis result of: (a) horizontal cross-section of sample M3; (b) horizontal cross-section of sample DM1; (c) horizontal cross-section of sample S1; and (d) vertical cross-section of sample S1, DM1, and M3 (top-down).

The doped matte sample, on the other hand, has much less bubbles and cracks (figure 40b) compared to normal matte sample. Both matte samples are quite homogeneous compared to slag sample (figure 40c). It has a soft long crack across the horizontal section. Many pores and copper sulfide inclusions are observed in the slag sample, which match the SEM analysis in section 10.1.3. These imperfections create discontinuation in the solid structure that diminish thermal conduction. The slag sample displays a vitreous or glassy structure. Lastly, figure 40d shows the vertical cross-section area of the three samples. All samples display similar vertical cross-section structure to the horizontal cross-section areas.

10.2 Thermal conductivity analysis

There are three important notes for analyzing experimental result in this thesis. First, thermophysical properties of studied copper matte are changing. This is concluded from the specific heat capacity comparison between pure Cu_2S and experimental data of this thesis. Figure 41a shows that pure Cu_2S has two positive specific heat capacity peaks due to crystal structure change at 390 and 750 K, with magnitude between 0.52 and 0.68 J g^{-1} K^{-1}. On the other hand, industrial copper matte (figure 41b) has only one peak at 157 °C, with a magnitude above 1.5 J g^{-1} K^{-1}.

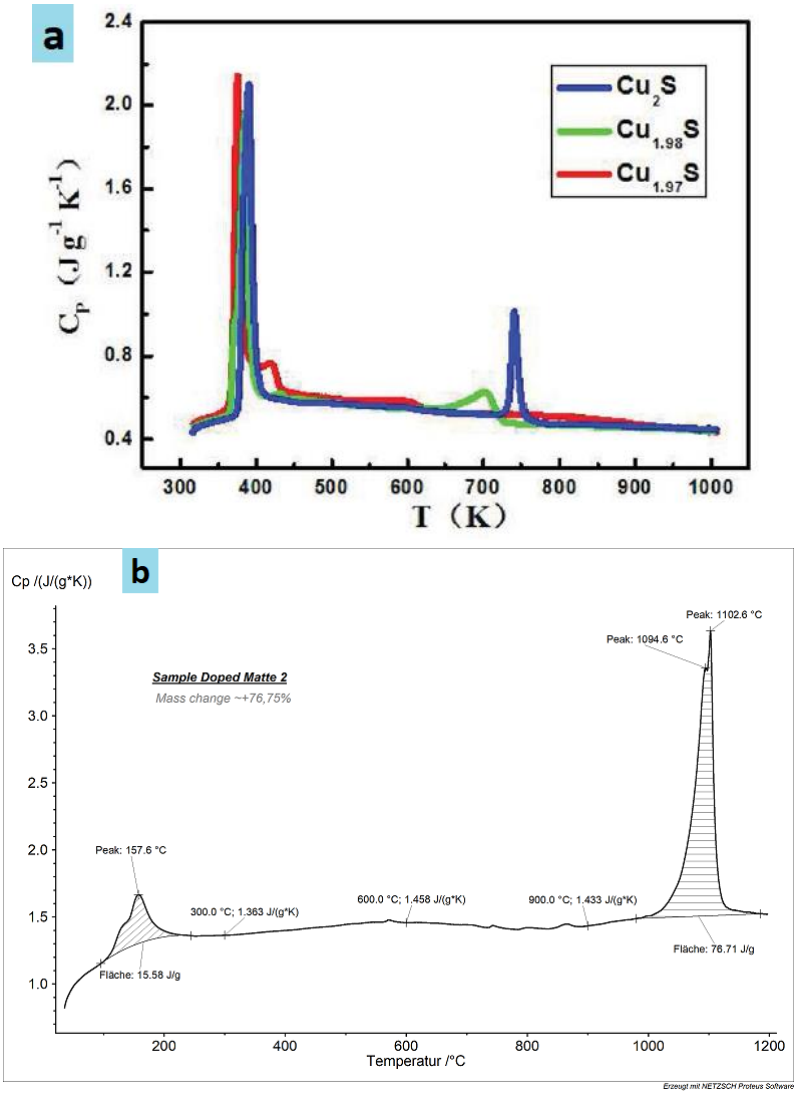

Figure 41 Chart of temperature-based specific heat capacity data of: (a) Cu_2S from a reference (He, Y. et al., 2016) and (b) of industrial copper matte sample M2.

Secondly, most data of thermophysical properties and electrical conductivity were measured in prior research at interval of 100 K, covering each crystal structure. Experimental results of this thesis, on the other hand, are plotted at three temperature points only. Interval of 100 K is

useful to observe the behavior of each crystal structure. After crystal structure change, sometimes conductivity shifts to a different level, thus conductivities of some sulfides fluctuate. At least, smaller interval would be beneficial for this thesis in two things: knowing the thermal conductivity level before crystal structure change at 157 °C and figuring out glass transition temperature of the slag samples.

Lastly, the measured specific heat capacity of M1 and M2 from the NETZSCH-Gerätebau GmbH Applications Laboratory are equal. The accuracy of thermal conductivity of M1 and M2 might be compromised a bit because specific heat capacity should be sensitive to composition.

10.2.1 Comparison of three normal matte samples

This comparison was made to analyze the effect of copper grade to thermal conductivity. Range of thermal conductivity of M1 and M2 is between 1.2 and 2.1 W m^{-1} K^{-1} (figure 42b). This range is at the same order of magnitude with copper sulfide in section 8.1, between 0.3 and 0.4 W m^{-1} K^{-1}. Observing relation between thermal conductivity and temperature, the experimental data follows thermal conductivity behavior of pure copper sulfide in two aspects.

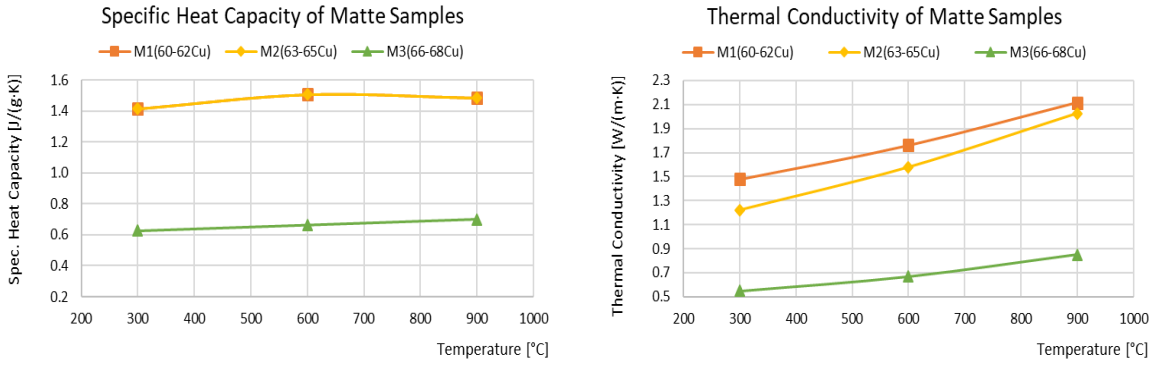

a b

Figure 42 Measured specific heat capacity (a) and thermal conductivity (b) of copper matte.

First, M1 has higher thermal conductivity than M2. It means lower copper sulfide concentration causes higher thermal conductivity. This is theoretically valid because copper sulfide has the lowest thermal conductivity compared to other sulfides, e.g. bornite and pyrite. Second, there is an increased level of thermal conductivity from 300 °C to 900 °C, which eliminates the possibility of copper matte being a conductor. These two facts indicate that industrial copper matte is either a semiconductor or a non-conductor.

Sample M3, on the other hand, has much lower specific heat capacity than M1 and M2, between 0.5 and 0.7 J g^{-1} K^{-1} (figure 42a). The only significant difference between them is presence of arsenic in M3 as observed in section 10.1.1. It is assumed to cause M3 to have lower thermal conductivity than M1 and M2. Hence, M3 is going to be compared with arsenic doped matte.

At 107 °C, copper sulfide stays as hexagonal chalcocite and changes to FCC chalcocite at 437 °C. FCC chalcocite is said to have the character of a metal, has high thermal conductivity at the beginning, which decreases as temperature goes higher. However, thermal conductivity of copper matte at 900 °C is higher compared to that at 600 °C for M1, M2, and M3, even though crystal structure change is not detected from specific heat graphic. This is characteristic to a typical non-conductor. There are two possible reasons why it is not a semi-conductor or conductor anymore: metal-insulator transitions or different crystal structure due to presence of FeS in the matrix.

Electrical conductivity behavior at elevated temperatures could be inferred from thermal conductivity behavior, referring to literature review at section 5.5. If thermal conductivity increases at elevated temperatures, resistivity by phonon would increases as well, thus electrical conductivity decreases with temperature. Although primarily contain copper sulfide, the absolute value of electrical conductivity of copper matte samples might be as low as that of non-conductor. Confirmation of actual value of electrical conductivity of copper matte requires another kind of experiment.

To this date, no reference of thermal conductivity of FeS was found. However, it is assumed that thermal conductivity of FeS is higher than Cu_2S because that of copper matte is higher than pure Cu_2S. Nevertheless, composition is not the only factor of thermal conductivity; crystal structure is an important factor as well. Therefore, thermal conductivity measurement of FeS are needed to ascertain the analysis.

10.2.2 Comparison of two doped matte samples and one normal matte sample

Two doped copper matte samples have similar copper grade to sample M2, 63 to 65 wt-%. Their thermal conductivity is between 0.5 and 1.3 W m^{-1} K^{-1} (figure 43b), which is close to sample M3. The observation, therefore, serves to relate arsenic concentration with thermal conductivity.

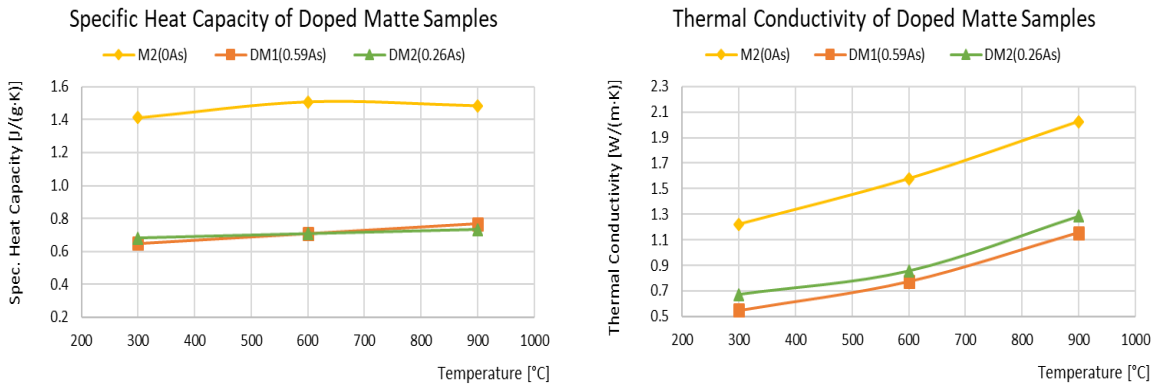

a b

Figure 43 Measured specific heat capacity (a) and thermal conductivity (b) of arsenic-doped copper matte.

DM1 has higher arsenic and copper grade than DM2, whereas M2 does not contain arsenic. According to the results of the experiment, higher copper grade seems to lead to lower thermal conductivity. Comparison of DM1, DM2, and M3 shows that thermal conductivity of arsenic-doped copper matte has a negative relation with both arsenic and copper grade. Range of thermal conductivity of the three arsenic-containing samples are: 0.5 – 1.2 W m^{-1} K^{-1} (DM1), 0.7 – 1.3 W m^{-1} K^{-1} (DM2), and 0.5 – 0.9 W m^{-1} K^{-1} (M3).

Reference for the effect of arsenic to thermal conductivity of sulfides is not found. In doping of single element semiconductors like silicon, arsenic is used as dopant to provide free electrons, which eventually increases electrical conductivity (Kittel, C., 1953). There is no reference that explicitly correlate the increased electrical conductivity to lowered electrical resistivity by phonon. However, because of lower thermal conductivity, electrical conductivity of arsenic-doped copper matte is inferred to be higher than that of normal copper matte.

10.2.3 Comparison of three slag samples

Thermal conductivity of three slag samples with different Fe - SiO_2 ratio are compared. Their values range between 1.7 and 1.9 W m^{-1} K^{-1} (figure 44c), which are close to values from prior research of silicate slag in section 8.6. Higher SiO_2 concentration makes the slag more glassy, while higher Fe concentration creates more fayalite crystals, which make slag structure to be less glassy. Figure 44c shows that all slag samples behave as glassy one.

Theoretically, higher Fe - SiO_2 ratio leads to less glassy structure, meaning lower thermal conductivity (Mills and Susa, 1992). Figure 44a and 44b show that thermal conductivity of S2

and S3 follow this principle and behave accordingly at the elevated temperatures, whereas S1 does not. Although its silica concentration is the highest, it has medium specific heat capacity and the lowest thermal diffusivity among the three slag samples. In addition, no significant difference between their microstructures is observed in section 10.1.3.

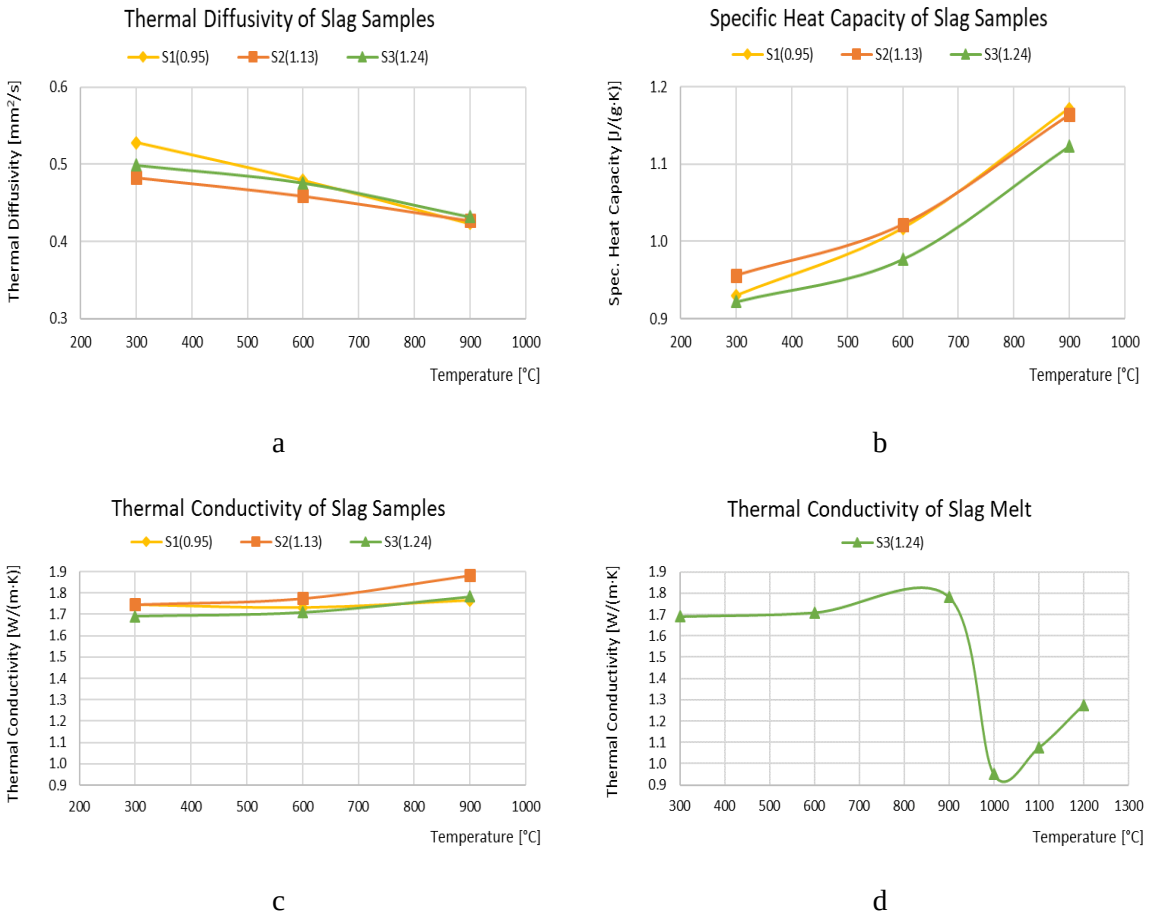

Figure 44 Thermophysical properties of the slag samples: (a) thermal diffusivity, (b) specific heat, (c) thermal conductivity of solid phase, and (d) thermal conductivity of molten slag

Moreover, thermal conductivity data of S3 melt (figure 44d) does not agree with prior research in section 8.6. It is supposed to decrease with temperature not only after glass transition (Mills and Susa, 1992), but also after melting point (Kang, Y. et al., 2014). Meanwhile, thermal conductivity of the studied slag sample increases with temperature after melting at 1000 °C.

According to section 8.6, the electrical conductivity would continue to increase after samples pass glass transition temperature. No research has measured electrical conductivity of any slag at below glass transition temperature, therefore electrical conductivity is assumed to be opposite of thermal conductivity. Glass transition temperature of the samples are unable to be determined unless more thermal conductivity data are collected between 700 and 900 °C.

11 Summary, conclusions, and suggestions

This section contains a summary of what was studied in this master's thesis. The conclusions of the obtained results and the suggestions for the future work on this research topic are presented.

The objective of this thesis to measure thermal conductivity of copper mattes and fayalite slags as a function of temperature, as well as investigating its relation to several factors, including electrical conductivity and composition. Prior publications in the field of thermal conductivity of sulfides were then reviewed to find the factors that influence them. Furthermore, they could be used as a comparison for the experimental results.

In order to fulfill the objectives, eight samples for thermal conductivity measurements were prepared as follows: three industrial copper matte samples, two arsenic-doped copper matte samples, and three fayalite slag samples. Thermal conductivity measurement results of normal copper matte samples could show the relation between matte copper grade and thermal conductivity. Arsenic-doped copper mattes measurement could show the effect of arsenic concentration to thermal conductivity of copper matte. Lastly, slags measurement could show the effect of Fe-SiO_2 ratio to thermal conductivity.

Microstructure is another important factor that could affect thermal conductivity of a material. Therefore, SEM analysis was applied in this study to observe whether there were significant differences of microstructure between the samples. It showed that all the samples were heterogeneous and slag samples were the most heterogeneous ones, followed by normal copper mattes and doped coper mattes. In addition, it was discovered from SEM analysis that one of normal copper mattes contains arsenic. From this fact, it was assumed that thermal conductivity of the arsenic containing copper matte would be similar to thermal conductivity of doped copper mattes.

After SEM analysis, all samples were subjected to thermal conductivity measurement by using laser flash analysis, which are measured at three temperature points: 300, 600, and 900 °C. The measured thermal conductivity of normal copper matte samples were 1.2 to 2.1 W m^{-1} K^{-1}. Meanwhile, arsenic containing matte samples exhibited low thermal conductivity, between 0.5 and 1.3 W m^{-1} K^{-1}. It was confirmed that arsenic containing normal matte and doped matte samples have similar thermal conductivity range.

Measured thermal conductivities of fayalite slag samples were between 1.6 and 1.9 W m^{-1} K^{-1}, close to results of prior research in silicate slags. All slag samples had more than 30 wt-% SiO_2 content and they behaved as glassy slag. Experimental data of the three slag samples were not conclusive as one of them had lower thermal conductivity than expected (sample S1). Sample S1 should have the highest thermal conductivity among all slag samples. In addition, one of slag samples was measured at 1000 to 1200 °C for observation of thermal conductivity of molten slag and its relation with temperature. The result was between 0.9 and 1.3 W m^{-1} K^{-1}.

The experimental data showed that thermal conductivity of copper mattes increases linearly with temperature. The low values of thermal conductivity were within expectation as copper sulfide has the lowest thermal conductivity among the sulfides according to prior research. Positive relation between thermal conductivities of mattes and temperature, however, was outside expectation because it marked the behavior of non-conductors. The adverse effect of arsenic to thermal conductivity of mattes was another important finding as well. From the slag samples analysis, thermal conductivity behavior of solid fayalite slags followed that of silicate slags in prior publications, while the molten slag sample did not. The discussed analysis in section 10 is summarized into eight points as follows:

1. Industrial copper matte possess thermophysical characteristics of a non-conductor, so its thermal conductivity increases with temperature;
2. Thermal conductivities of the studied copper mattes have a weak dependency on temperature, which are between 1.2 and 2.2 W m^{-1} K^{-1} at 300 to 900 °C;
3. Thermal conductivity of FeS is assumed to be higher than Cu_2S, therefore higher copper grade leads to higher copper sulfide content, which results in lower thermal conductivity;
4. Electrical conductivity of copper matte is assumed to behave like semiconductor, where electrical conductivity is in negative relation with thermal conductivity; the basis of this assumption is electrical conductivities of slags that behave similarly in prior research;
5. Higher arsenic concentration decreases phonon activity, which eventually decreases thermal conductivity; therefore it is assumed that electrical conductivity of arsenic-doped copper matte is higher than normal copper matte due to lowered phonon activity;
6. Thermal conductivity of fayalite slag is between 1.7 and 1.9 W m^{-1} K^{-1} at 300 to 900 °C, where it has the characteristics of glassy slag;
7. Higher Fe-SiO_2 ratio in fayalite slag leads to less glassy structure, which decreases thermal conductivity, while thermal conductivity of S1 deviates from this principle;

8. Measured thermal conductivity of molten slag deviates from the prior research of silicate slag that thermal conductivity should decrease with increasing temperature.

After getting through all measurements, three samples that represent each type of samples were subjected to an internal microstructure analysis by using x-ray computed tomography. This step was to make sure that significant differences do not exist between inside of each sample and its surface, which was validated by the results. In addition, there are suggestions for further analysis:

1. Thermal conductivity data for all matte and slag samples at molten phase would be valuable for designing more optimal cooling and lining system;
2. Thermal conductivity data below 300 °C could confirm whether copper matte is a non-conductor from the start or not;
3. Thermal conductivity experiment of FeS as a function of temperature could be helpful in confirming the measured thermal conductivity of all matte samples.

References

Bale, C.W.; Bélisle, E.; Chartrand, P.; Decterov, S.A.; Eriksson, G.; Gheribi, A.E.; Hack, K.; Jung, I.H.; Kang, Y.B.; Melançon, J., et al. Factsage thermochemical software and databases, 2010–2016. Calphad 2016, 54, 35–53.

Balow, Robert B. et al. 2015. Synthesis and Characterization of Copper Arsenic Sulfide Nanocrystals from Earth Abundant Elements for Solar Energy Conversion. Chem. Mater, 27, 2290-2293. DOI: 10.1021/acs.chemmaster.5b00701

Bekenstein, Y. 2014. Thermal doping by vacancy formation in copper sulfide nanocrystal arrays. Nano Lett. 2014, 14, pp. 1349-1353.

Bogaard, R.H., Ho, C.Y. 1989. Thermal Conductivity of Gallium Arsenide at High Temperature. In: Hasselman D.P.H., Thomas J.R. (eds) Thermal Conductivity 20. Springer, Boston, MA

Butera, R. A. and Waldeck, D. H. 1997. The dependence of resistance on temperature for metals, semiconductors, and superconductors. J. Chem. Education, Vol. 74, No. 9, pp. 1090-1094.

Chakrabarti, D. J. and Laughlin, D. E. 1983. The Cu-S (copper-sulfur) system. J. Phase Equilibria. DOI: 10.1007/BF02868665

Callister, William D. 2001. Fundamentals of Materials Science and Engineering: An Interactive, ch. 5 & 6. New York: John Wiley & Sons.

Coey, J. Roux-Buisson, H. Brusetti, R. METAL-NON METAL TRANSITIONS IN TRANSITION METAL COMPOUNDS.THE ELECTRONIC PHASE TRANSITIONS IN FeS AND NiS. Journal de Physique Colloques, 1976, 37 (C4), pp.C4-1-C4-10. <10.1051/jphyscol:1976401>. <jpa-00216515>

Dong, Y. et al. 2014. Effective Thermal Conductivity of Slag Crust for ESR slag. ISIJ International, vol. 55 (2015), No. 4, pp. 904-906.

Duan, J. et al., 2018. Multiple phase transitions and structural oscillations in thermoelectric Cu2S at elevating temperatures. Ceramics International 44, pp. 13076-13081.

Ejima, T. Watanabe, Y. Kameda, M. 1968. Electric conductance in molten lead silicates. II. Electric conductance in the molten PbO-SiO2-MO ternary system. Nippon Kinzoku Gakkaishi, vol. 32, pp. 1256-1262.

Fei, Y., Prewitt, C.T., Mao, H-K., Bertka, C.M. 1995. Structure and density of FeS at high pressure and high temperature and the internal structure of Mars. Science 268, pp.1892-1894.

Flemings, M. C. 2006. Solidification Processing. In Materials Science and Technology (eds R. W. Cahn, P. Haasen and E. J. Kramer). doi:10.1002/9783527603978.mst0173

Garbee, A. K. 1969. *ELECTROCHEMICAL PROPERTIES OF METAL SULFIDES IN IONIC MELTS*. The National Library of Canada.

Grønvold, F. and Westrum Jr., E. F. 1987. Thermodynamics of copper sulfides I. Heat capacity and thermodynamic properties of copper (I) sulfide, Cu_2S, from 5 to 950 K. J. Chem. Thermodynamics 1987, 19, pp. 1183-1198.

Grønvold, F. and Westrum Jr., E. F. 1976. Heat capacities of iron disulfide - Thermodynamics of marcasite from 5 to 700 K, pyrite from 300 to 780 K, and the transformation of marcasite to pyrite. J. Chem. Thermodynamics 1976, 8, pp. 1039-1048.

Grønvold, F. and Westrum Jr., E. F. 1958. Heat capacities and Thermodynamics properties of the pyrrhotite FeS and $Fe_{0.877}S$ from 5 to 350 K. J. Chem. Physics 1959, 30, 2, pp. 528-531.

Haynes, W. M. (2009). *CRC handbook of chemistry and physics: A ready-reference book of chemical and physical data*. Boca Raton: CRC Press.

Heimo, J. et al. 2018. Thermal Conductivity of Titanium Slags (master's thesis). Aalto University, Espoo, Finland.

He, Y. et al. 2014. High Thermoelectric Performance in Non-Toxic Earth-Abundant Copper Sulfide. Adv. Mater. 2014, 26, pp. 3974-3978.

Hirahara, E. 1950. The Physical Properties of Cuprous Sulfides Semiconductors. Journal of The Physical Society of Japan Vol. 6, No. 6.

Horvat, A., Rejec, T., Mravlje, J. 2013. Metal-Mott Insulator Transitions, Seminar. Ljubljana: University of Ljubljana, faculty of mathematics and physics.

Hoster, T. and Pötschke, J. 1983. Archiv Eisenhüttenwesen, 54, 389.

Howard, Stanley M. 2006. Standard Gibb's Energies of Formation for Bromides, Chlorides, Fluorides, Hydrides, Iodides, Nitrides, Oxides, Sulfides, Selenides, Tellurides. SD School of Mines and Technology.

Incropera, F. P., & DeWitt, D. P. (2002). *Fundamentals of heat and mass transfer, ch. 1-2*. New York: J. Wiley, 6th Ed.

Jansson, J., Pesonen, L., and Vajamo, I. 2015. Ensuring The Furnace Integrity with Intelligent Operations, Efficient Cooling, Refined Design. Outotec, The Conference of Metallurgists.

Jiang, C. and Song, J. 2014. *Significant photoelectric property change caused by additional nano-confinement: a study of half-dimensional nanomaterials.* Wiley: Small Vol. 10, No. 24, p.5044.

Kang, Y., Lee, J., and Morita, K. 2014. Thermal conductivity of molten slags: a review of measurement techniques and discussion based on microstructural analysis. ISIJ International, Vol. 54, No. 9, pp. 2008-2016.

Kato, K. et al. 1997. The thermoelectric properties of FeS_2. J. Materials Science Letters 16, pp. 914-916.

Kittel, C. 1953. *Introduction to solid state physics, chapter 1-8*. New York: Wiley.

Kyllo, A. K., Gray, N. B., Papazoglou, D., and Elliot, B. J. 2000. Developing composite furnace module cooling systems. JOM.

Leino, T. 2017. Determination of Metallization Degree of Prereduced Chromite with Image and Rietveld Analysis (master's thesis). Aalto University, Espoo, Finland.

Li, Fan. 1996. Studies of structures and phase transitions in pyrrhotite. *Retrospective Theses and Dissertations*. 11548. https://lib.dr.iastate.edu/rtd/11548

Lide, D. R. 2005. ed., *CRC Handbook of Chemistry and Physics, Internet Version 2005,* http://www.hbcpnetbase.com. CRC Press, Boca Raton, FL.

Liu, Y., Liu, M., and Swihart, M. T. 2017. Plasmonic Copper Sulfide-Based Materials: A Brief Introduction to Their Synthesis, Doping, Alloying, and Applications. J. Phys. Chem. C, 121, 13435-13447. DOI: 10.1021/acs.jpcc.7b00894

Madelung O., Rössler U., Schulz M. (eds) II-VI and I-VII Compounds; Semimagnetic Compounds. 1982. Landolt-Börnstein - Group III Condensed Matter (Numerical Data and Functional Relationships in Science and Technology), vol 41B. Springer, Berlin, Heidelberg.

Marinage, J. C. 1954. Some Electrical Properties of Natural Crystal of Iron Pyrite. Physical Review vol. 96, No. 3.

Mills, K. C. and Susa, M. 1992. Thermal conductivities of slags. NPL Report DMM(A) Vol. 68, National Physical Laboratory, London.

Mills, K. C., Yuan, L., and Jones, R. T. 2011. Estimating the physical properties of slags. Journal of Southern African Institute of Mining and Metallurgy, Vol. 111, pp. 649-658.

Nishioka, K., Maeda, T., and Shimizu, M. 2006. Application of square-wave pulse heat method to thermal properties measurement of CaO-SiO2-Al2O3 system fluxes. ISIJ International, vol. 46, pp. 427-433.

Ogonowski, S. et al. 2018. Comparison of Wet and Dry Grinding in Electromagnetic Mill. Minerals, 8, 138. doi: 10.3390/min8040138

Parker, W. J., Jenkins, R. J., Butler, C. P., and Abbott, G. L. 1961. *Flash method of determining thermal diffusivity, heat capacity, and thermal conductivity*. J. Applied Physics, Vol. 32, 9, pp. 1679-1684.

Pearce, I. C., Pattrick, R. A. D., Vaughan, D. J. 2006. Electrical and Magnetic Properties of Sulfides. Rev. Mineralogy & Geochemistry, Vol. 61, pp. 127-180.

Predel B. () Fe-S (Iron-Sulfur). In: Madelung O. (eds) Dy-Er – Fr-Mo. Landolt-Börnstein - Group IV Physical Chemistry (Numerical Data and Functional Relationships in Science and Technology), vol 5e. Springer, Berlin, Heidelberg. DOI: 10.1007/10474837_1136

Qiu, P. et al. 2016. Electrical and thermal transports of binary copper sulfides Cu_XS with X from 1.8 to 1.96. APL Materials 4, 104805; doi: 10.1063/1.4953439

Qiu, P. et al. 2014. Sulfide bornite thermoelectric material: a natural mineral with ultralow thermal conductivity. Energy Environ. Sci., 2014, 7, 4000.

Roine, A. HSC chemistry 9.2.6. Outotec Research Oy, Pori, Finland, 2018. Available online: http://www.chemistry-software.com/

Schlesinger, M. E., King, M. J., Sole, K. C., and Davenport, W. G. 2011. *Extractive metallurgy of copper, ch. 1, 5, and 6*. Amsterdam ; Boston: Elsevier.

Seetharaman, S. 2014. *Treatise on Process Metallurgy: Vol. 3, Industrial Processes*. Oxford: Elsevier.

Shinzato, K. and Baba, T. 2001. *A laser flash apparatus for thermal diffusivity and specific heat capacity measurements.* Journal of Thermal Analysis and Calorimetry, Vol 64, pp. 413-422.

Sun, C. and Guo, X. 2010. Electrical conductivity of MO (MO=FeO, NiO)-containing CaO-MgO-SiO_2-Al_2O_3 slag with low basicity. Transactions of Nonferrous Met. Soc. China 21, pp. 1648-1654.

Tsatis, D. and Theodossiou, A. 1981. Thermal Diffusivity in Pyrrhotite (Fe_7S_8). J. Phys. Chem. of Solids, vol. 43, 8, 1982, pp. 771-772

Vasuhi, A. et al. 2016. Tuning the structural properties and flower-like morphologies of Cu2S thin films through Zn doping. International Journal of Information Research and Review Vol.03, 5, pp. 2337-2342.

Wang, L. 2009. Estimations of Electrical Conductivities in Molten Slag Systems. Steel research int. 80, No. 9, pp. 680-685.

Wuensch, B. J. and Buerger, M. J. 1963. The crystal structure of chalcocite, Cu_2S. Mineralogical Society of America, special paper 1, pp. 164-170.

Yuan, Q. et al. 2017. The Effect of P on the Microstructure and Melting Temperature of Fe2SiO4 in Silicon Containing Steels Investigated by In Situ Observation. Metals, 7, 37.

Zhang, G.H. and Chou, K.C. 2010. Simple method for estimating the electrical conductivity of oxide melts with optical basicity. *Metallurgical and Materials Transactions B*, vol. 41, no. 1. pp. 131–136.

https://www.outotec.com/products/smelting-and-converting/cooling-elements/ [accessed October 29th 2018]

https://www.netzsch-thermal-analysis.com/en/products-solutions/thermal-diffusivity-conductivity/ [accessed: May 3rd 2018]

https://energyeducation.ca/encyclopedia/valence_band [accessed: November 13th 2018]

https://www.scienceabc.com/innovation/what-are-semiconductors-and-how-do-they-work.html [accessed: November 14th 2018]

Appendices

Appendix A

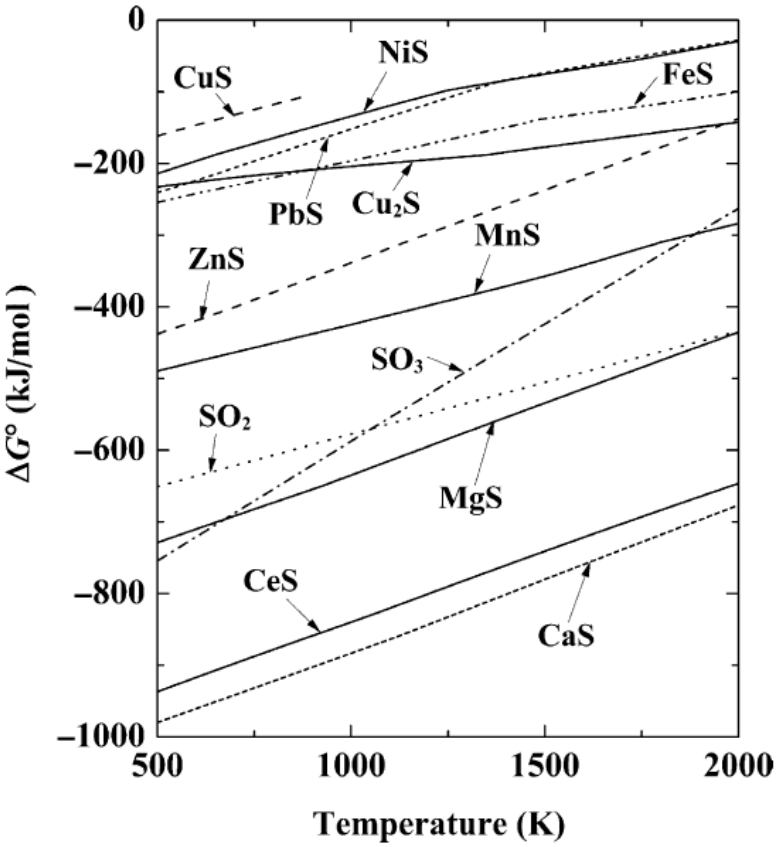

Figure 45 Ellingham diagram for sulfides per ½ S_2 (Seetharaman, S., 2014). Above 1000 K, Cu_2S has a bit more negative Gibb's free energy than FeS.

Table 17 Gibb's free energy of primary reactions in copper smelting furnace (Roine, A., 2018)

Reaction	ΔG (100°C) [kJ]	ΔG (1200°C) [kJ]
$Cu_2S + 1.5O_2(g) = Cu_2O + SO_2(g)$	-352.92	-228.27
$FeS + 1.5O_2(g) = FeO + SO_2(g)$	-437.72	-341.35
$NiS + 1.5O_2(g) = NiO + SO_2(g)$	-414.66	-317.76
$ZnS + 1.5O_2(g) = ZnO + SO_2(g)$	-414.03	-328.12
$PbS + 1.5O_2(g) = PbO + SO_2(g)$	-383.80	-296.59

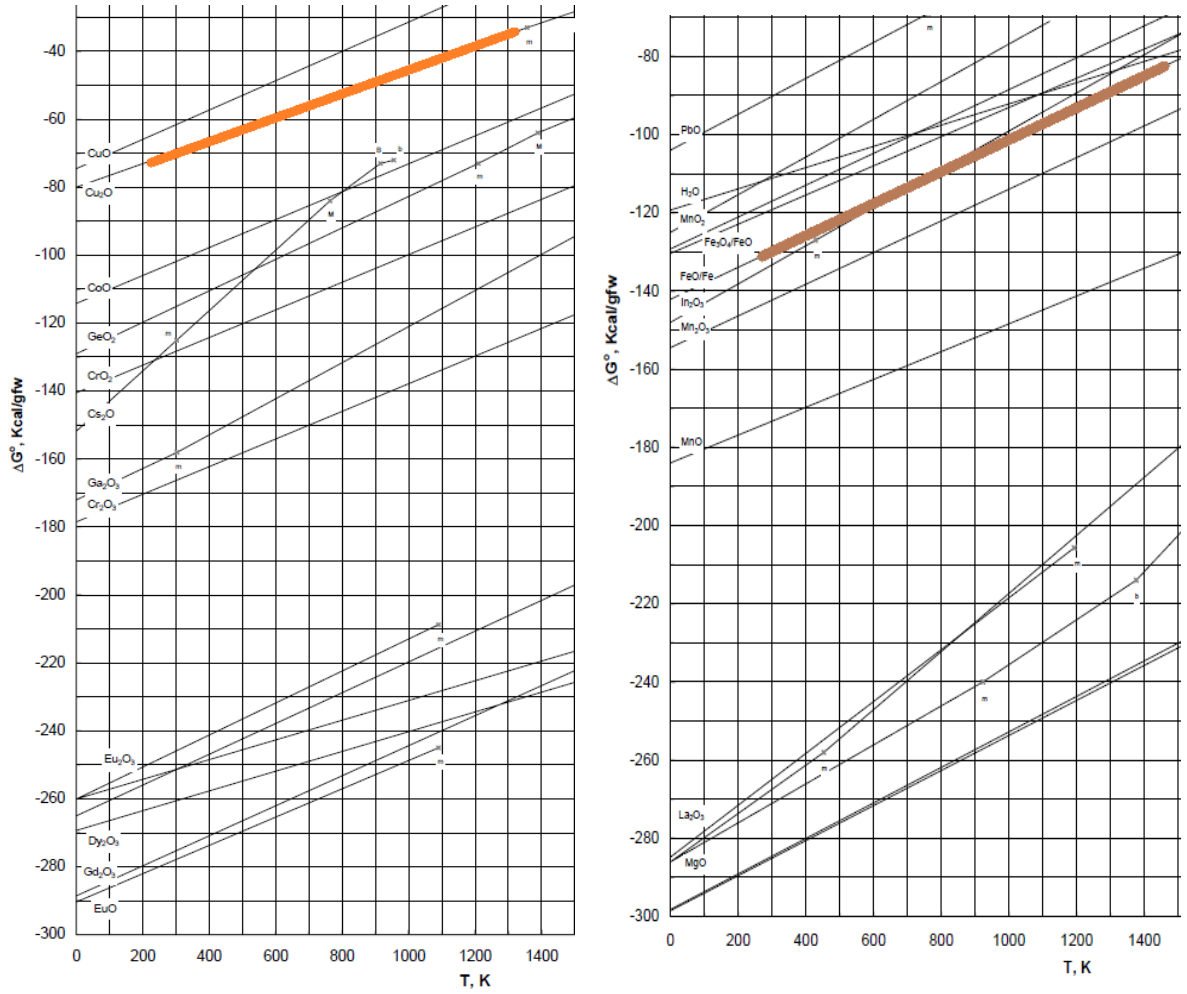

Figure 46 Ellingham diagram for oxides (Stanley M. Howard, 2006). The gfw unit at y-axis stands for gram formula weight, equals to mol. The pictures were cut from the original version to fit into the page. Orange line is Cu_2O (left-hand side) and brown line is Fe/FeO (right-hand side).

Appendix B

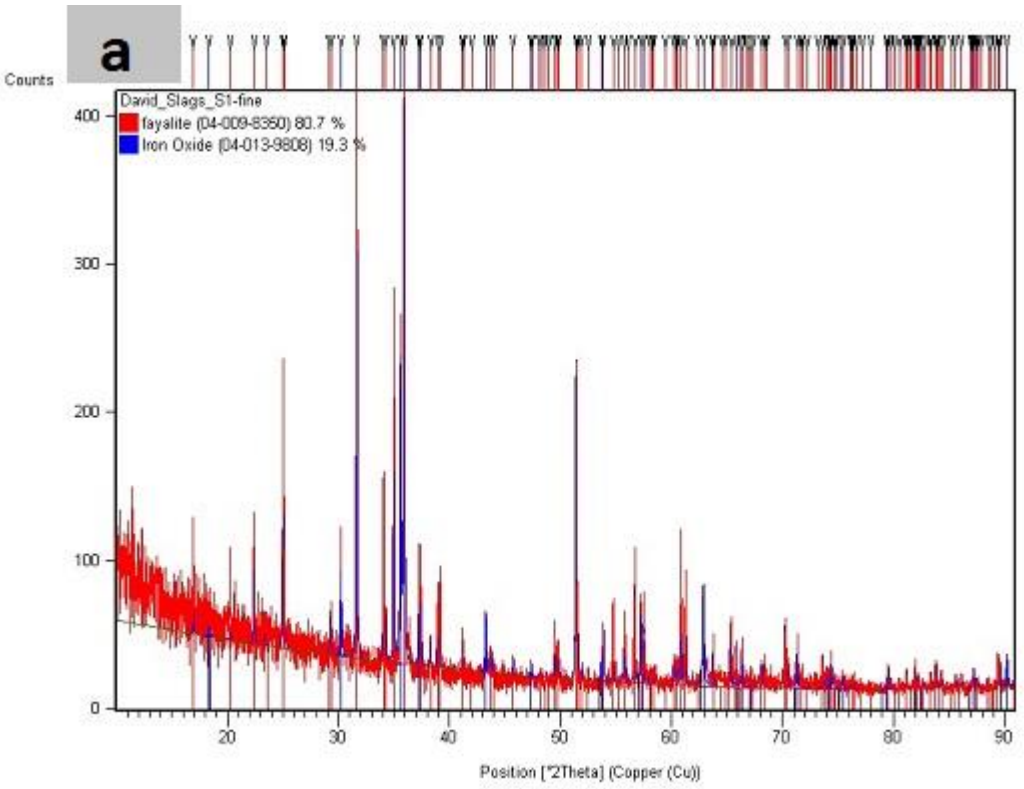
a
Counts
David_Slags_S1-fine
fayalite (04-009-8360) 80.7 %
Iron Oxide (04-013-9808) 19.3 %
400
300
200
100
0
20
30
40
50
60
70
80
90
Position [°2Theta] (Copper (Cu))

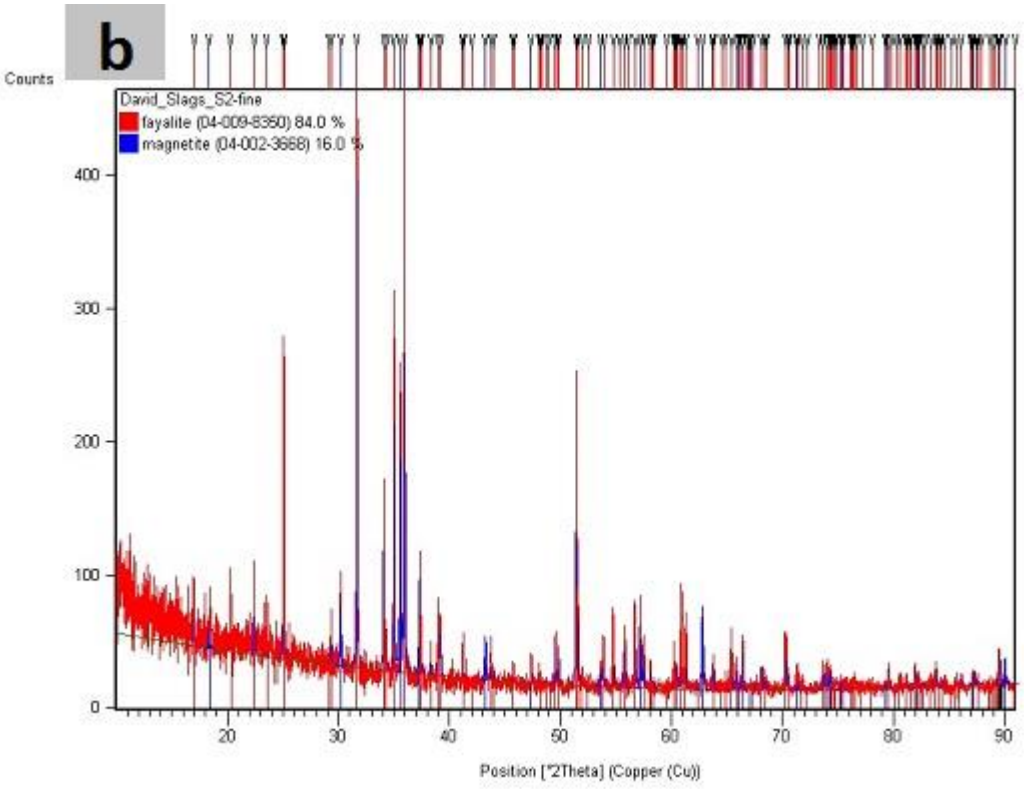
b
Counts
David_Slags_S2-fine
fayalite (04-009-8360) 84.0 %
magnetite (04-002-3668) 16.0 %
400
300
200
100
0
20
30
40
50
60
70
80
90
Position [°2Theta] (Copper (Cu))

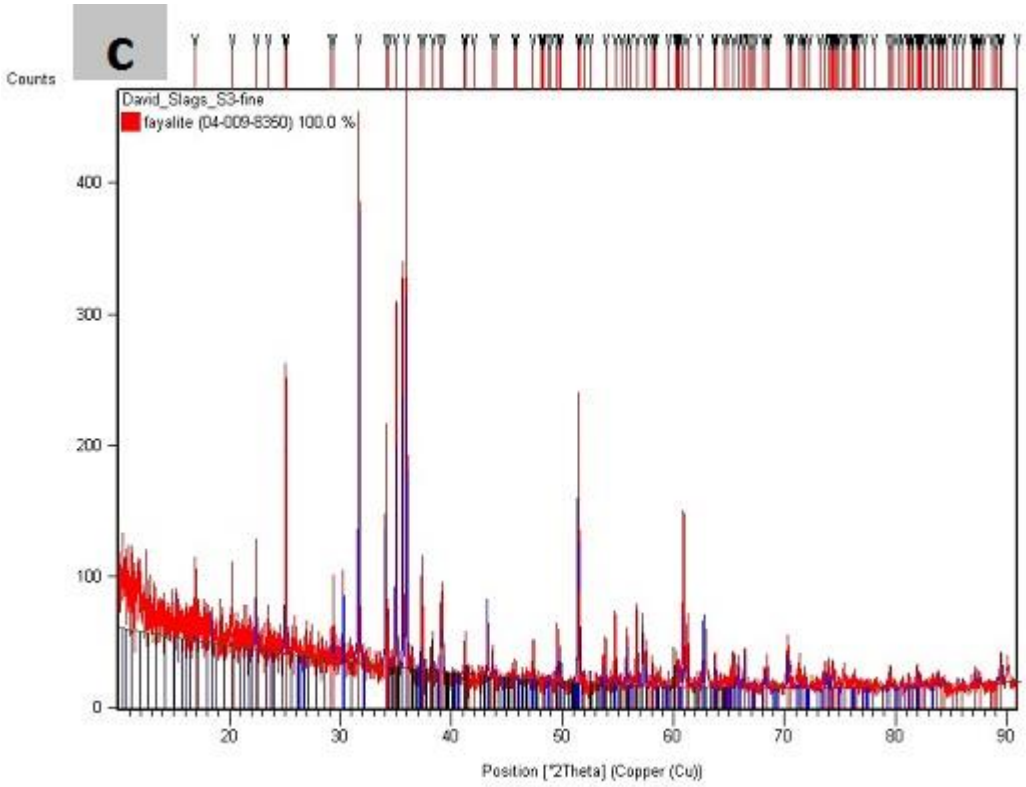

Figure 47 XRD analysis on 3 slag samples: (a) slag S1, (b) slag S2, and (c) slag S3. Only fayalite and magnetite were scanned here, although chosen fitting background during Rietveld analysis comprises fayalite, magnetite, silica, and alumina.

Accurate XRD analysis requires its powder sample to be as small as possible and homogeneous (Leino, T., 2017). In order to achieve that profile of particle size, wet grinding is a better option in XRD sample preparation. In addition, since all three samples contain sulfidic minor impurities, wet grinding is even more proper to be applied in this experiment (Ogonowski, S. et al., 2018).

Appendix C

Segregation is a gradient of concentration across the grain. In the area of particular grain, the metals are polarized, not mixed or fully soluble. Sequence of segregation formation is illustrated in the following figure 48. The system is Ni-Cu liquid alloy. The first to solidify is nickel for its higher melting point. Entering liquidus line, the solubility of nickel is changing as temperature decreases. This shifts the equilibrium in the non-solidified solution and causes the concentration of each solidified area to be different than the previous one. The phenomena thus is called nonequilibrium solidification (Callister W. D., 2001).

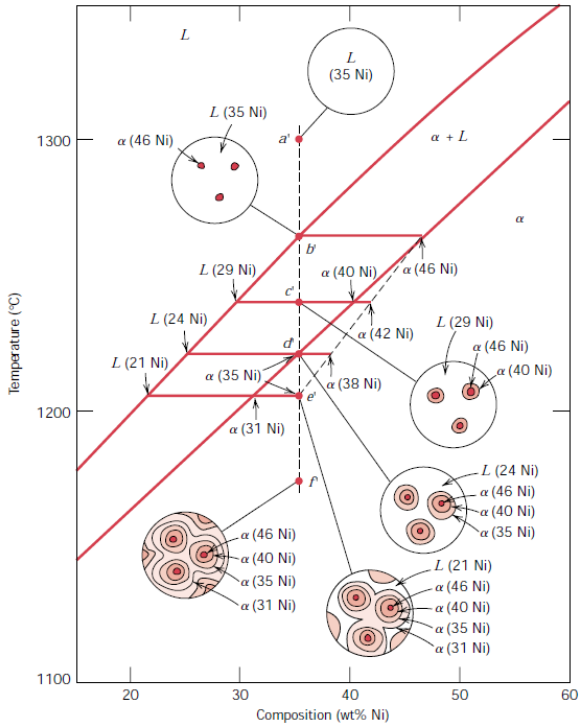

Figure 48 Segregation in the liquid system of Ni 35 wt-%-Cu 65 wt-%.

The case in figure 48 is classified as segregation by different melting point of the composing elements. Another factor that leads to segregation beside melting point is physical movement of solid or liquid phase during solidification, or in other words, diffusion (Flemings, M. C., 2006). The mechanism of diffusion, however, are quite numerous:

- gravity driven, where the solid/liquid flow is caused by difference in density;
- volume driven, where solidification shrinkage causes density of the solution to change;
- convection driven, where convection cause a flow in the bulk liquid;
- electromagnetic force driven;
- solid movement, where the movement of solidified phase causes flow within the system, as in cases of bulging in continuous casting.